2

INIS-mf--10920

LIFETIME MEASUREMENTS OF CHARMED MESONS WITH HIGH RESOLUTION SILICON DETECTORS

Gijs de Rijk

STELLINGEN

1. De konklusie van Atkinson et al. omtrent de bruikbaarheid van scintillerende fiber detektoren voor de spoordetektie van hoog-energetische botsingsprodukten in opslagringen geldt niet wanneer het plastic fibers betreft.
   M. Atkinson et al., CERN-EP/86-110.
   J.M. Gaillard, Proc. DPF conference, Eugene Oregon 12-15 Aug 1985.

2. De aanduiding van de ladingstoestanden van deeltjes in 'Review of Particle Properties' is inconsistent.
   Review of Particle Properties, Particle Data Group, Phys. Lett. 170B (1986).

3. De in de V.S. gebruikelijke notatie voor de reeksontwikkeling van het magnetische veld verdient de voorkeur uit wiskundig oogpunt. De Europese notatie verdient de voorkeur uit fysisch oogpunt, daar zij de poligheid van het veld benadrukt.
   M. Tigner, Proc. ICFA workshop on Superconducting magnets and Cryogenics, BNL May 1986.
   J. Coupland, Nucl. Instr. and Meth. 78(1970)181.
   C. Daum et al., DESY-HERA 83/01.

4. Het feit dat de sexe van aardappelcysteaaltjes (Globodera pallida en G. rostochiensis) niet erfelijk bepaald is, maar een larve zich alleen bij voldoende voedselaanbod tot een vrouwtje ontwikkelt, zou de teelt van voor aardappelmoeheid vatbare rassen op zeer zwaar besmette percelen billijken.
   D. Mugniery et al., Revue Nématologie 4(1981)41.
   Beschikking aardappelmoeheid 1973.

5. De berekening van de verhouding van het reële to het imaginaire gedeelte van de $\bar{p}p$ verstrooiings amplitude door Poth uit gegevens omtrent antiprotonische atomen is aan bedenkingen onderhevig.
   H. Poth, CERN-EP 85/135.

6. De polarisatie van een $\bar{p}$ bundel met een impuls van 600 MeV door een gepolariseerd proton doelwit wordt beter beschreven door het Parijs model dan door het Dover-Richard model.
   R. Kunne, Contr. to $\bar{p}$ Conf., Tessaloniki Sept. 1986.
   C. Dover et al., Phys. Rev. D17(1978)1770.
   J. Côté et al., Phys. Rev. Lett. 48(1982)1319.

7. De toepassing van CCD spoordetectoren in combinatie met een vertexteleskoop van Silicium mikrostrip detektoren levert een belangrijke verbetering op van de plaatsbepaling van de gedetekteerde sporen. Deze toepassing schept de mogelijkheid om, vrijwel zonder achtergrond, baryonen met charm te bestuderen, die een levensduur hebben van ongeveer $1 \cdot 10^{-13}$ s.
   S. Barlag et al., Contr. XXII Conf. on High Energy Physics, Berkeley USA, July 1986.

8. CERN zou voor het benutten van de technische expertise in de lidstaten vaker buiten de grenzen van Frankrijk en Zwitserland moeten kijken. CERN zou er derhalve goed aan doen haar dienstfietsen uit Nederland te betrekken.

9. De meting van de totale werkzame doorsnede van de $\bar{p}p$ reactie bij een zwaartepuntsenergie van 900 GeV door Almer et al. berust op te veel veronderstellingen om wezelijk tot onze kennis te kunnen bijdragen.
   G. Almer et al. Zeit. f. Phys. C 32(1986)153.

10. De gemiddelde lengte van de nederlandse man als functie van zijn geboortejaar lijkt exponentieel toe te nemen.
    Statistisch Zakboekje 1983.

11. Om de fout op de in dit proefschrift gemeten verhouding $P^{(8)}/P^{(1)}$ tot ongeveer 25% terug te brengen dienen de meetfouten op $\tau(D^+)/\tau(D^0)$ en $\tau(D^+)/\tau(D_s^+)$ met respektievelijk een faktor 2 en 4 teruggebracht te worden.
    Dit proefschrift hoofdstuk 8.

12. Koffieautomaten die tevens soep serveren zouden op estetische gronden verboden moeten worden.

G. de Rijk,
Genève, oktober 1986.

LIFETIME MEASUREMENTS OF CHARMED MESONS WITH HIGH RESOLUTION SILICON DETECTORS

Gijs de Rijk

LIFETIME MEASUREMENTS OF CHARMED MESONS WITH HIGH RESOLUTION SILICON DETECTORS

ACADEMISCH PROEFSCHRIFT

ter verkrijging van de graad van doctor in
de Wiskunde en Natuurwetenschappen aan
de Universiteit van Amsterdam, op gezag
van de rector magnificus Dr. D.W.Bresters,
hoogleraar in de faculteit der wiskunde en
Natuurwetenschappen, in het openbaar te
verdedigen in de Aula der Universiteit
(tijdelijk in de Oude Lutherse kerk, ingang
Singel 411, hoek Spui) op donderdag
20 november 1986 des namiddags
te 14.00 uur

door

Gijsbertus Adrianus Franciscus de Rijk

geboren te Breda

Promotor : Prof. Dr. J.C. Kluyver
Co-promotor : Dr. C. Daum

The work described in this thesis is part of the research program of the "Nationaal Instituut voor Kern en Hoge Energie Fysica (NIKHEF)". The author was financialy supported by the "Stichting voor Fundamenteel Onderzoek der Materie (FOM)".

CONTENTS

1. INTRODUCTION

This thesis describes an experiment in which the lifetimes of pseudoscalar charmed mesons (D^o, D^+, D_s^+)† are measured. These particles can only disintegrate via weak decay channels as described by the electro-weak interaction. The decay probabilities are modified by the strong interaction which has an important influence on the detailed structure of the decay mechanisms. Lifetimes of the charmed mesons offer an opportunity to study the strength of these effects.

The experiment is performed by the Amsterdam, CERN, Cracow, Munich, Bristol, Rutherford collaboration (ACCMOR). The collaboration started its program of charm physics in 1979 with an experiment on characteristics of charmed meson production in π^-Be interactions, using a single electron trigger. In 1982, with the availability of the first operational Si microstrip detectors, the program was extended with the study of charmed particle lifetimes, using high resolution Si microstrip detectors for the measurement of the incident beam particles and the interaction products. It was shown that a sample of charmed particles on a low background could be collected for lifetime studies. The use of the Si microstrip detectors was extended in 1984 by replacing the Be target with a Si active target. Also, the single electron trigger was exchanged for an interaction trigger. The active target consists of a closely packed array of 14 Si microstrip detectors. Interactions of the incoming beam particles with the target material are registered by the detectors, and the charge signals caused by the interaction secondaries are registered by the detectors downstream of the interaction vertex, offering the possibility to detect jumps in the charge particle multiplicity due to e.g. the decay of short lived particles.

The analysis described in this thesis is a preliminary analysis of part of the data taken in 1984.

The thesis is organized as follows. In chapter 2 a description is given of the spectrometer used for the measurements. In chapter 3 the most important features of Si microstrip detectors are discussed, together with some details of their implementation in the spectrometer. Chapter 4 contains a description of the trigger, the calibration procedures, and the data sample collected. Chapter 5 treats the track reconstruction and event selection for this analysis. A presentation of the selected events and the calculation of

† The new particle nomenclature as proposed by the particle data group, and used in the Review of Particle Properties 1986, will be used throughout this thesis. The D_s^+

lifetimes is given in chapter 6. The other existing experimental data on the lifetimes of charmed particles are reviewed in chapter 7. The final chapter 8 summarizes the relevant theoretical aspects of the decay of charmed particles. It is shown how the lifetime data determine various parameters of the effects of strong interactions on decay probabilities.

2. THE EXPERIMENTAL APPARATUS

2.1 Introduction

In this chapter a description will be given of the experimental apparatus used for this thesis. The ACCMOR spectrometer was originally designed for the detection of hadronic decays of charmed particles with the help of a single electron trigger (NA11). In that experiment the selection criterion for a charmed particle was the detection of a single electron coming from the associated or pair produced charmed particle. In NA32 the selection criterion is the observation of a secondary decay vertex at a small distance from the primary production vertex. High precision silicon detectors were added to provide coordinate information for this purpose. The experiment is located in beam line H6 of the North Area at the CERN SPS (see fig. 2.1). The data described in this thesis were obtained with an unseparated negatively charged hadron beam with a momentum of 200 GeV.

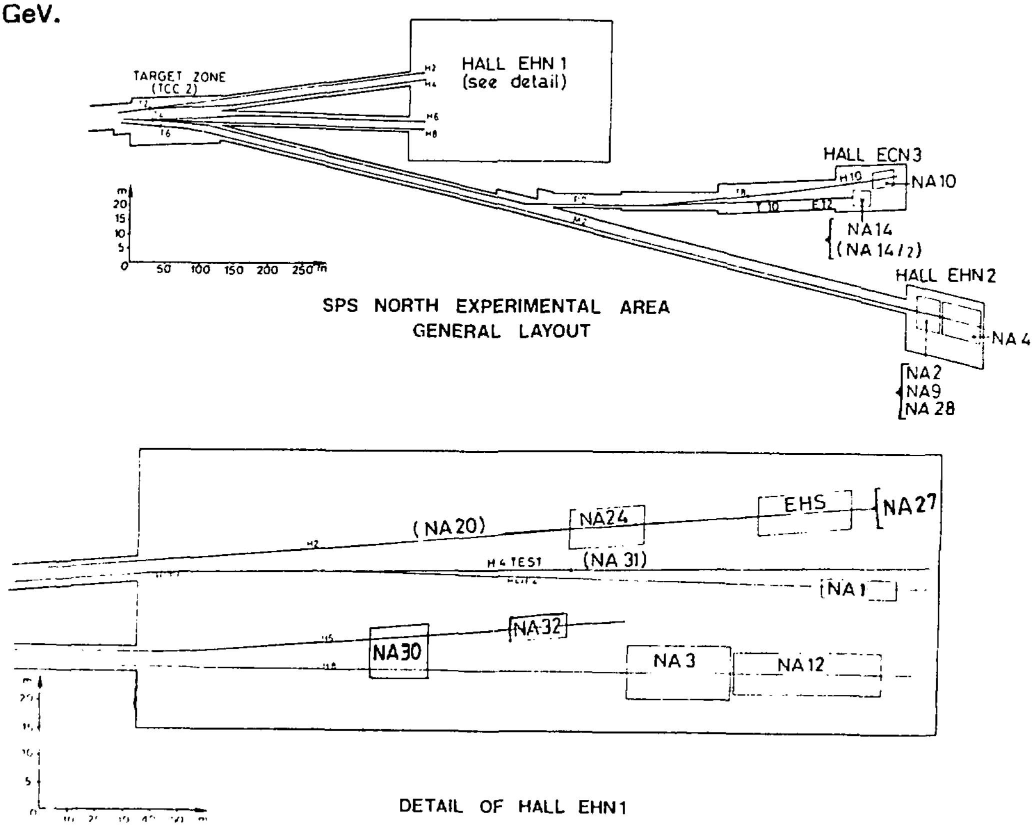

Fig. 2.1 The layout of the beam lines in the CERN north area.

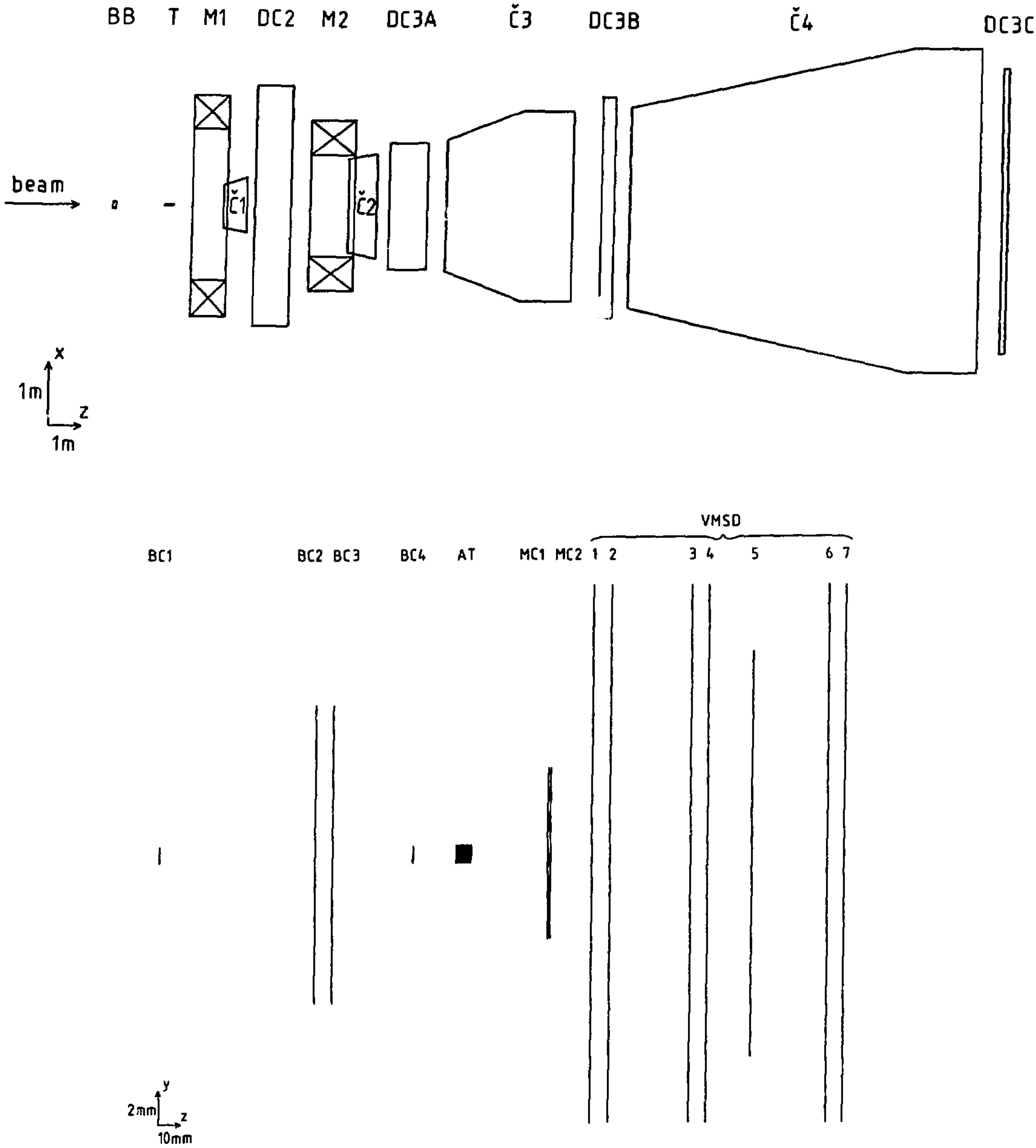

Fig. 2.2 The spectrometer:

a) general overview:

BB beam hodocope, T target area, M1,M2 magnets, DC drift chambers, C1–C4 Cerenkov counters;

b) target area:

BC1,BC4 beam silicon detectors active target type, BC2,BC3 beam silicon detectors VMSD type, AT active target (14 planes), MC multiplicity counters (2 planes), VMSD1-VMSD7 vertex microstrip

Figure 2.2 shows the spectrometer. It can be divided into two parts.

1. The original NA11 spectrometer, consisting of two large aperture magnets for momentum analysis, 48 planes of drift chambers for track reconstruction and four threshold Cerenkov counter hodoscopes for particle identification (see fig. 2.2a).

2. The target area in which the new silicon detectors are located (fig. 2.2b). It consists of the following elements.

- A scintillator and silicon detector beam telescope for a precise measurement of the incoming beam track.
- An active target made of silicon detectors, in which the interaction takes place. It is used for the measurement of the primary vertex and the detection of the charged secondaries from the interaction. Changes in the charged multiplicity, due to decaying particles or secondary interactions, can be detected at a finite distance from the primary interaction point.
- A silicon vertex telescope (VMSD = Vertex Micro Strip Detector) for precision tracking of the interaction products.

The coordinate system used throughout this thesis is as follows: the Z direction is along the beam line, the X and Y directions are horizontal perpendicular to the beam and vertical, respectively (see also fig. 2.2). In the next sections the spectrometer elements will be briefly described. Details on the traditional components of the detectors and the general performance of the spectrometer may be found in refs SPIE1 and BELA1. The new elements, made of silicon detectors, will be treated in more detail.

2.2 The Beam Line

Protons of 450 GeV momentum are extracted from the SPS accelerator and steered onto the primary target T4 (fig. 2.1). From here secondary beams of interaction products, at various momenta, can be selected and guided via the secondary beam lines towards the experiments. The beam arrives in bursts with a repetition time of 14 s and a burst length of 2.5 s. The beam line used in this experiment is the H6 beam line, providing a negatively charged unseparated hadron beam of 200 GeV momentum. This beam is focussed onto the active target. The FWHM[†] of the focus in X and Y are 8 mm and 0.3 mm, respectively (see fig. 2.3). The beam focus in Y has a stability of better than 40 μm. The maximum intensity is $3.5 \cdot 10^6$ particles/burst. As the beam is unseparated (see table 1 for the beam

† FWHM = Full Width Half Maximum.

composition), an identification is made of each incoming beam particle with 2 differential Cerenkov counters (CEDAR) in the beam line. The signals of the CEDARs can be used in the trigger of the experiment to select a given type of particle in the beam. In order to allow a high beam intensity compatible with a reliable operation of the drift chambers, the beam can be diverted with the help of a kicker magnet during the dead time of the data transfer to the online computer.

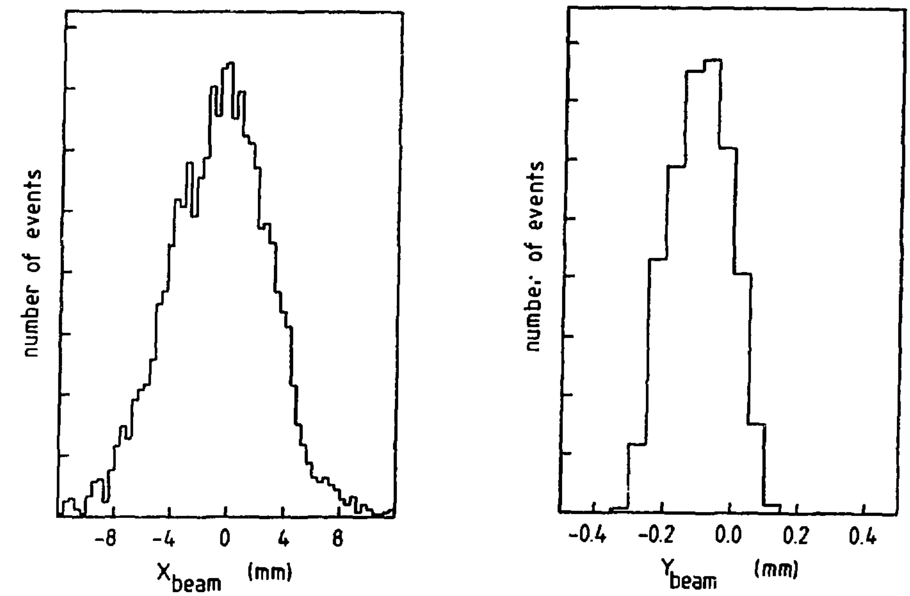

Fig.2.3 Profile of the beam in X and Y directions at the focus.

Table 1: The beam composition
as measured with the CEDAR differential Cerenkov counters

fraction π^-	0.880
fraction K^-	0.036
unidentified	0.084

2.3 The Beam Telescope

The beam telescope is used to :

1. register the passage of a beam particle through a defined volume,

The former function is performed by the fast trigger i.e. the online selection of the passage of a "good" beam particle (the trigger will be described in chapter 4). The latter function is performed by the measurement of coordinates on the trajectory and offline reconstruction of this trajectory from these coordinates. This is done for trigger selected events only (see chapter 5 for a description of the offline reconstruction). The beam telescope (fig. 2.4) consists of :

- 2 sets of 2 scintillator hodocopes,
- 4 trigger scintillator counters,
- 2 VMSD type silicon microstrip detectors,
- 2 active target type silicon microstrip detectors.

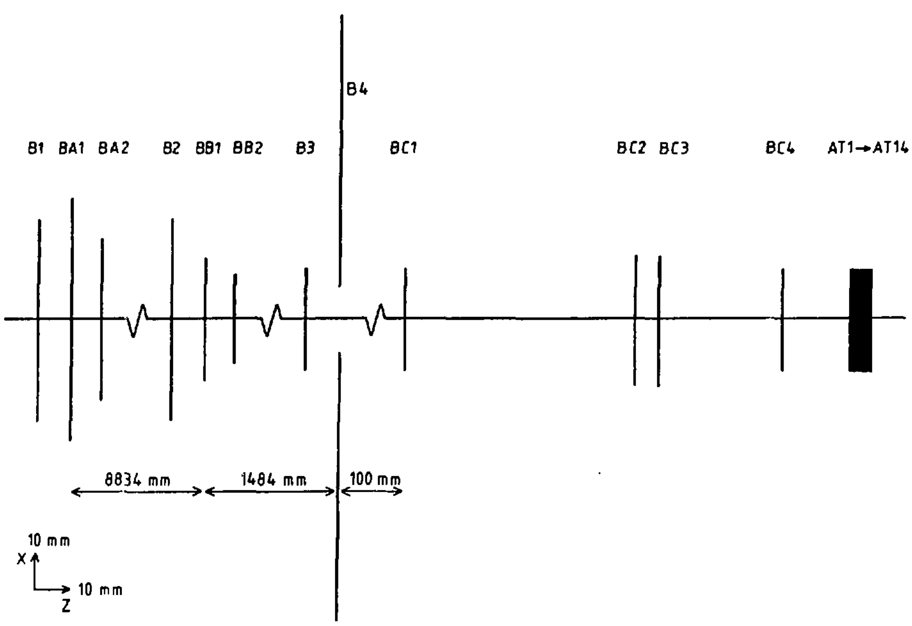

Fig. 2.4 The beam telescope:
B1-B4 beam scintillator counters,
BA1-BA2,BB1-BB2 beam hodoscopes, BC1,BC4 active target type Si detectors, BC2, BC3 VMSD type Si detectors, AT active target (14 planes).

All detectors except the VMSD's can be used in the fast trigger, whereas the scintillator counters are omitted in the offline reconstruction. The main properties of the beam telescope detectors are summarized in table 2.

Table 2: The elements of the beam telescope.

<u>scintillator hodoscopes</u>				
	BA1	BA2	BB1	BB2
strip orientation (°)*	0.	90.	0	90.
active area (XxY)(mm^2)	72.x48.	48.x72.	36.x25.	25.x36.
# strips	12	12	12	12
strip width (mm)	6.	6.	3.	3.
strip distance (mm)	2.	2.	1.	1.
resolution (mm)	2./√12	2./√12	1./√12	1./√12
<u>scintillator counters</u>				
	B1	B2	B3	B4
active area (XxY)(mm^2)	60.x60.	60.x60.	30.x10.	200.x200.
hole size (XxY)(mm^2)				20.x2.

<u>silicon microstrip detectors</u>		
	VMSD type	active target type
# planes	2	2
orientation (°)*	± 14.	0.
active area (XxY)(mm^2)	36.x9.4	30.x0.96
# strips/plane	120	48
strip pitch (μm)	20.	20.
readout pitch(μm)	60.	20.
resolution(μm)	4.5	2.8

* Angle with the horizontal.

2.4 The Active Target

The active target (fig. 2.5) is an array of 14 identical silicon microstrip detectors closely packed together, followed at a distance of 40 mm by 2 large silicon microstrip detectors, the multiplicity counters. The functions of the active target are the following :

- The first plane is used to register the beam and to veto upstream interactions. The hit information is employed in the fast trigger for the selection of a useful passage of a beam particle and to veto upstream interactions. The pulse height information from this detector is used in the offline beam reconstruction.
- The 2^{nd} to 7^{th} plane serve as target. A trigger on pulse height information selects interactions in these planes (see section 4.1). The extrapolated beam position and the knowledge of the plane in which the interaction takes place thus define the interaction point. The six planes provide an interaction rate which is sufficient to saturate the readout system.
- The planes behind the interaction plane and the multiplicity counters record the energy deposition by the charged secondaries of the interaction. The pulse height information of these detectors is used to detect changes in the charged particle multiplicity, which may be due to e.g. decaying particles or interactions of secondaries with the detector material.

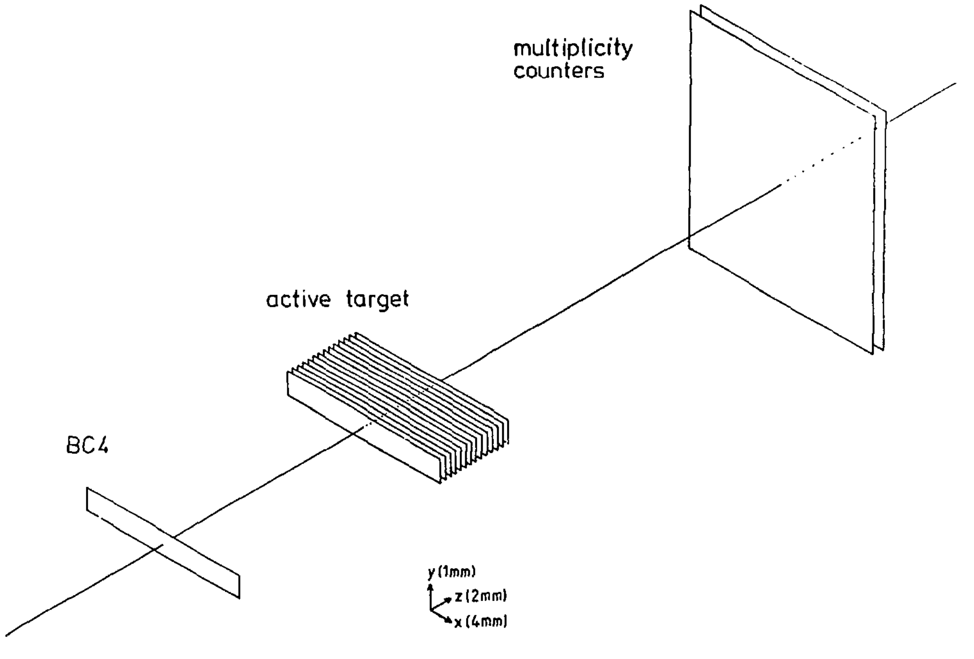

Fig. 2.5 Active target.
Isometric view of the active target with the last beam detector (BC4) and the multiplicity counters.

The main characteristics of the target may be found in table 3. A more detailed description of the principle of operation and the performance will be given in chapter 3.

Table 3: The active target

	target	multiplicity counters
# planes	14	2
active area (XxY)(mm^2)	30.x0.96	36.x9.6
thickness detector (μm)	280.	280.
dist. between det. centres (μm)	500.	1000.
# strips/det.	48	24
strip pitch (μm)	20.	400.
resolution (μm)	2.8	400./√12
strip orientation (with horizontal)(°)	0.	0.

2.5 The Vertex Microstrip Detectors.

The measurement of high precision coordinates of the secondary tracks for vertex reconstruction is performed by the vertex microstrip detectors (fig. 2.2b). The strip pitch of these detectors is 20 μm. Only every 3^{rd} strip is read out in the inner area, and every 6^{th} strip in the outer area. The signals on the non-readout strips are measured with the readout strips by capacitive coupling (capacitive charge division). This readout technique reduces the number of electronic channels with a factor 5. The spatial resolution of the detectors for a well separated track (in the 60 μm readout region) is 4.5 μm. The resolution degrades sharply when the distance between 2 tracks becomes less than 120 μm (see also section 3.5). The main characteristics of the detectors are displayed in table 4. In chapter 3 the general principle of operation of microstrip detectors will be described. More details on the detector construction and operation may be found in refs. BELA1 and BAIL1.

Table 4: The vertex microstrip detectors

strip orientation (°)*	+14.	-14.	0.
# planes	3	3	1
active area (XxY)(mm^2)	36.x24.	36.x24.	36.x24.
# strips/plane	1200	1200	1200
strip pitch (µm)	20.	20.	20.
# readout strips/plane	240	240	240
readout strip pitch			
inner(outer) region (µm)	60.(120.)	60.(120.)	60.(120.)
area inner region(XxY)(mm^2)	36.x7.2	36.x7.2	36.x7.2
resolution inner(outer) region (µm)	4.5(7.8)	4.5(7.8)	4.5(7.8)

* Angle with the horizontal.

2.6 The Downstream Spectrometer.

The momentum analysis and particle identification of charged interaction products are performed by the downstream spectrometer (fig. 2.2). To combine a good acceptance for low momentum particles with a high momentum resolution for high momentum particles a two magnet setup is used. Charged particles produced in the target are deflected by a low field wide gap magnet which deflects the particles in the X-Z plane. Their tracks are measured by the drift chambers between the two magnets (ARM2). High momentum (≥ 3. GeV) forward tracks are further analyzed by a high field smaller gap magnet (BBC). These are measured by the 3 packs of drift chambers behind the BBC magnet (ARM3). In table 5 the momentum resolution for the different track topologies is listed. Particle identification is provided by four threshold Cerenkov counter hodoscopes. Hodoscope C1 is positioned in the MNP magnet, hodoscope C2 in the BBC magnet, and C3 and C4 are located downstream of the BBC magnet. Table 6 contains the most important parameters of the spectrometer. Figure 2.6 schematically depicts the momentum windows for particle identification.

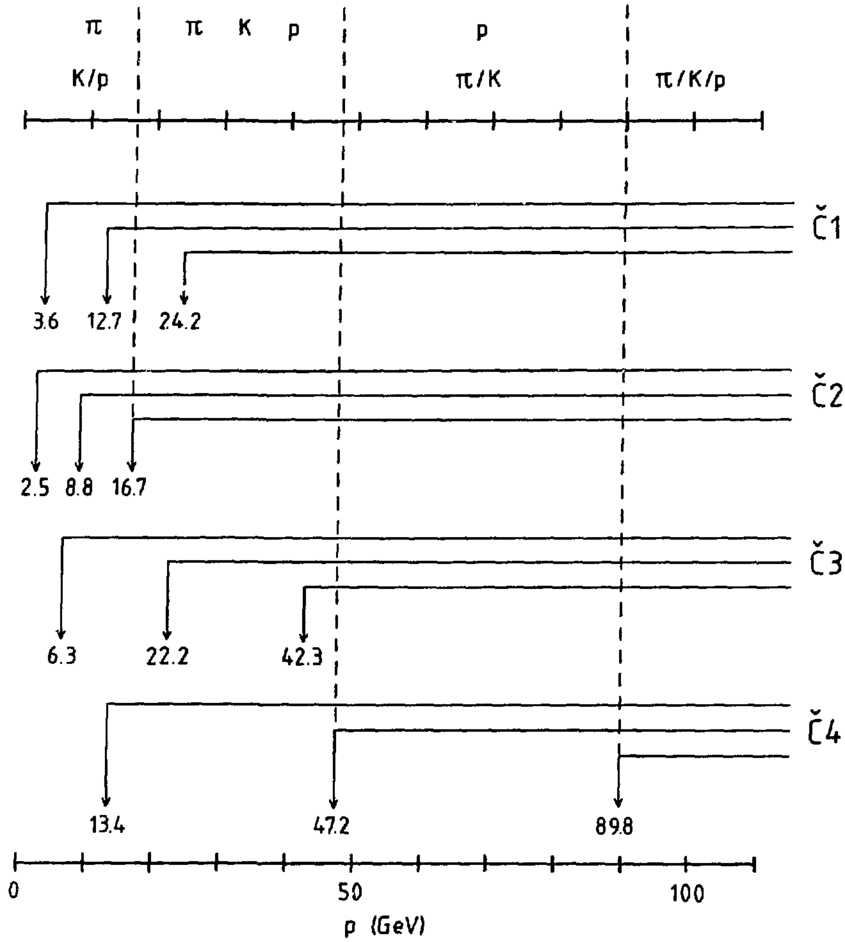

Fig. 2.6 Windows for particle identification.
For each Cerenkov counter hodoscope the 3 momentum threshold values are indicated, from left to right pion, kaon and proton (the numbers under the arrows). The top part of the picture displays the momentum intervals in which particles can be identified, when they traverse the complete spectrometer. Particles which can be separated uniquely are indicated on the top line, confused particles on the second.

Table 5: Momentum resolutions

reconstructed in			Δp/p	fraction of
VMSD	ARM2	ARM3	in %	all tracks
no	yes	no	0.15	0.136
no	no	yes	0.13	0.037
yes	yes	no	0.15	0.332
yes	no	yes	0.11	0.039
no	yes	yes	0.10	0.062
yes	yes	yes	0.09	0.394

Table 6: The spectrometer

The spectrometer magnets

	MNP	BBC
magnetic length (m)	1.3	1.7
window (X×Y)(m^2)	2.4x0.6	1.6x0.5
field integral $\int B_Y dZ$ (Tm)	0.90	2.06

The drift chambers

	ARM2	ARM3A	ARM3B	ARM3C
# planes	20	16	8	2
active area (X×Y)(m^2)	3.8x1.4	2.0x0.8	3.5x0.85	4.5x2.
wire orient. (°)*	0., ± 14.	0., ± 30.	0., ± 27.	0., ± 13.5
# sense wires/plane	96	48	94, 72	112
max drift length (mm)	20.	20.	20.	20.
mean drift velocity (µm/ns)	52.	52.	52.	52.
resolution (mm)	0.17	0.17	0.17	0.17

* Angles with the vertical

Cerenkov counter hodoscopes

		C1	C2	C3	C4
# mirrors		4x14	2x9	2x11	2x10
threshold	π	3.6	2.5	6.3	13.4
(GeV)	K	12.7	8.8	22.2	47.2
	p	24.2	16.7	42.3	89.8
# photoelectrons for a β=1. particle		10.	15.	12.	9.5

3. SILICON MICROSTRIP DETECTORS

3.1 Basic Operation

All Si microstrip detectors employed in this experiment have the same basic operation, but can feature different readout techniques (section 3.5). Figure 3.1 shows schematically a Si microstrip detector. The detector consists of a chip of n doped high resistivity Si with electrodes on both sides. One electrode has a strip structure and consists of p implanted regions covered with aluminium. These p implanted regions form the strip shaped diodes which determine the operation of the detector. The other electrode, the so-called "back" side, consists of an n^+ implanted layer, covered with aluminium. A voltage is applied between the strip electrodes and the back side in the so-called reverse bias direction. (The back side is then on positive voltage.) This voltage depletes the counter of its free charge carriers, leaving behind the ionized dopand atoms which produce an electric field decreasing linearly with the distance to the strips. The maximum depletion is reached at a voltage of 120 V, the operating voltage of these counters. When a charged relativistic particle traverses a detector it will ionize atoms along its path. Subsequently, the electrons from this primary ionization will ionize other atoms. This cascade process continues until no electron has enough energy left to produce any further ionization. This means that the ionization process stops when the electrons are all left in the conduction band, each leaving behind a hole in the valence band. The average energy required to produce an electron-hole pair in Si is 3.6 eV. In 280 µm thick Si detectors the average number of electron-hole pairs so created is 24000. They are initially located in a narrow tube around the particle trajectory. Under the influence of the electrical field the electrons will drift towards the "back" side and the holes to the "front" side where they will be collected at the strips. The following paragraphs deal with

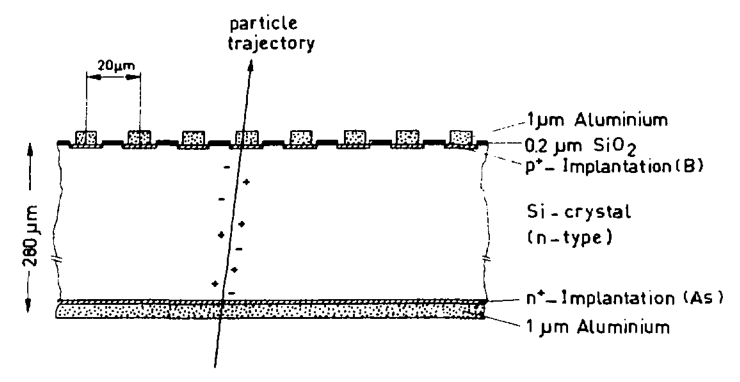

Fig. 3.1 Cross section of a Si microstrip detector.

a more detailed description of several important subprocesses in Si detectors. Further descriptions may be found in references CHAR1, HEIJ1 and RANC1.

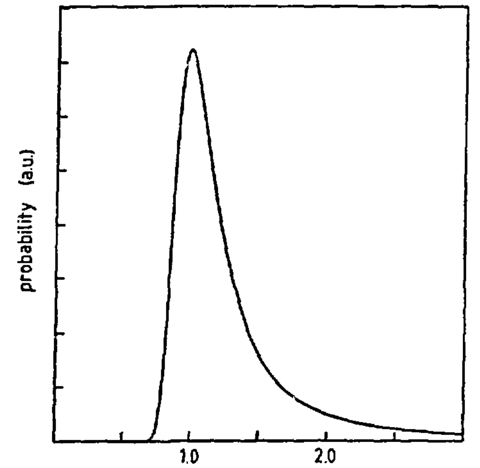

Fig. 3.2 A Landau energy loss distribution.

3.2 Ionization in Si

The energy loss distribution of relativistic charged particles in matter was first successfully described by Landau (LAND1). Vavilov refined this description (VAVI1), but for 280 µm Si both are practically identical and we will use the former. The Landau distribution (see refs. ROSS1 and KOLB1 and fig. 3.2) is based on Rutherford scattering on free electrons. A later addition (BLUN1, SHUL1) takes into account that the electrons in matter are not free but bound. This results in a distribution which can be expressed as a convolution of a Landau and Gaussian distribution. Thus (HANC1, HANC2) :

$$f(\Delta,x) = (1./\sigma\sqrt{(2\pi)}) \int_{-\infty}^{\infty} f_l(\Delta',x)\exp[-(\Delta-\Delta')^2/2\sigma^2]d\Delta' \qquad (3.1),$$

with :

$f_l(\Delta',x)$	the Landau distribution,
Δ	the actual energy loss,
x	the traversed distance in the Si,
ρ	the density of the Si.

The width of the Gaussian distribution is given by :

$$\sigma^2 = (8/3)\ \xi\Sigma_i l_i(Z_i/Z)\ln[2m_e c^2\beta^2/l_i] \qquad (3.2),$$

in which :

$$\xi = 153.4\ (z^2/\beta^2)\ (Z/A)x\rho \qquad \text{(keV)} \qquad (3.3),$$

with :

I_i	the ionization potential of the i-th shell in Si,
Z_i	the number of electrons in the i-th shell in Si,
z	the charge of the incident particle,
Z,A	the charge and atomic weight of Si.

The most probable energy loss is expressed by the Bethe-Bloch formula (FANO1) :

$$\Delta' = x \ (FZ\rho z^2/A\beta^2)\,(\ln[2m_e\gamma^2\beta^2c^2/I]-\beta^2) \qquad (3.4),$$

with :

m_e	the electron mass,
I	the binding energy of electrons in Si,
F	$= 0.307$ MeV cm^2/g.

Not taken into account are very energetic δ-rays which can escape out of the thin detectors, thus reducing the tail of the distribution. A measured distribution will also include noise which is due to two sources : the intrinsic detector noise, and the electronics noise. When expressing a measured distribution in terms of the above formalism, the width of the contributing Gaussian will be :

$$\sigma_{Gauss} = \sqrt{[\sigma^2 + \sigma^2_{int.\ noise} + \sigma^2_{elec.\ noise}]} \qquad (3.5).$$

3.3 Charge Drift and Diffusion

Under the influence of the electric field in the counter the generated charges will separate and drift to the electrodes of the detector. The strength of the electric field at the voltage where full depletion is reached, is sufficient to separate electrons and holes fast enough to prevent recombinations (SZE1) and thus signal losses. The electrons will drift towards the back side of the detector. The holes will drift towards the strip electrodes, and will be collected there. The positive charges collected by the strips produce the signal to be read out. To derive an expression describing the shape of the charge distribution which will be collected by the strips, one has to solve first the Poisson equation for the electric field $\vec{E}$ in which the charges move (BELA1)(fig. 3.3) :

$$\nabla\vec{E} = (4\pi/\varepsilon)\,\rho \qquad (3.6),$$

Together with the relation for the depletion voltage this gives :

$$U_D = -\,(\rho d/2\varepsilon) \qquad (3.7),$$

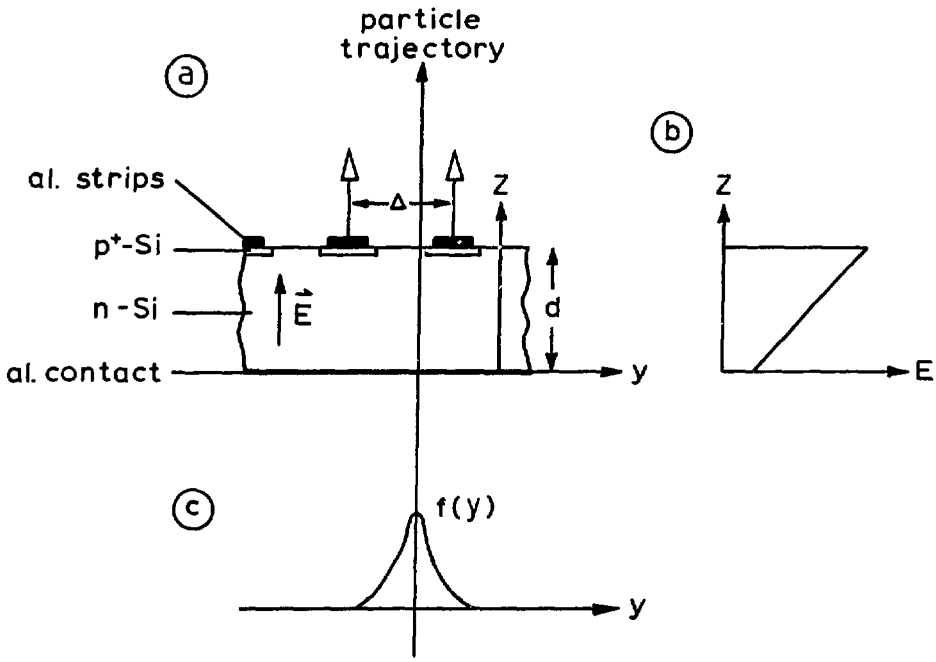

Fig. 3.3 Definition of symbols in the drift calculation.
a) Schematic representation of a Si microstrip detector,
b) electric field $\vec{E}$ in a detector,
c) charge distribution (expression 3.13).

with

d	the thickness of the counter,
ρ	the charge density of dopand ions,
U_D	the voltage at which full depletion is reached,
ε	the dielectric constant.

This gives for the electric field as function of the depth z in the detector :

$$E(z) = ((U-U_D)/d) + (2U_D z/d^2) \qquad \vec{E} = (0,0,E) \qquad (3.8),$$

with

U_D	the voltage at which full depletion is reached,
U	the applied voltage,
d	the detector thickness.

The drift velocity is then given by :

$$v = (dz/dt) = \mu E(z) \qquad (3.9),$$

with :

μ the mobility of the holes.

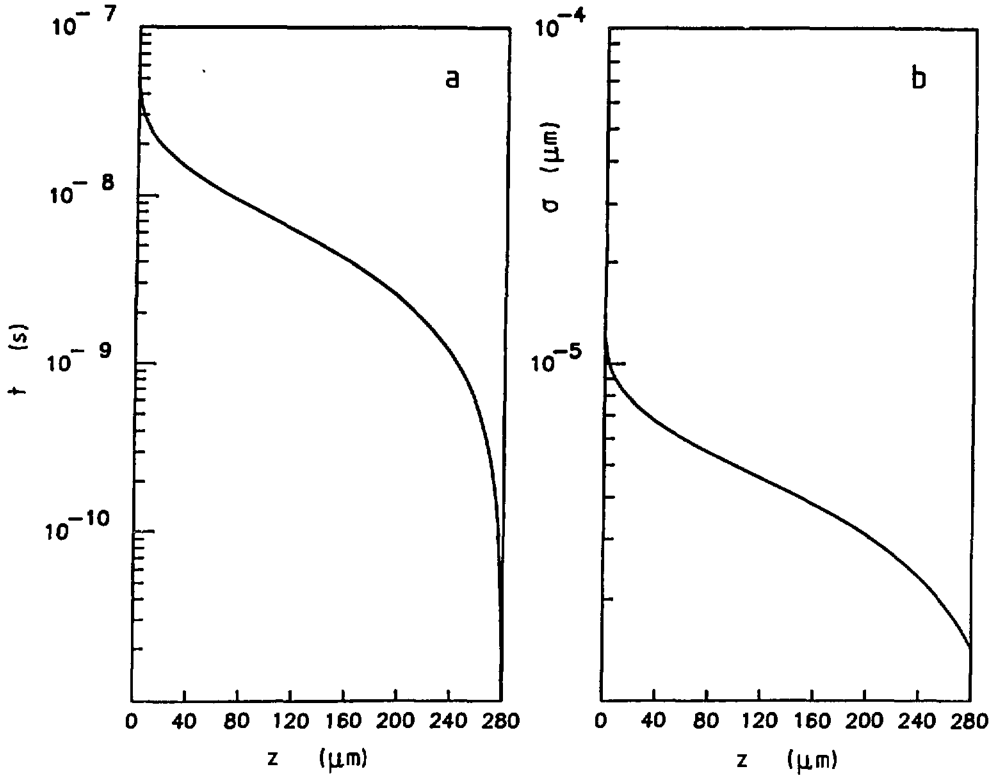

Fig. 3.4 a) Drift time of holes as function of the drift distance in a Si microstrip detector with $U = U_d = -120$ V (expression 3.10);

b) Width of the charge cloud after drift to the strips as function of the drift distance (expression 3.12).

Integration of (3.9) will then provide us with the relation between the drift time and the drift distance (fig. 3.4a) :

$$t(z) = (-d^2/2\mu U_D)\ \ln[1 - (2U_D(d-z)/(U-U_D)d)] \qquad (3.10),$$

During this drift process, the charge cloud will disperse due to diffusion. In the absence of an electric field and recombination of electrons and holes, the charge distribution as a result of diffusion will be :

$$c(x,y,t) = (1/4\pi D_h t)\ \exp[-\ (x^2+y^2)/4D_h t] \quad , \quad 0 \le z < d \qquad (3.11),$$

with : D_h the transverse diffusion constant of holes in Si.

Integration over x gives the charge distribution in the projection perpendicular to the strips :

$$C(y,t) = \int_{-\infty}^{\infty} c(x,y,t)dx = (1/\sqrt{(4\pi D_h t)}d) \exp[-(y^2/4d_h t)] \qquad (3.12).$$

We can now include the effect of the finite width of the initial charge distribution δ by replacing the time t by t+to with $t_o = \delta^2/2D_h$ (fig. 3.4b). The effect of the electric field is expressed by the relation between t and z (expression 3.10). Integration over z will then produce the charge distribution at the strips.

$$f(y) = (1/\sqrt{(4\pi D_h)}d) \int_0^d (dz/(\sqrt{(t+t_o)})) \exp[-(y^2/4d_h(t+t_o))] \qquad (3.13).$$

The charge distribution after drifting to the strips is thus an integral over Gaussian distributions. The width of the distributions increases with the drift distance. For a track incident at right angles the Gaussians are centered around the same position, resulting in a symmetric charge distribution. For tracks incident at other angles the Gaussians will not be centered around the same position, resulting in an asymmetric charge distribution.

3.4 Charge Deposition by Inelastic Interactions

In an interaction of high energy particles with a Si nucleus in the detector, the large ionization observed will be due to more than just the ionization of the incoming particle before the interaction and the produced particles after the interaction. In the interaction the nucleus itself may be excited and send out fragments. The nucleus may also recoil and then lose its energy via ionization. This can produce large charge depositions in the target detector. The inelastic interactions in Si can be divided into 3 categories (RANC1).

- Coherent interactions. All 28 nucleons of the Si nucleus participate in the interaction. The nucleus recoils but remains in the ground state.
- Semicoherent interactions. The nucleus recoils and is internally only disturbed to the extent that it is left in a well defined state.

  e.g. : $h + {}^{28}Si \rightarrow h^* \; {}^{28}Si^*$ (1.78 MeV)
  $\quad\quad\quad\quad\quad\quad\quad\quad \rightarrow \gamma + {}^{28}Si.$

- Incoherent interactions. The interaction takes place with one or more nucleons. The nucleus is left behind in an excited state.

In all 3 cases the end products contain a number of secondary particles and a recoiling nucleus. This recoil produces, depending on its energy, a rather large amount of ionization. In the case of excitation, the nucleus can send out ("evaporate") nucleons or groups of nucleons. At the energies involved (≪ 1 GeV) these particles are also highly ionizing. Apart from coherent interactions with a small recoil, all interactions will produce a significant amount of ionization. This fingerprint of an inelastic interaction can be used to locate an interaction in the active target. This can be used for two purposes : online to trigger on interactions and offline to reject interactions of secondaries in the planes downstream of the primary interaction vertex. Figure 3.5 shows an example of an interaction in the target.

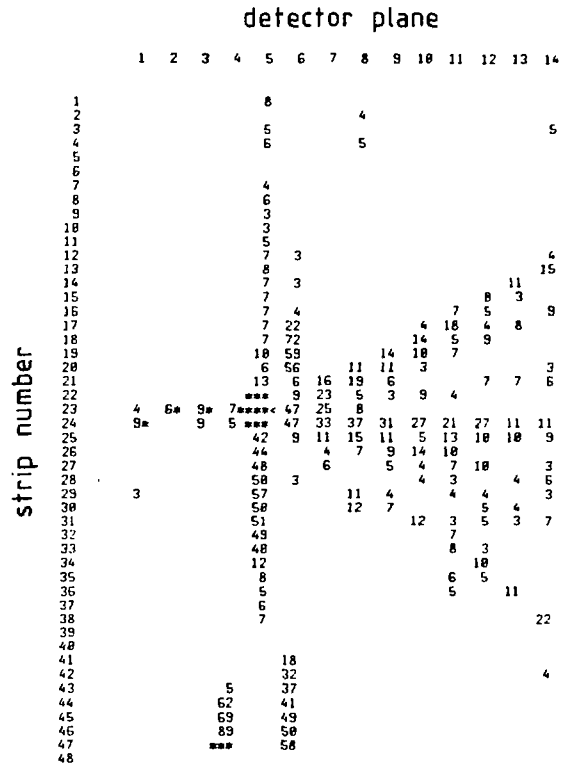

Fig. 3.5 Example of an interaction in the active target. The columns depict the detectors, the rows depict the strips. The ADC pulse heights are given in units of 0.1 minimum ionizing particles. An overflow is indicated as ***. The interaction vertex is pointed out by the symbol <. The fitted incident beam track is indicated with a *.

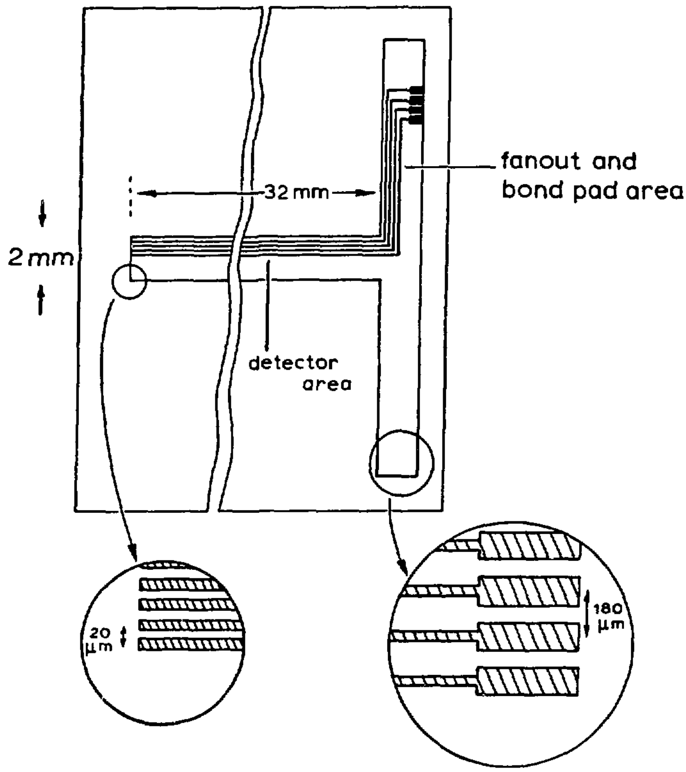

Fig. 3.6 Active target: layout of the strips and fanout on the Si chip.

3.5 Readout Types

The Si detectors used in this experiment are equipped with two different readout systems. The first type of readout is used for the active target. All strips are read out. This gives the best possible resolution but is very costly due to the large number of electronic channels used per surface area of the detector. As the active target detectors are very close to the interaction vertex, many tracks cannot be separated from each other, making a systematic use of the single coordinates impossible. The target is thus employed to sample the energy deposition by the secondaries for offline multiplicity analysis. To lead the signals from the 20 µm strips to the electronics a fanout is necessary. On the chip (fig. 3.6) a fanout pattern is provided which leads from the strips, with 20 µm pitch, to the bonding pads, with 180 µm pitch. The pads are connected to an external Kapton fanout with ultrasonically bonded wires. The connection to the preamplifiers is made with connectors soldered on the other end of the Kapton fanouts (fig. 3.7). The second type of readout is used for the VMSD's. In the central area every

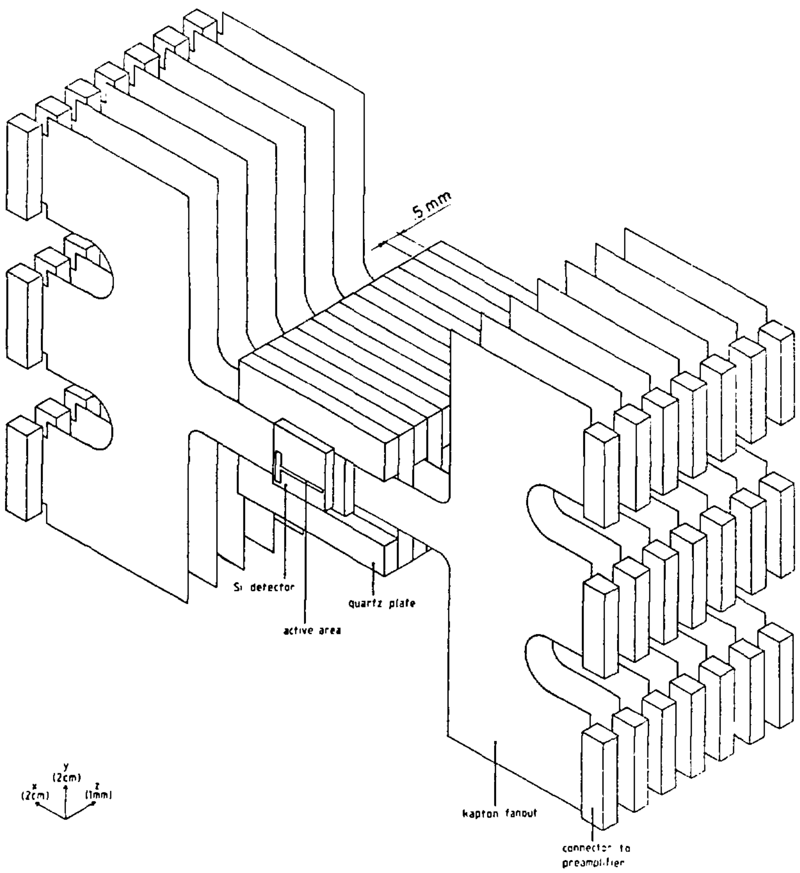

Fig. 3.7 Fully assembled active target module.
In the centre the quartz plates onto which the detectors are glued. The detectors are oriented alternatively to left and right.

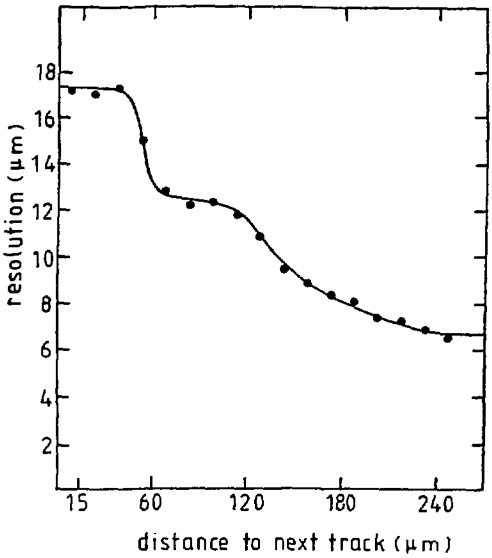

Fig. 3.8 The resolution of a track as a function of the distance to the nearest track.

3^{rd}strip is read out, in the outer area only every 6^{th} strip is read out. The signals are divided from the non-readout strips capacitively over the readout strips (capacitive charge division). This arrangement reduces the number of readout channels with a factor five. The resolution will be worse than in detectors with all strips read out due to a capacitive coupling of the strips to the grounded electrode on the other side of the detector. Figure 3.8 depicts the resolution of a track as function of the distance to the nearest track in the inner readout area. As, at most, only every 120 µm a strip is read out, a fanout on the chip is not necessary (fig. 3.9). The bonding pads on the chip are connected to a fanout made of printed circuit board via ultrasonic bonding (BELA1). The two active target type beam detectors have an active target chip but a VMSD type fanout on printed circuit board. In table 7 the measured resolutions (fig. 3.10) are compared with predictions obtained with the charge drift and diffusion model of section 3.3.

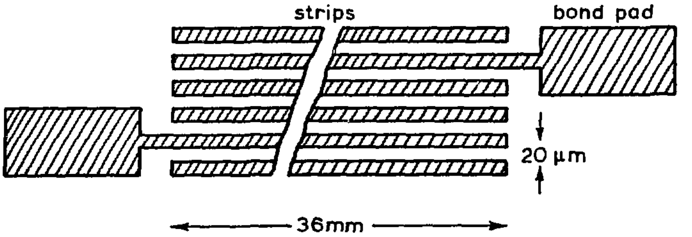

Fig. 3.9 Scheme of strips layout on a VMSD detector (60 µm readout region).

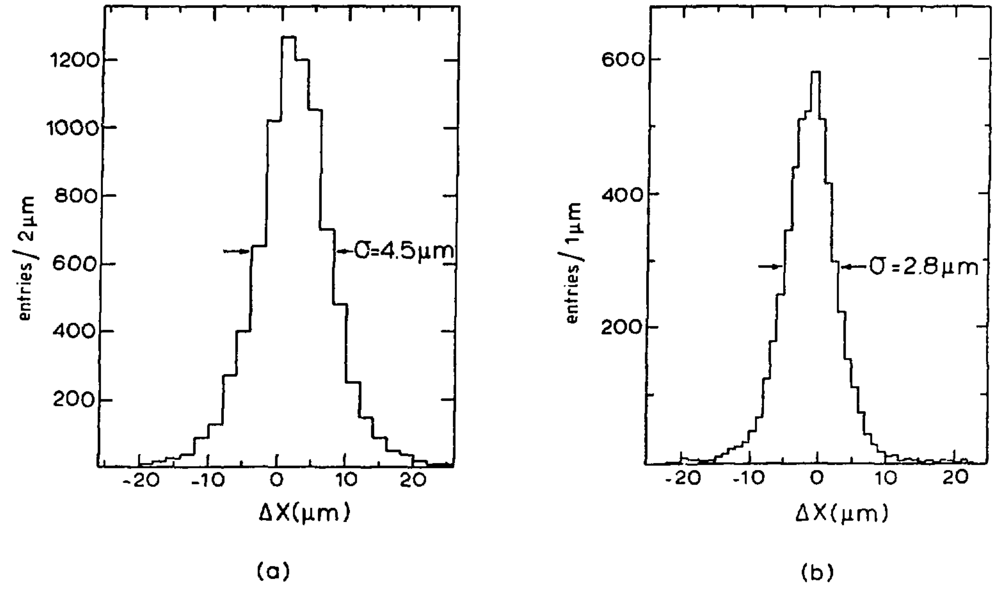

Fig. 3.10 Measured resolution of the Si detectors,
a) inner area VMSDs,
b) active target.

Table 7: Resolutions of Si microstrip detectors

comparison of the model and the measurements

	Active target	VMSD inner area	VMSD outer area
strip pitch (μm)	20.	20.	20.
readout pitch (μm)	20.	60.	120.
calculated resolution (μm)	2.8	3.6	5.9
measured resolution (μm)	2.8	4.5*	7.9*

* The measured resolution is worse than predicted, see text.

It is clear that the cost saving readout scheme of the VMSD's mainly influences the two track separation capabilities of the detectors. Later it will become clear that this is the most stringent limitation to the final vertex reconstruction.

3.6 Detector Mounting and Electronics

The microstrip detectors have resolutions of a few microns which requires a high precision in the mounting of the detectors. The position has to be fixed in all 3 directions within a few µm during data taking. Furthermore the detectors have to be parallel within a few tenths of µm and the distances between the detectors have to be known with a precision of ± 10 µm. To achieve this, the detectors are mounted on quartz precision plates and kept at fixed distances with precision gauge blocks. This assembly is placed on an optical bench and pressed together. For the different types of detectors the mounting on the quartz plates is as follows :

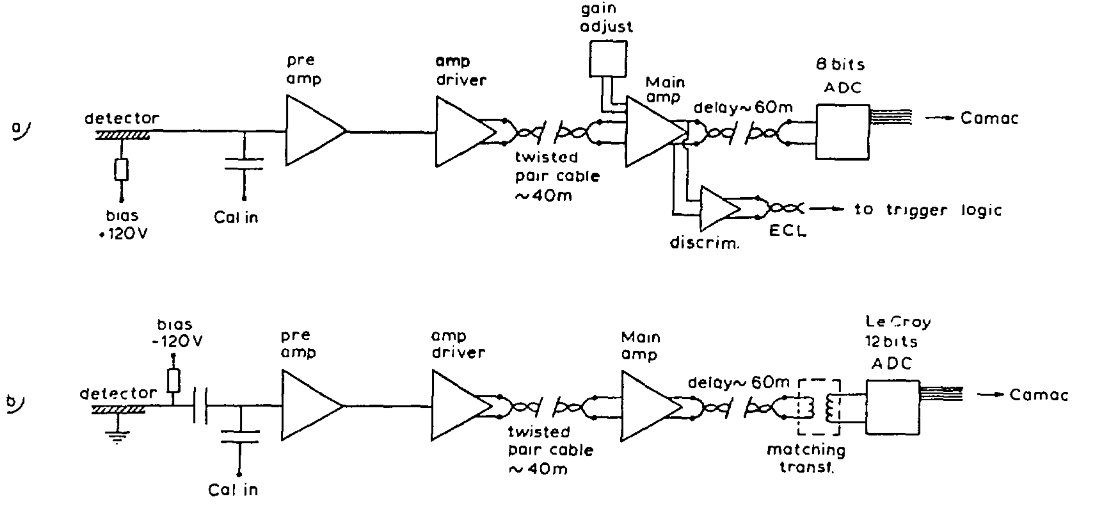

Fig. 3.11 a) Block scheme of the active target electronics,
b) block scheme of the VMSD electronics.

1. Active target type beam detectors; mounted separately on 14 mm quartz plates like the VMSD's,
2. Active target; 14 detectors each mounted on a 0.5 mm thick quartz plate and joined together in one module (fig. 3.7),
3. The two multiplicity counters; mounted on 1 mm thick quartz plates and placed togther in one module,
4. VMSD; mounted separately on 14 mm thick quartz plates (BELA1).

The electronics for the VMSD system is described in refs. BELA1 and BAIL1. The active target uses a chain of electronics similar to that of the VMSD's. The block diagrams are shown in fig. 3.11. The input charge from the detectors for 1 m.i.p.† is $4 \cdot 10^{-15}$C (24000 holes) which is amplified and shaped in steps by a preamplifier, an amplifier driver and a main amplifier to a 100 mV pulse as input for an 8-bit ADC. Gain adjustment is made with an external voltage. For triggering purposes the main amplifier delivers in parallel a digital ECL signal via an adjustable discriminator. In total 816 channels are read with this system.

† minimum ionizing particle.

4. THE TRIGGER, CALIBRATIONS AND DATA TAKING

4.1 The Trigger

The trigger employed in this experiment is an interaction trigger. This trigger has the advantage that it introduces only minimal biases. Furthermore no decay channel will be excluded by the trigger and thus a wide range of physics possibilities remain open for the analysis. The disadvantage of an interaction trigger is that no trigger enrichment of good events takes place before the events are written to tape. Thus the event selection will have to take place in the offline analysis.

The selection of interactions is done in two steps, the beam trigger and the interaction trigger.

1. The beam trigger itself is in turn split up into three steps. In the first step the total beam flux is measured with the scintillation counters B1 and B2 (see fig. 2.4)

   $$\mathrm{CONTROL} = \mathrm{B1}\bullet\mathrm{B2} \qquad (4.1).$$

   In the second step a coarse beam definition is made restricting the beam into a slit matching the size of the active target (AT) planes with a height of 1 mm and a width of 30 mm. Two scintillator counters are used here: B3 and the hole counter B4 (see fig. 2.4).

   $$\mathrm{UB1} = \mathrm{CONTROL}\bullet\mathrm{B3}\bullet\overline{\mathrm{B4}} \qquad (4.2).$$

   In the third step the beam definition is refined with the help of the Si micro-strip detectors BC4 and AT1 (fig. 2.4). The detector AT1 is employed to select one particle passing through the central 16 strips out of 48 in AT1. Clusters of neighbouring hits are taken here as only one hit (the so called cluster mode). The detector BC4 antiselects upstream interactions, vetoing events with hits in the 2 outer groups of 16 strips (out of 48 strips).

   $$\mathrm{UB2} = \mathrm{UB1}\bullet\overline{\mathrm{BC4(1\text{-}16,33\text{-}48)}}\bullet\mathrm{AT1(17\text{-}32)} \qquad (4.3).$$

   Before data taking the beam shape was optimized so as to maximize the ratio UB2/CONTROL.

2. The interaction trigger selects events which have a strip in the active target with a large (> 3 m.i.p.) pulse height (see section 3.4 on charge deposition by inelastic interactions). The strips used for this are the central 16 strips (out

of 48) of the active target planes 2 to 7. In addition, a charged particle multiplicity of three or more is demanded in the two downstream multiplicity counters (see fig. 2.5). This last requirement is made to exclude triggers in the target due to very energetic δ-rays, elastic scattering and diffractive interactions with low multiplicity which do not contain charm. As events with a detectable charm decay contain at least two charged tracks from the decaying particle, and very probably many more from the primary interaction or other decaying particles, a cut at three is still a very safe choice.

The trigger selection works now in two steps.

The first step is the trigger on strips with a high pulse height in the active target planes 2-7.

$$\mathrm{INT1} = \mathrm{UB2} \bullet \sum_{i=2,7} \mathrm{AT}_i^{(3)}(17\text{-}32) \qquad (4.4).$$

The second step adds the condition imposed on the multiplicity counters. One multiplicity counter plane provides a trigger demanding at least one strip with a pulse height of ≥ 3 m.i.p. ($\mathrm{MC1}_1^{(3)}$), the other a trigger demanding at least three strips with each a pulse height ≥ 1 m.i.p. ($\mathrm{MC2}_3^{(1)}$). These two conditions are put in a logical OR.

$$\mathrm{INT2} = \mathrm{INT1} \bullet (\mathrm{MC1}_1^{(3)} + \mathrm{MC2}_3^{(1)}) \qquad (4.5).$$

From the trigger rates given in table 8 one can conclude that the interaction trigger rate is 0.25%. Comparing this number with the expected rate (PDG1) of 0.37%, one has to correct for the loss of cross section due to three prong interactions (FLAM1), which are not accepted by the trigger. The expected rate is then 0.28% yielding a trigger efficiency of 88.4%.

Figure 4.1 displays the distribution of the charge sum over all strips in the planes for the interaction trigger. The peak at one m.i.p. is due to the beam particle before the interaction vertex in any of the planes 2-7. In these planes the beam signal gradually disappears. In these and following planes one sees the ionization due to the interactions and the interaction products.

The negative 200 GeV H6 beam contains 3.5% kaons (table 2.1). By reducing the number of pion interaction triggers with respect to the number of kaon interaction triggers, a sizable quantity of K^- induced interactions can also be recorded. Kaon interactions (MASTER1)are detected with the interaction trigger (INT2) and the signal

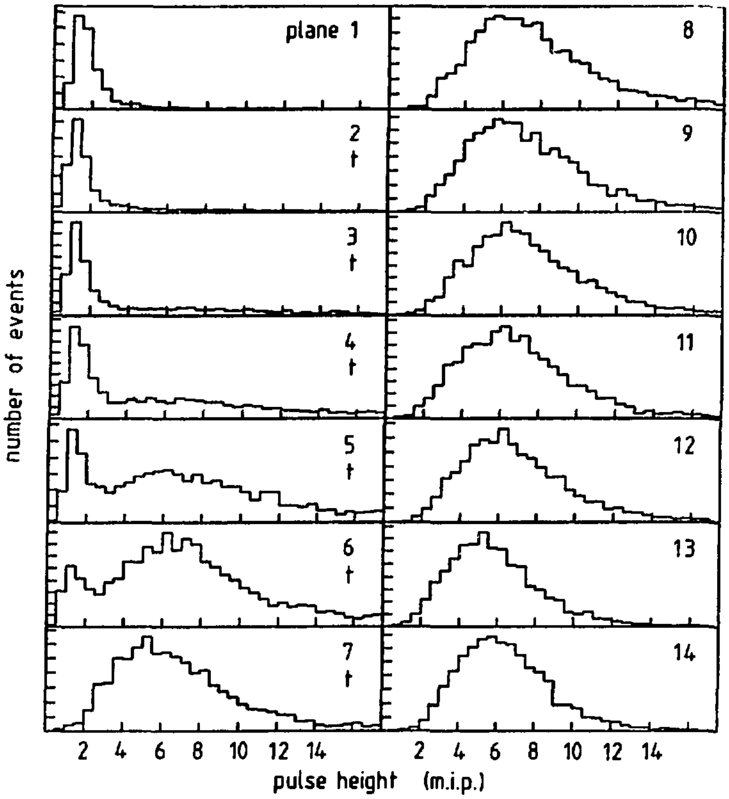

Fig. 4.1 The distribution of the total charge sum in the active target planes.
The shape of the distribution is explained in the text.

from the CEDAR1 Cerenkov counter in the beam line. All other interactions are labeled pion interactions. The pion interaction rate is artificially reduced by a coincidence with a random signal (MASTER2). The interaction trigger (TRIGGER) is taken as the OR between

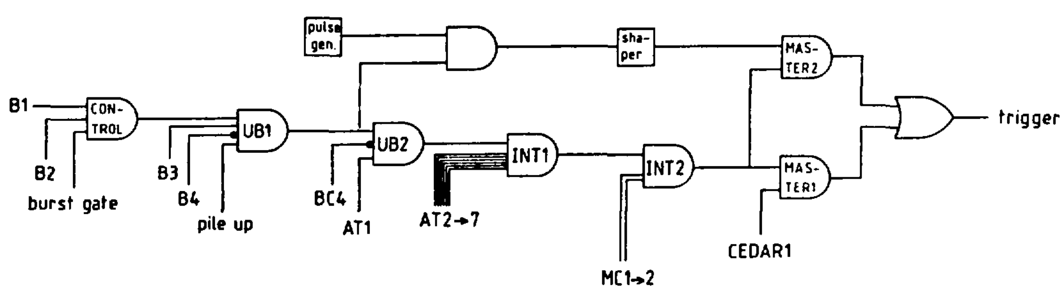

Fig. 4.2 The trigger scheme.

the kaon and pion interaction triggers. This evidently reduces the total trigger rate. For this reason the experiment was run with the highest possible beam intensity which still ensures a reliable drift chamber operation. With a data taking rate of 90% of the pion-only rate, the kaon interaction rate is 30% of the total interaction rate. Figure 4.2 shows a scheme with the complete trigger logic. In table 8 an example is given of the trigger rates.

Table 8: Example of trigger rates taken in 41 bursts of 2.5 sec duration.

	Number of triggers
CONTROL	70110488
UB1	64375601
UB2	48763884
INT2	119584
MASTER1	3707
MASTER2	10766
TRIGGER	14140
TRIG to tape	6681

4.2 The Calibration of Detector and Electronics

4.2.1 Introduction

In order to transform the signals of the tracking detectors into coordinates, several parameters of the detectors and their electronics have to be determined in advance. This calibration is split up into two phases for all detectors. The first phase is the calibration of the readout electronics, determining signal amplification factors and relative timing constants. The second phase is the calibration of the geometry, in which the positions of all the detectors are determined. These calibrations, using test pulse and beam track data, are performed at regular intervals during data taking.

4.2.2 The calibration of the electronics

Two types of readout electronics are employed in the apparatus. The first is a time digitization system used for the drift chambers. The second type are Analog to Digital Converters (ADC), which are used to measure the light production in the Cerenkov counters and the charge deposition in the Si detectors.

4.2.2.1 Drift chamber calibration

The drift chambers have a time digitization system for which the relative timing of the channels with respect to each other have to be determined (T0's). Details on the drift chamber system and its calibrations can be found in ref. DAUM1.

4.2.2.2 Cerenkov counter calibration

From the Cerenkov ADC's the zero readings (pedestals) and the gain factors of the photomultiplier-ADC chains have to be determined. Both are obtained from pulse height spectra in which the pedestal and the single photon signals stand out as distinct peaks.

4.2.2.3 The vertex microstrip detector calibration

The pedestals for the VMSD's are obtained by reading out empty events (no beam on target). The ADC signals in these empty events are averaged for each channel over 100 events. For monitoring purposes the standard deviations of the pedestals are also calculated and saved, as they contain the information on the noise level. The

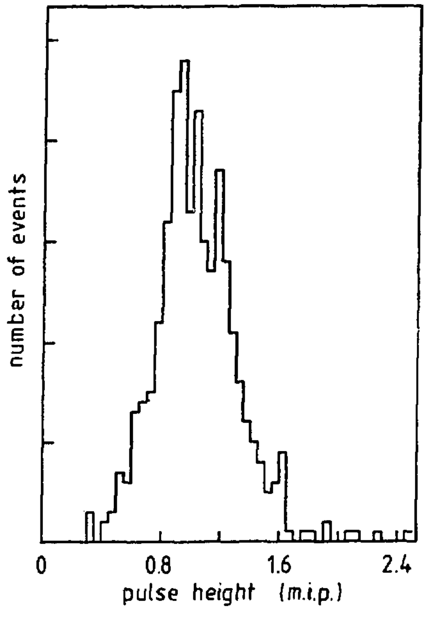

Fig. 4.3 VMSD gains calibration; distribution of pulse heights in clusters consisting of one strip only for beam track events.

determination of the gains is performed in two steps. In the first step, a fixed amount of charge is injected into the preamplifiers and read out with the ADC system. This test pulse, averaged for each channel over 100 events, provides the unnormalized gains for the VMSD's (HYAMI). The gains so obtained are determined relative to the strips in the same readout group to within 2%. In the second step the gains are normalized to the level of a minimum ionizing particle using beam track data. A defocussed beam is set to illuminate the VMSD telescope, and ~ 6000 beam passage events are written on tape. Offline the Landau charge distributions for the clusters which are contained in one strip are made. This is done separately for sections of the detector planes with strips which are grouped together in the readout chain. The determination of the peak values of these Landau distributions fixes the absolute level of the gains (fig. 4.3).

4.2.2.4 Active target calibration

The active target electronics chain is in several aspects different from the VMSD's (chapter 3). The faster components of the amplifiers and their very dense packing gives rise to more crosstalk between strips in the active target and a less optimal functioning of the test pulse system. The resulting noise level in the active target is 18% of a m.i.p., whereas the noise level in the VMSD's is only 3% of a m.i.p. The gains obtained using the active target test pulse system are only determined to within ± 10% of their optimum value, necessitating a long and complicated calibration of individual channels. The calibration of the gains is performed in three steps.

1. In the first step test pulse data are read out and averaged over 100 events, fixing the gains to within ~ 10%.
2. In the second step data are collected with a defocussed beam which illuminates the target uniformly, for recording the energy deposition from particles.
   The gains are extracted with the following algorithm.

- Clusters are encoded correcting for the gains from step 1. In each cluster the position of the strip with the largest pulse height is recorded as a hit.
- The beam track is reconstructed making use of these hits in the 14 active target planes.
- In each plane the strip with the largest pulse height in the 3 strips surrounding this beam track is taken for calibration.
- With these pulse heights an average is calculated for each strip in the target.

This method uses the feature that the Landau tail is caused mostly by energetic δ-electrons, emitted at high angles, which have a long range and can deposit their energy accordingly over more strips. In detectors with 20 μm strip pitch the charge distribution loses the Landau tail, when only the pulse height of the strip with largest pulse height in a cluster is taken. This method will result in gains ~ 20% lower than the m.i.p. level, as the ionization due to short range electrons is in most cases shared by two strips (fig. 4.4a).

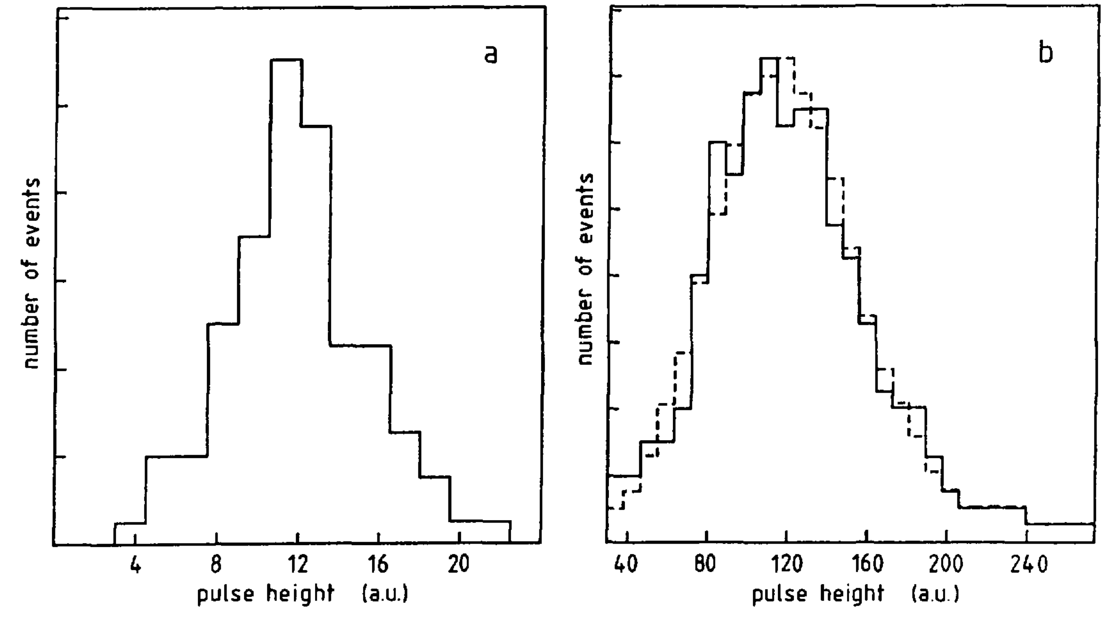

Fig. 4.4 Active target gains calibration.
a) Distribution of the pulse height of the strip with the largest pulse height around the beam track after correction with gains factors as found with the test pulse system.
b) Distribution of the pulse height in a cluster after correction for relative gains for individual strips. The broken line represents the fit to a Landau distribution convoluted with a Gaussian distribution.

3. In step 3 the gains are normalized to the minimum ionizing particle level using the same beam track algorithm as for step 2, but now the gains obtained in step 2 are used. For each plane the pulse heights in the cluster are added and subsequently the distribution of the sums of these pulse heights is fitted with a Landau distribution convoluted with a Gaussian (see section 3.2). The peak value determines the normalization of the gains (fig. 4.4b).

4.2.3 The calibration of the geometry

The calibration of the geometry is an essential first step in the analysis. The resolution of the tracks reconstructed as well as the track finding efficiency depend closely on the knowledge of the exact position and orientation of the detectors. The spatial resolution of the tracks determines the momentum resolution and the secondary vertex resolution. The calibration consists of two phases, the optical (hardware) and the software alignment.

4.2.3.1 Optical alignment

The optical alignment is the actual positioning of the detectors, which is done or checked before each data taking run. The magnets and Cerenkov counters are aligned by reading their positions with respect to a ruler fixed on the floor of the experimental hall. The drift chambers are positioned perpendicular to the beam direction (X-Y plane) and are aligned with respect to beam axis in both horizontal (X) and vertical (Y) directions. Their longitudinal positions (Z) are determined with the help of an optical pointer system, which is again refered to the ruler on the floor.

The target area is aligned in two steps. First the Si detectors are positioned on an optical bench (see section 3.5), then this internally rigid assembly of bench and detectors is positioned with respect to the rest of the spectrometer. The errors on the positions of all components (the target table is seen here as one component) is ~ 1 mm.

4.2.3.2 Software alignment

The second phase in the calibration is the software alignment in which the positions obtained with the optical alignment are fine tuned. Using coordinates obtained with the nominal positions of the detectors as found in step one, tracks are fitted in the detectors, leaving out detectors successively. The distances of single coordinates to this fitted track are plotted for each detector. The peak positions of these residuals' distributions are used to redefine the positions of the detectors. This procedure is repeated several times to obtain the optimal position. For the drift chamber system this procedure has been extensively described in refs. SPIE1 and PETE1. After the drift chambers have been aligned, the silicon detectors on the target table are adjusted with respect to the drift chamber system.

This software fine tuning can only be done in directions perpendicular to the beam axis. The Z-positions obtained in the hardware phase are not changed. The alignment quality can be monitored from the distributions of the residuals from the tracks fitted at the end of the procedure. Figure 4.5a shows a typical distribution of residuals for the drift chambers. The alignment of these chambers can be performed with a precision of 40 µm. Figure 4.5b shows a distribution of residuals for a VMSD detector. The precision here is 4.0 µm.

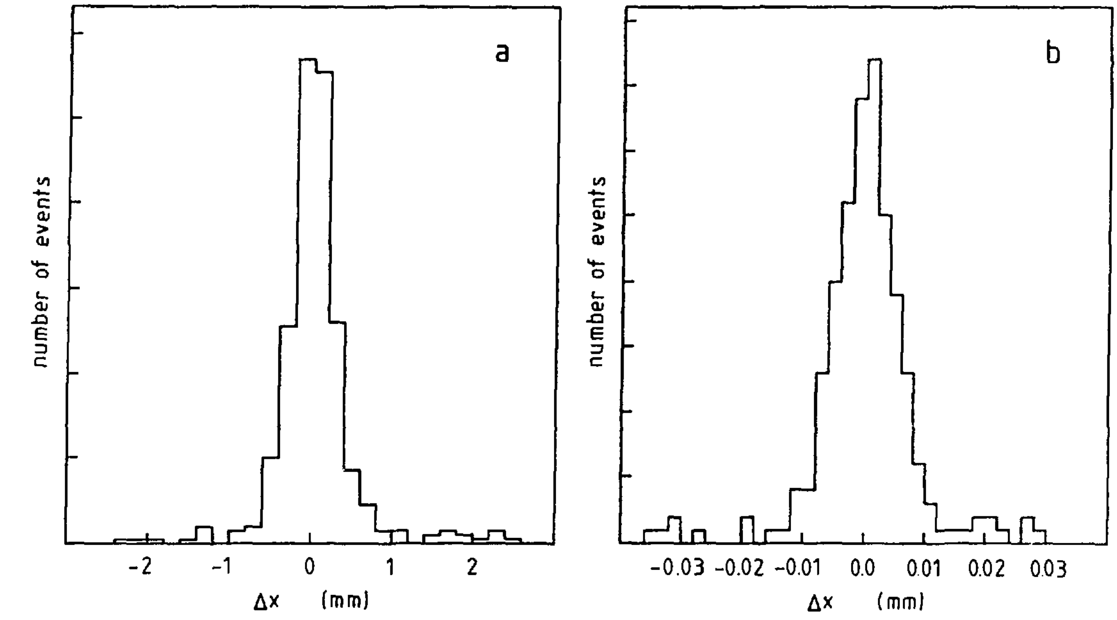

Fig. 4.5 Calibration of the geometry.
a) Distribution of residuals of drift chamber coordinates with respect to a beam track fitted with the other drift chambers.
b) Distribution of residuals of VMSD detector coordinates with respect to a beam track fitted with the other VMSD's.

4.3 Data Taking and Data Sample

The events passing the trigger are read out via CAMAC into the NORD 100 data acquisition computer and written onto tape. The data acquisition rate is ~ 160 events written to tape per burst of 2.5 s. At this speed a 6250 bpi tape is full in 35 minutes. The average readout time per event is 15 ms. Table 9 shows a breakdown of the averaged event length for the various detector systems.

During data taking the performance of the detectors and the trigger can be checked with a system of monitoring programs on the NORD 100 computer. For every burst several events are stored in a buffer in the NORD 100 which can be accessed by the monitoring programs. The programs display diagnostics' information on e.g. hit maps of detectors, ADC spectra, cluster properties and drift times.

The data taking took place in the spring and summer of 1984. The data analysis described in this thesis was performed on $5.\bullet 10^6$ events with incoming K^- and $7.9\bullet 10^6$ events with incoming π^- at 200 GeV momentum. The complete data sample contains an additional $14.\bullet 10^6$ events with incoming π^- and $11.\bullet 10^6$ events with incoming p^+, both at 200 GeV beam momentum. The analysis of these data is still in progress.

Table 9: Average event length for the various detector systems

detector system	average # words (16 bits)
drift chambers	601
VMSD's	504
active target	416
γ cal. + Cerenkov 48 bits ADC	95
γ cal. 8 bits ADC	480
general*	215

* all other information : Cerenkov digital readout, trigger bits, etc.

5. TRACK RECONSTRUCTION AND EVENT SELECTION

5.1 Introduction

The offline event reconstruction comprises track reconstruction in Si detectors and drift chambers, particle identification with the Cerenkov counter hodoscopes and secondary vertex reconstruction with the tracks. The average time used for the full reconstruction of an event is ~ 4 s/event (IBM 370/168 equivalent time). To reduce this work load, the event reconstruction is split up into steps; these steps include selection criteria. When events fail these criteria, they are rejected for further reconstruction. In this way, a work load reduction is achieved, as the rejected events do not require any further attention. Figure 5.1 schematically depicts the reconstruction and selection steps which are also listed below.

1. Decoding of the raw data into physical quantities.
2. Reconstruction of the incoming beam trajectory in the beam telescope.
3. Reconstruction of the primary interaction vertex in the active target.
4. Preselection. Tracks are reconstructed in the vertex telescopes in projections. Events are selected which have at least 2 tracks in projections which do not point back to the primary interaction vertex.
5. Drift chamber track reconstruction. Using DC coordinates, track segments are reconstructed in the arms of the spectrometer. These track segments are matched to each other. A momentum measurement of the track is obtained with a fitting procedure.
6. Particle identification. Using the drift chamber tracks and their momenta, the Cerenkov counter information is employed to assign a particle probability (pion, kaon or proton) to the track.
7. Microtrack reconstruction. With the drift chamber tracks as a guide, tracks are reconstructed in the vertex telescope using the coordinates from the Si microstrip detectors.
8. Secondary vertex reconstruction. A secondary vertex search is done with the tracks as found in the vertex telescope. The search is restricted to those tracks which form an invariant mass in a window around the charm region.

In the following sections these steps will be described in more detail.

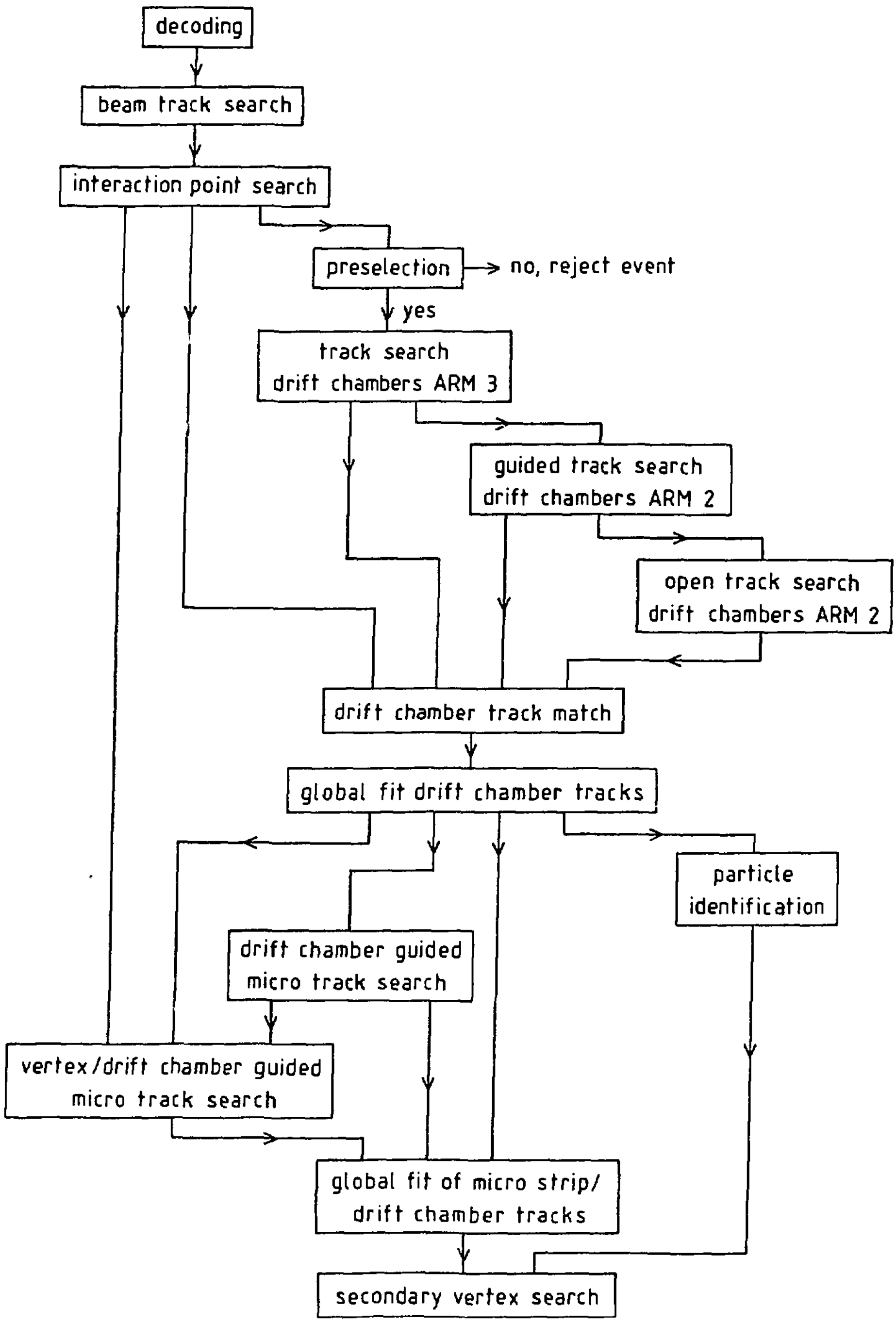

Fig. 5.1 The reconstruction and selection steps in the analysis.

5.2 Decoding of the Raw Data

Before track reconstruction can be started, the raw data have to be decoded into physical quantities like coordinates, quantities of charge or number of photoelectrons. For most detectors like drift chambers and Cerenkov counters these procedures have been described elsewhere (DAUM1, SPIE1). For the Si microstrip detectors, the procedure is complicated by the high track density near the vertex which may cause overlaps in the charge clouds deposited by adjacent tracks. We shall therefore describe the decoding procedure for the Si detectors here in some detail. The coordinate attribution for the Si detectors is done in three steps.

1. In the first step the ADC information is ordered and the signals are normalized into units of minimum ionizing particles (m.i.p.) for each strip.

2. In the second step clusters are searched for among the signals in each detector plane. A cluster is a group of adjacent strips which contain charge signals from tracks. Strips outside clusters are presumed to contain no signal. In a cluster all strips have a pulse height ≥ 0.06 m.i.p. and each pair of neighbours shares a pulse height of at least 0.5 m.i.p. Clusters consisting of only one or two strips are already accepted when they contain a total pulse height ≥ 0.25 m.i.p.

3. The third step forms the calculation of coordinates from the clusters found in step two. The detectors are very near to the interaction vertex and the coordinates are measured in only one projection per detector plane. Thus many tracks cause overlapping clusters. Due to the Landau fluctuations in the amount of ionization and hence the detected charge, it is not possible to attribute with certainty the exact number of coordinates, i.e. the exact number of m.i.p.. To obtain the best solution in a wide range of cluster configurations, the clusters are categorized in size and total pulse height. The lower cut off values for the multiparticle Landau distributions determine the number of coordinates attributed to a certain pulse height. Each cluster category is treated separately according to the number of strips and the total pulse height.

- Single strip clusters are given a coordinate at the centre of the strip. Multiple coordinates due to high pulse heights are put at the same position.

- In two and three strip clusters the coordinates are determined with a "centre of gravity" method. This is done after an attempt to cut the cluster down to a two strip cluster by removing an outer strip with a pulse height smaller than 0.2 m.i.p. If in both outer strips the signals are smaller than 0.2 m.i.p. we retain the strip with the larger pulse height.
- For clusters over 4 strips or more, we try to make a split into subclusters. Strips with a pulse height lower than 0.2 m.i.p. are taken as subcluster boundary. The subclusters of one, two and three strips are treated in a similar way as above. In the remaining 4 and more strip (sub)clusters the coordinates are evenly divided such that, at each interstrip gap, at least one coordinate is attri- buted. The number of coordinates attributed to each interstrip gap depends on the sum of pulse heights in the two surrounding strips.

The errors to be assigned to the coordinates are determined in an empirical way. We search for and fit tracks (see section 5.8), leaving out each detector plane in turn. The distance of the track to the selected coordinate in this detector plane is plotted. This is done separately for each category of co-ordinates. The standard deviations of these distributions are taken as errors on the coordinates. The shape of these distributions also provide a check whether the choice of the categories was correctly done (see fig. 5.2).

5.3 The Reconstruction of the Beam Trajectory

The incoming beam trajectory is registered by the detectors of the beam telescope and the active target (figs. 2.4 and 2.5). Offline this trajectory is reconstructed, using the coordinates as provided by the decoding routines. The reconstructed beam trajectory (from now on called beam track) will later on be used to find the interaction vertex in the active target. The beam track alone will determine the X,Y coordinates of this inter-action vertex. Before describing the reconstruction algorithm, it is useful to reiterate the strip orientation of the beam detectors and the active target planes (see figs. 2.4 and 2.5 and tables 2 and 3 in chapter 2).

- BC1 and BC4 are active target type detectors with horizontal strips.
- BC2 and BC3 are VMSD type detectors with strips at ±14° with the hori-zontal.
- The beam hodoscopes BB1 and BB2 have horizontal and vertical strips res-pectively.
- The active target has horizontal strips.

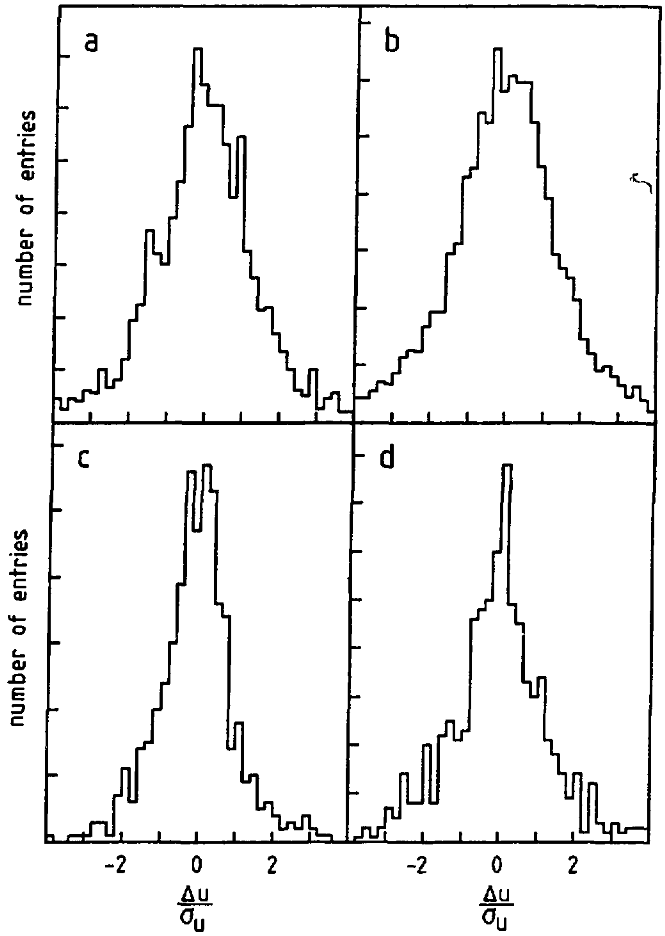

Fig. 5.2 Distributions of the deviations of predicted and measured coordinates normalized to the errors for 4 types of clusters in the 60 μm readout regions. a) one strip, one m.i.p., b) two strips, one m.i.p., c) two strips, two m.i.p., d) three strips, two m.i.p.

The reconstruction is done as follows. Coordinates are first selected in the detectors of the beam telescope and subsequently used in a track fit. The minimum set of coordinates required for a track fit are two X coordinates and two Y coordinates. When more coordinates are available, they will also be selected. The detectors BC2 and BC3 are each required to supply one coordinate, giving effectively one X,Y pair. Plane BC4 and the first four planes of the active target have to supply together one Y coordinate. In these 5 detectors the Y coordinate with the best resolution is selected for the fit. The additional X coordinate is obtained either from the beam hodoscope BB2 or, when no hits are present there, from the extrapolation of the X obtained with BC2 and BC3 assuming a track slope in in the X-Z plane of zero and a large error. With this minimum set, it is not possible to resolve ambiguities due to multiple coordinates in one detector. In reality only BC2 and BC3 can have multiple coordinates due to additional beam particles passing through the same long (1 µs) ADC gate pulse used for these detectors. These ambiguities can be solved using additional Y coordinates supplied by BB1 or BC1. In the case that the ambiguities cannot be resolved, the event is rejected for further analysis. When enough coordinates are avail- able, they are required to lie within a distance of 60 µm from a straight line. The second step in the reconstruction is a straight line fit through these coordinates. Figure 5.3 shows the X and Y resolutions histograms of the reconstructed beam track. In table 10 the event rejection in the beam track reconstruction is split up in the various categories.

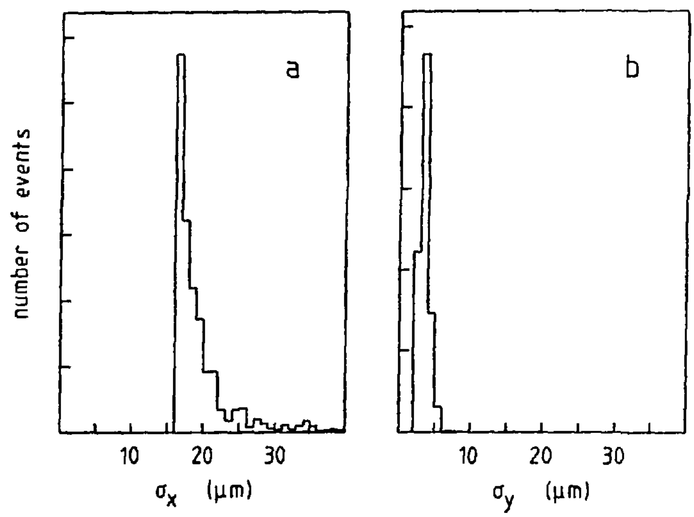

Fig. 5.3 The resolution of the beam track at position AT3. a) in X, b) in Y.

Table 10: The beam track reconstruction, event losses

	rejected events (%)
No hit found in BC2 or BC3	1.7
No good hit found in BC4 or AT1-4	1.9
No additional hit found in BC1 or BB2 to solve ambiguities	1.7
No straight line through coordinates	0.9
Unresolvable ambiguity in BC2 or BC3	2.4
Total rejection	8.6

5.4 The Reconstruction of the Primary Interaction Vertex

The interaction vertex is reconstructed on the basis of a pulse height analysis of the signals in the active target. Using the beam track as a guide, the beam is followed through the active target. Going from one plane to the next, one looks in a window of eight strips (= 160 μm) around the extrapolated beam position in the previous plane to locate the charge signal from the beam particle. The interaction is detected if a pulse height is encountered larger than 2 m.i.p., followed in the two consecutive planes by a pulse height larger than 2.5 m.i.p. in windows of respectively 7 and 13 strips around the beam position. For the choice of the interaction plane, one can distinguish 3 cases.

- Plane N : 2.0 m.i.p. < pulse height in window < 2.5 m.i.p.;
  plane N + 1 : pulse height in window < 2.5 m.i.p.;
  plane N + 2 : pulse height in window contains an overflow. Plane N+2 is taken as the interaction plane.
- Plane N : 2.0 m.i.p. < pulse height in window < 2.5 m.i.p.;
  plane N + 1 : pulse height in window > 2.5 m.i.p. Plane N+1 is taken as the interaction plane.
- In all other configurations the first flagged plane (pulse height in window > 2.0 m.i.p) is taken as the interaction plane.

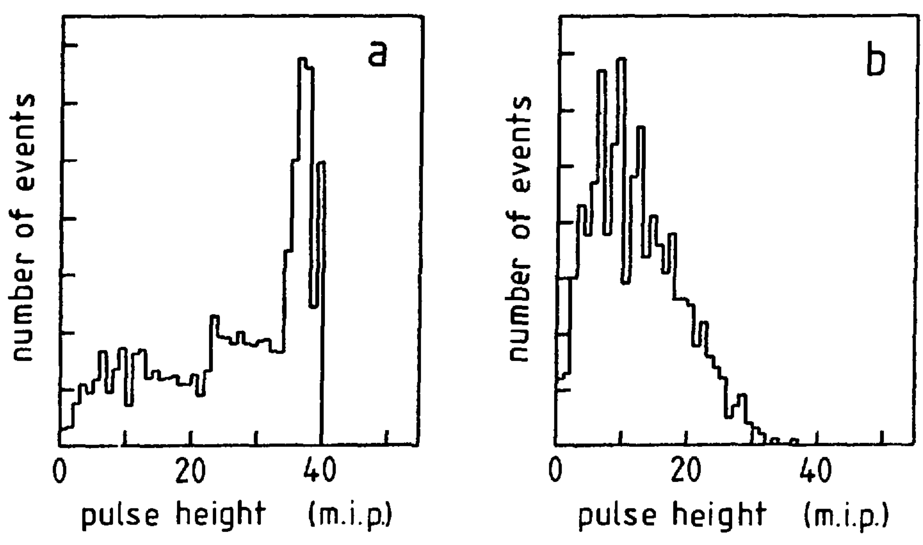

Fig. 5.4 a) The distribution of the sum of the charge in the three strips surrounding the interaction vertex.
b) The same, but omitting the events which have an overflow in one of the three strips (see text).

The distribution of the charge sum of the three strips surrounding the interaction vertex thus found may be seen in fig. 5.4. An overflow in the target will on average correspond to 11 m.i.p. for the calibration used. In fig. 5.4a one may distinguish the pulse heights at which two and three strips contain an overflow.

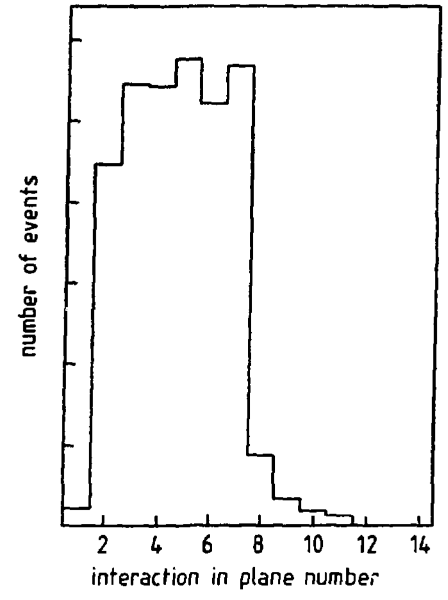

Fig. 5.5 The distribution of interactions over the active target planes.

In 3% of the events, no interaction being found in the active target, it was checked that these events are due to false interaction triggers. Figure 5.5 shows the distribution of the interactions over the active target planes. The online trigger also accepts interactions which take place in the plane in front of the trigger planes (AT1), as interactions in AT1 can also produce strips with high pulse heights in the trigger planes (AT2-AT7). Backscattering of heavy or slow particles originating from planes behind the trigger planes can also produce strips with high pulse heights in the trigger planes and thus trigger such an event. The position perpendicular to the beam direction (X,Y) is obtained by refitting the beam track. The coordinates used for the refit are the ones taken for the beam reconstruction (section 5.2) with, in addition, all coordinates on the beam in the target detectors more than two planes before the interaction plane. The resolution of the interaction vertex in X and Y is that of the beam track at the Z-position of the centre (in Z) of the target plane. The resolution along the beam (in Z) is given by $280\ \mu m/\sqrt{12}$, where the thickness of an active target plane is 280 µm.

5.5 Preselection

5.5.1 Introduction

In order to reduce further the total computer time needed for the event reconstruction, an event selection has to be performed at an early stage of the analysis, i.e. before the drift chamber track reconstruction is executed. Due to a lifetime of $O(10^{-13}$ - $10^{-12})$s, charmed particles will decay after having travelled a small distance. The probability of a particle to traverse a distance larger than ℓ before decaying is :

$$P(\ell) = e^{-\ell m/p\tau_0} \qquad (5.1),$$

with: m = the mass of the particle,

p = the momentum of the particle,

τ_0 the proper mean lifetime of the particle,

c = the velocity of light.

In fig. 5.6 those probabilities are displayed for D^0 and D^+ for several momenta.

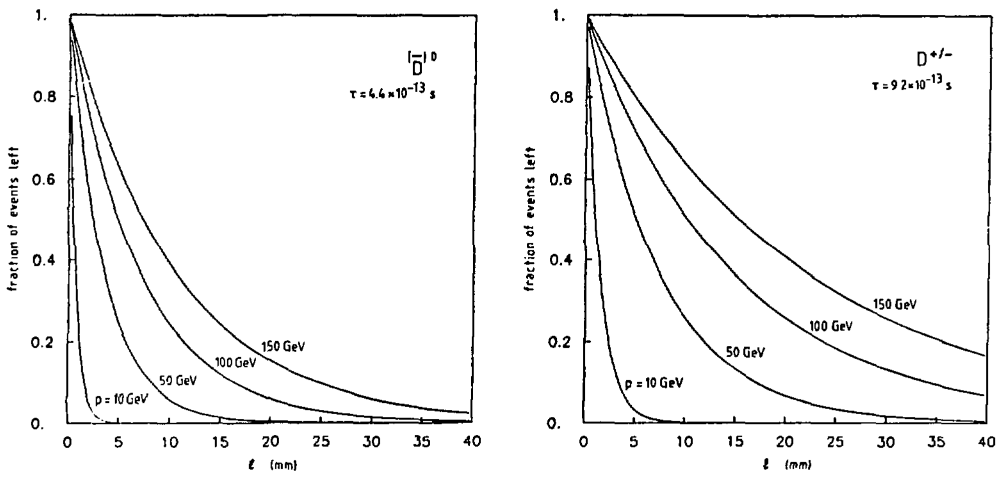

Fig. 5.6 The decay curves for a) D^0 and b) D^+ for 4 different momenta. The lifetimes used are from the 1984 PDG (PDG1).

The decay tracks from the charmed particles thus do not originate from the primary interaction vertex. This feature is exploited in two different ways to provide a preselection of the events. In the first preselection, events are selected which have tracks which miss the primary vertex when extrapolated backwards from the vertex telescope, the so-called impact parameter preselection. The second preselection looks for events which exhibit a sudden jump in the charged particle multiplicity in the active target. Events passing any of the two preselections are passed on for further analysis. In the total preselection, 34% of the total events sample are selected. In the following subsections, we will describe both preselections and assess their efficiency for selecting charm decays.

5.5.2 Preselection on Impact parameter

As in the strong interaction between the beam particle and the nucleons of the Si nucleus the quantum number charm is conserved, only charm-anticharm quark pairs can be produced. When this pair does not form a bound state, the event will contain two charmed particles. We will now make an estimation of the distance at which the decay tracks will miss the primary vertex when extrapolated backwards. In fig. 5.7 some of the quantities in this calculation are defined.

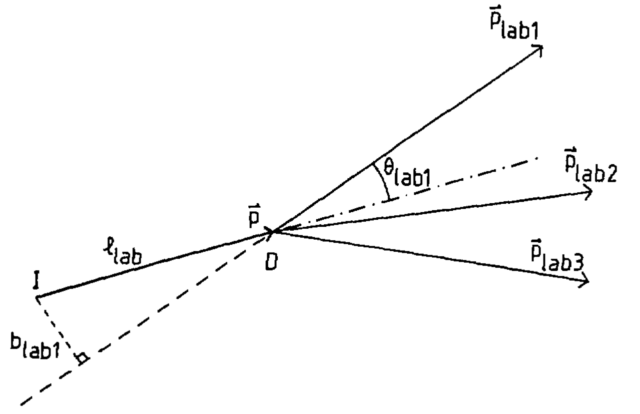

Fig. 5.7 Definition of symbols for impact parameter calculation.
I Interaction vertex, D decay vertex.

The distance b_{lab} will from now on be called the impact parameter. The sub- script "lab" indicates that the value is taken in the laboratory system, "cm" indicates the rest system of the decaying charmed particle. We can write :

$$b_{lab} = \ell_{lab} \sin\Theta_{lab} \qquad (5.2),$$

with:

$$\sin\Theta_{lab} \approx \tan\Theta_{lab} = p_{cm}\sin\Theta_{cm}/(\gamma p_{cm}\cos\Theta_{cm}+\beta\gamma E_{cm}) \qquad (5.3),$$

and:

p_{cm}	=	the momentum of the decay particle,
E_{cm}	=	the total energy of the decay particle,
Θ_{cm}	=	the angle with respect to the line of flight of the decaying particle,
β	=	the velocity of the decaying particle in the lab system relative to c, the speed of light
γ	=	$1/\sqrt{(1-\beta^2)}$.

The relation between the decay distance in the lab system and the proper lifetime t of the decaying particle is :

$$\ell_{lab} = \beta\gamma ct \qquad (5.4),$$

For $p_{lab} > 20$ GeV : $\beta \approx 1$, thus :

$$b_{lab} = ct\, p_{cm}\sin\Theta_{cm}/(p_{cm}\cos\Theta_{cm}+E_{cm}) \qquad (5.5),$$

With charmed momenta > 20 GeV the impact parameters of the decay tracks are thus independent of the momentum of the decaying charmed particle. For the two body decay $D^o \rightarrow K^-\pi^+$ the maximum impact parameters for a lifetime of $t = \tau_0$ are for π and K 120 µm and 103 µm respectively. The impact parameter is linear in the lifetime of the particle t, so we may expect impact parameters of the order of 50-500 µm for two body decays. For three and more body decays not all decay particles will have a large impact parameter.

In the event preselection events are accepted which have two or more track projections in the vertex telescope which do not point back to the primary interaction vertex.

The reconstruction of track projections in the vertex telescope is done in four steps, starting with the easiest tracks and successively going on to the more difficult cases. Each of the steps is executed for the two full projections of three detectors in the vertex telescope. In the first three steps a guide line is constructed connecting two coordinates or a coordinate and the vertex. After this the coordinates in the other planes are only considered if they lie within a distance of 0.2 mm from this guide line and have not previously been used for another track. The final criterion for accepting a track projection is a straight line fit with a cut on the resulting χ^2. This χ^2 is the square of the distances of the coordinates to the fitted track weighted for the coordinate errors. After accepting a track its coordinates are deleted to prevent multiple use of coordinates. The four steps are as follows.

1. Reconstruction of tracks which point back to the primary interaction vertex and have a hit in each of the three detectors of the projection.
For accepting the track the χ^2 (named χ^2_3, number of degrees of freedom NDF = 3-2) from the straight line fit of the three coordinates should be less than 8, corresponding to a cut on 2.8 standard deviations (σ). The pointing back condition is investigated by performing a straight line fit through the three coordinates and the interaction vertex. This fit yields a χ^2 (named χ^2_4, NDF = 4-2). To accept a track as pointing, it is demanded that $\chi^2_4 - \chi^2_3 < 8$, which corresponds to a cut on 2.4 σ.

2. Reconstruction of tracks which point back to the primary interaction vertex and have a hit in the first two detectors of the projection, but miss the third detector of the projection.
Such a track is accepted when a straight line fit of the two coordinates and the vertex yields a χ^2 less than 8.

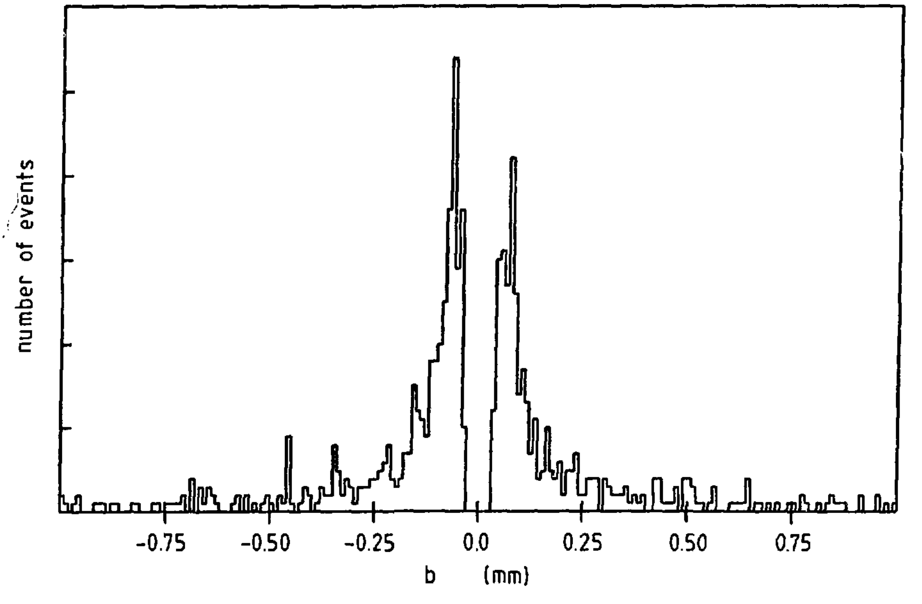

Fig. 5.8 The impact parameter distribution for the tracks classified as non-pointing.

3. Reconstruction of tracks which do not point back to the primary interaction vertex and have a hit in each of the three detectors of the projection.
   The track is accepted when a straight line fit through the three coordinates yields a χ^2 less than 8. The impact parameter with the primary vertex is demanded to be less than 2.0 mm, to prevent the reconstruction of unphysical tracks.

4. Reconstruction of tracks which do not point back to the primary interaction vertex, have a hit in the first two detectors of the projection and do not cross the active area of the third detector.
   Tracks are accepted when their impact parameter with the primary vertex is less than 1.5 mm.

After reconstruction in the two projections of the vertex telescope, the tracks reconstructed in steps one and two are discarded, as they are considered pointing. The tracks reconstructed in step three are subjected to a tighter non-pointing condition in order to arrive at a substantial event reduction in the preselection. The criterion for a non- pointing track to participate in the preselection is that $\chi^2_4 - \chi^2_3 > 15$. We take as an approximation that the $\chi^2_4 - \chi^2_3$ distribution has the same behaviour as a χ^2 distribution of one degree of freedom. The applied cut of 15 then corresponds to a cut on

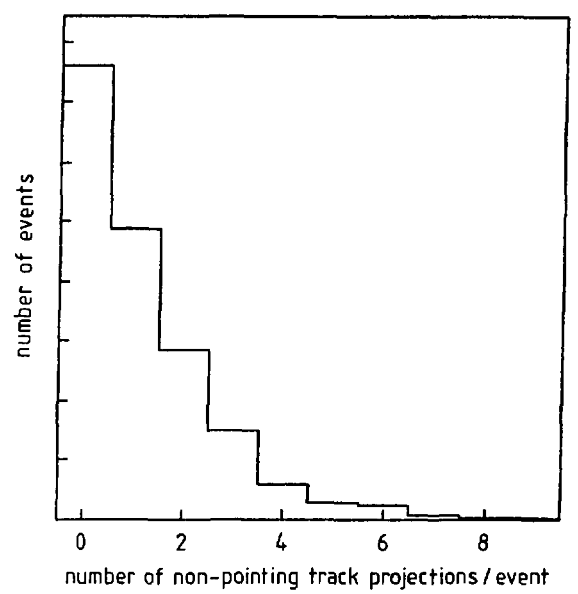

Fig. 5.9 The number of tracks per event in projections classified as non-pointing by the preselection.

tracks having an impact parameter with the primary vertex larger than 4 σ. Tracks reconstructed in step four are always taken for the preselection. In fig. 5.8 the impact parameters for the selected tracks are plotted. From fig. 5.8 it can be clearly seen that the 4 σ cut on $\chi^2_4 - \chi^2_3$ introduces an effective impact parameter cut of 30 µm. Figure 5.9 shows the number of tracks classified as non-pointing per event. The event sample is reduced to 31% in this preselection step by demanding at least two tracks in projection to be non-pointing.

5.5.3 Preselection on a jump in the charged multiplicity

This preselection uses the information supplied by the active target and multiplicity counters. It selects events which exhibit an effective jump in the charged particle multiplicity of 2 m.i.p. in the active target. For this the signal clusters in the multiplicity counters and the interaction vertex are used to predict charge patterns in the active target. These charge patterns, series of signals in neighbouring planes caused by the same particles, are examined for multiplicity steps. A total multiplicity increase of 2 m.i.p. is required for selecting an event. This preselection accepts 3% of the events.

5.5.4 The efficiency of the preselection

The first preselection can exhibit an inefficiency with respect to the final analysis (section 5.8), where the tracks are reconstructed in space, using 2 full projections with 3 VMSD counters each plus a counter with horizontal strips. Furthermore, the final reconstruction is guided by the drift chamber tracks. These extra facilities prevent the reconstruction of unphysical (ghost) tracks or distorted tracks and thus leave the coordinates for use with other correct tracks. The second preselection on charged multiplicity jumps in the active target will overcome most of the efficiency problems at low decay distance where the effect is expected to be worst. In order to check the efficiency of the preselection for tagging charmed particle decays which pass the impact parameter requirements a comparison was done of the number of K^0 decays found in events accepted by the preselection and events rejected by the preselection. The K^0 tracks were reconstructed with a program analogous to the final charm analysis program discussed in sections 5.8 and 5.9. The K^0's were required to have two track projections which miss the primary vertex by 4 σ. The results are summarized in table 11.

Table 11: Measured inefficiency of finding a K^o decay due to the preselection as function of the decay distance

Δz (mm)	inefficiency (%)
0 - 5	0. ± 2.
5 - 10	5. ± 2.
10 - 15	8. ± 2.
15 - 20	9. ± 2.
20 - 25	8. ± 2.
> 25	7. ± 2.

These inefficiencies are in fact an upper limit to the true inefficiencies as the preselection tags events with non-pointing tracks, which do not necessarily come from the particular decays to be selected. The decrease in inefficiency at decay distances of 0-5 mm is due to the second preselection on charge jumps in the active target. We conclude that the preselection gives no appreciable loss or bias on the charm decays reconstructed with the final selection program.

In table 12 all event rejection factors are listed which occurred up to now in the analysis. The average computer time spent per event up to this point is ~ 0.6 s/event (IBM 370/168 equivalent time).

Table 12: Event rejection in the first 3 analysis steps

	rejection rate (%)	cumulative rejection rate
decoding	2.5	2.5
beam track reconstruction	8.8	11.1
interaction vertex search	3.0	13.8
preselection	66.0	71.7

5.6 Track Reconstruction in the Drift Chambers

The track reconstruction in the drift chambers of the spectrometer is done in a program called ELFPRO. The program ELFPRO has been extensively described previously in refs. PETE1, SPIE1 and DIJK1. The reconstruction proceeds in three steps.

1. First, track segments are reconstructed in the parts of the spectrometer where no magnetic fields are present, and thus are straight lines. The field free parts where the drift chambers are located are called ARMs (see fig. 2.2a). A track traversing the complete spectrometer, i.e. which originates from the target area and leaves the spectrometer through the last (ARM3c) drift chamber, possesses one segment in the ARM2 drift chambers and one in the ARM3 drift chambers (see fig. 5.10). The track search is started in ARM3. As the track multiplicity in ARM3 is lower than in ARM2, the ARM3 search will be faster due to the smaller number of coordinates to be considered. The track segments reconstructed in ARM3 are subsequently used as guidance for the search in ARM2 to restrict the search volume and thus to save time. After the guided ARM2 search a free ARM2 search is done with the still unused coordinates in ARM2. The track segments in ARM2 and ARM3 are separately fitted with straight lines.
2. When all track segments have been found and fitted a search for matches is made between the ARM2 and ARM3 track segments. For all ARM2 and ARM3 segments the crossing point with the central plane of the BBC magnet is calculated using a straight line extrapolation. The matching segments from ARM2 and ARM3 cross, within errors, at common points. For segments in ARM2 which do not enter the gap of the BBC magnet and segments in ARM2 and ARM3 to which no matching partner can be found it is checked whether they point back to the primary interaction vertex in the Y-Z plane in which no magnetic deflection takes place. This last match takes into account the

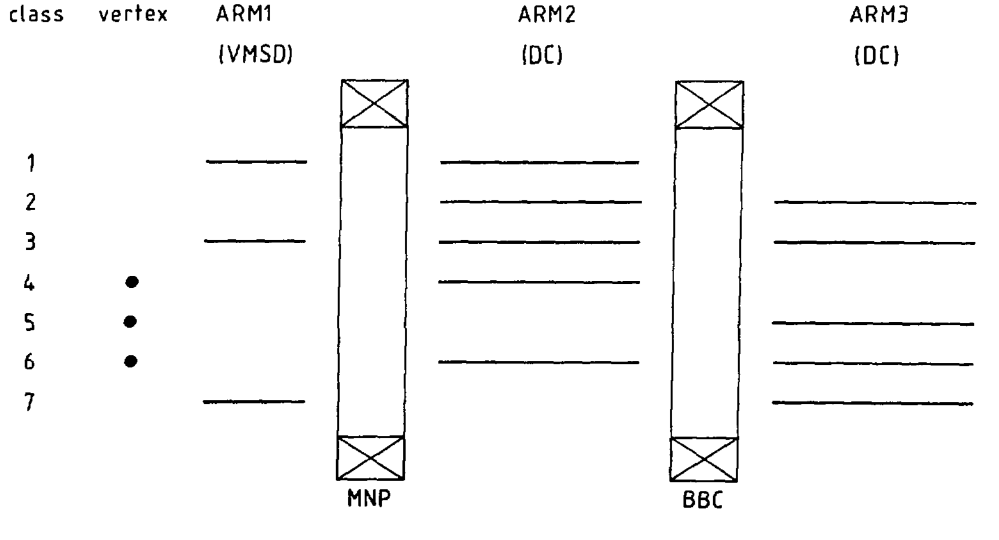

Fig. 5.10 The possible configurations of track segments in the spectrometer.

possible offset of tracks by several centimeters from the primary vertex due to decaying particles originating from a decay at a displaced secondary vertex. The reason for the absence of matching track segments is the high beam intensity, due to which a narrow cylindrical region in the drift chambers (radius ~ 1 cm) around the traversing non-interacting beam is made in- sensitive by the accumulated space charge. Tracks crossing this insensitive region can escape reconstruction in an ARM.

3. The last step in the drift chamber track reconstruction is a fit of the matched track segments or the single matched segments to the primary interaction vertex.
   Leftover track segments are not used any further in this analysis.

The result of the fit is a unit direction vector $\hat{p}$ of the track in the target area, an associated momentum p and the charge polarity q of the particle. A track is then defined by 7 parameters: X, X' = dX/dZ, Y, Y' = dY/dZ, Z, p and q. The errors on the track position, direction and momentum and the correlation between the errors are represented by the covariance matrix. This matrix has 15 independent elements :

$$\begin{pmatrix} \mathrm{var}(X,X) & \mathrm{covar}(X,X') & \mathrm{covar}(X,Y) & \mathrm{covar}(X,Y') & \mathrm{covar}(X,p) \\ & \mathrm{var}(X',X') & \mathrm{covar}(X',Y) & \mathrm{covar}(X',Y') & \mathrm{covar}(X',p) \\ & & \mathrm{var}(Y,Y) & \mathrm{covar}(Y,Y') & \mathrm{covar}(Y,p) \\ & & & \mathrm{var}(Y',Y') & \mathrm{covar}(Y',p) \\ & & & & \mathrm{var}(p,p) \end{pmatrix} \quad (5.6).$$

The resulting tracks and momenta are used as guidance for the track reconstruction in the vertex telescope. After finding the track segments in the vertex telescope a global refit will be performed reusing the track segments yielding a more precise momentum measurement (section 5.8). The configurations of segments which can form tracks are depicted in fig. 5.10. The momentum resolutions for the tracks of different configuration are given in table 6 of chapter 2.

5.7 Particle Identification

The Cerenkov counter hodoscopes are used to identify the particle on a track and thus to attribute a mass to the particle tracks (see ref. SPIE1). For the identification of the particles with the Cerenkov counter hodoscopes one calculates the expected number of photoelectrons for each track in each Cerenkov hodoscope for the particle hypotheses:

proton, kaon and pion. The errors on these quantities can be calculated from the statistical significance of the photoelectron signal and the experimental detection errors. Using the measured number of photoelectrons in a counter, the probability can be calculated that the track is a proton, a kaon or a pion. The results for all counters which are traversed by a track are multiplied :

$$P_j = \prod_i P_{ij} \qquad (5.7)$$

with: j = p,K,π: the particle hypothesis,

i = the Cerenkov counter hodoscope traversed by the track.

The light produced by several particles which overlaps in one mirror and light originating from one particle covering several mirrors are taken account of in this analysis. The interpretation of the probabilities for the invariant mass calculation is based on a comparison of the final probabilities for the three particle types. For some tracks the ambiguities in the particle identification cannot be solved and they get a double particle assignment. In table 13 the particle assigments are listed as function of the measured probabilities.

The result of the particle identification is that the unit direction vector $\hat{p}$ and the momentum p as obtained from the drift chamber tracks can be extended into a four vector $(E,\vec{p})$ for each particle hypothesis. The four vector $(E,\vec{p})$ will be used later on in the calculation of invariant masses for combinations of tracks.

5.8 Track Reconstruction in the Vertex Telescope

5.8.1 Global strategy

The four vectors obtained from the reconstruction in the downstream spectrometer do not have a sufficient spatial resolution to allow for the reconstruction of decay vertices in the first few centimeters behind the target. To improve on this, the information from the vertex telescope is used. With the coordinates as found in the telescope (see section 5.2) and guided by the drift chamber tracks we do a track segment search, followed by a refit of the four vector resulting in a more precise measurement.

Table 13: Particle assignment.

particles below the threshold of all counters traversed			→ pion
$P(\pi) \geq 2xP(K)$	and	$P(\pi) \geq 2xP(p)$	→ pion
$P(K) \geq 2xP(\pi)$	and	$P(K) \geq 10xP(p)$	→ kaon
$P(K) \geq 2xP(\pi)$	and	$P(p) < 10xP(\pi)$	→ kaon
$P(p) \geq 2xP(\pi)$	and	$P(p) \geq 10xP(K)$	→ proton
$P(p) \geq 2xP(\pi)$	and	$P(K) < 2xP(\pi)$	→ proton
$P(K) \geq 2xP(\pi)$	and	$P(p) \geq 2xP(\pi)$	
	and		→ kaon or proton
$P(K) \geq 2xP(p)$	and	$P(K) < 10xP(p)$	
$P(p) \geq 2xP(\pi)$	and	$P(K) \geq 2xP(\pi)$	
	and		→ kaon or proton
$P(p) \geq 2xP(K)$	and	$P(p) < 10xP(K)$	
$P(\pi) \geq 2xP(K)$	and	$P(\pi) < 2xP(K)$	
	and		→ pion
$P(p) \geq 2xP(K)$	and	$P(p) < 2xP(\pi)$	

Track segment reconstruction is done in two steps :

- first the coordinates which belong to a track are selected from the assembly off all measured coordinates,
- subsequently the coordinates are fitted with a straight line. A χ^2 test is performed on the result of the fit as a last acceptance test on the track quality.

The environment for track reconstruction in the vertex telescope is very different from that in the drift chambers of the spectrometer. The number of planes available is rather small, two projections with three detectors plus one separate detector, providing little redundancy. The coordinate density in the detectors is very high, due to which a sizable number of coordinates originate from large composite clusters. When performing a straight unguided track search one will face the problem of finding ghost tracks or distorted tracks due to ambiguities in the coordinate choice. To circumvent this, the search in the vertex telescope is done with drift chamber guidance and in steps of decreasing track quality. The track slope resolution (in the Y-Z plane) from the drift chambers is, due to the long lever arm in the spectrometer, of the same order of magnitude as in the vertex telescope. Using this slope as a guide one overcomes to a large extent many of the problems mentioned above. To recover low quality tracks which were not found in the search which was guided by the drift chambers, a second track search is done using the combined guidance of the drift chamber tracks and the interaction vertex. The track search strategy in the vertex telescope is schematically illustrated in fig. 5.11.

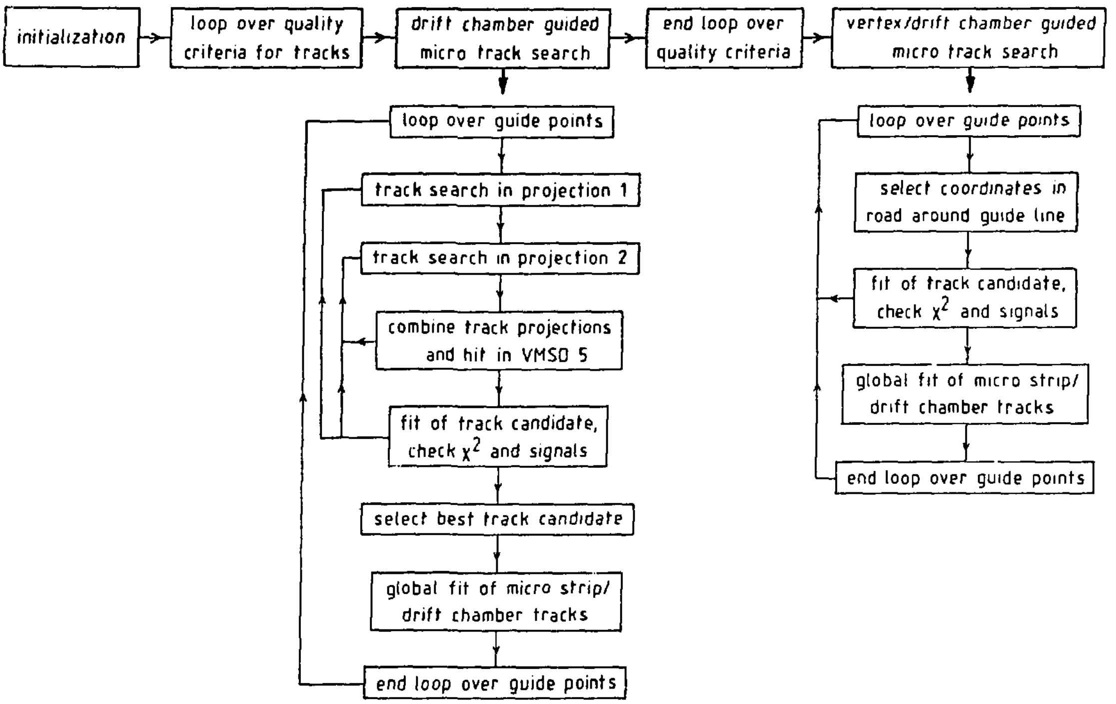

Fig. 5.11 Scheme of the track finding strategy in the vertex telescope.

5.8.2 Track search guided by the drift chamber tracks

The drift chamber guided search is performed as follows.

- First we reconstruct a guide point in the centre of the MNP magnet for each drift chamber track (see fig. 5.12). This guide point represents the crossing point of the tracks in ARM1 and 2 in the absence of a magnetic field.
- A loop is started over these constructed guide points.

- Subsequently a loop is done over the coordinates in planes three and four, the so-called master planes, at +14° and -14° with the horizontal, respectively (see fig. 2.2). In the two main views of the telescope coordinates are selected which lie in a road around the line connecting the coordinate in the master plane and that on the guide point. In a similar way a coordinate in the horizontal plane is also selected.
- It is checked that this track candidate crosses the surface of a cylinder. This cylinder is constructed around the beam axis, with a radius of 3 mm, starting 5 mm before the interaction vertex and ending at the first plane of the first VMSD. All decays should take place in this volume. By imposing this condition one prevents the reconstruction of unphysical ghost tracks.

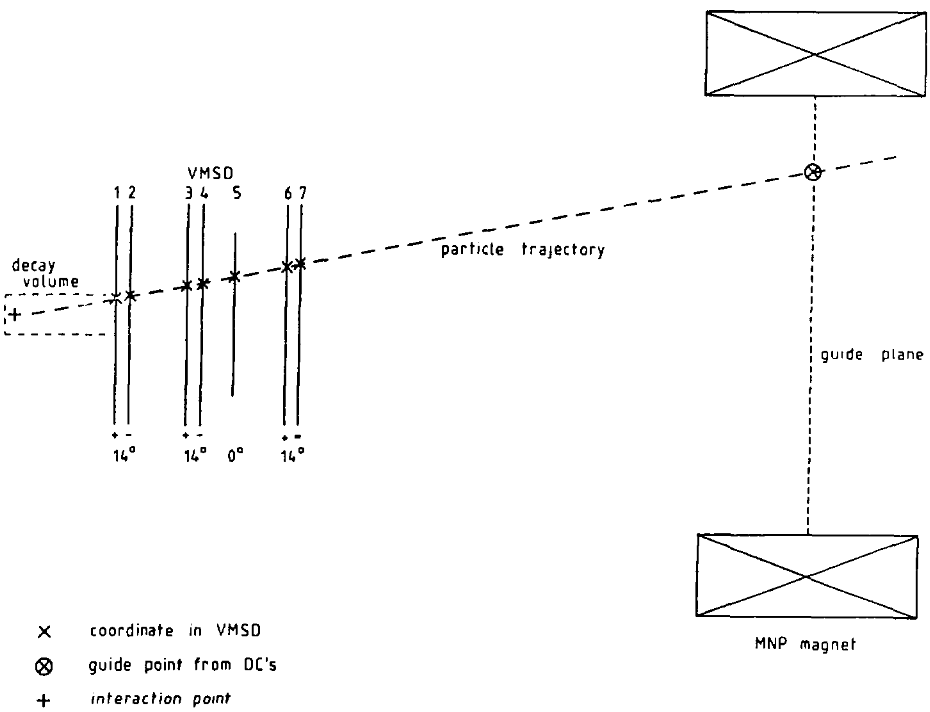

Fig. 5.12 Schematic representation of the drift chamber guidance.

- A track fit is now performed through the coordinates in the vertex telescope and the guide point giving a χ^2. This χ^2 is required to be less than 70. This limit was obtained in an empirical way in order to lose no tracks due to cluster decoding distortions.

- The resulting track candidate is required to pass in each detector between two strips which share a signal bigger than 0.2 m.i.p. As the detectors are 99.99% efficient (BELA1), this requirement can be made and it is a protection against reconstruction errors.
- For the guide point all track candidates are collected. The track candidate with the smallest errors is associated with this guide point.
- The momentum of the track is now refitted using a global fit in the spectrometer through all track segments (see section 5.6).

This drift chamber guided search is performed demanding seven coordinates in the telescope. The search is repeated for the unused guide points on unused coordinates demanding successively six, five and four coordinates in the telescope. In the case that a track did not produce a signal in a particular detector it is only accepted if it passes outside the active area of that detector.

5.8.3 Track search guided by drift chamber tracks and interaction vertex

In this search the guidance is provided by both the drift chambers and the position of the interaction vertex. For each unused guide point in the mid plane of the MNP magnet, a line is constructed which connects the interaction vertex with the guide point. Coordinates are selected which lie in a tube around this line. At least three coordinates distributed over all seven microstrip detectors in at least two different projections (±14°) are required for such a track. The track candidates are further subjected to the same requirements as in the drift chamber guided search.

5.8.4 Track quality

The correction of the track errors for multiple scattering is done by increasing the errors on the tracks with the multiple scattering errors. The contribution to the track error, at the position of the primary vertex can be parametrized by :

$$\sigma_{ms} = \frac{90.}{p}\ \mu m \qquad (5.8),$$

where p is the momentum of the track.

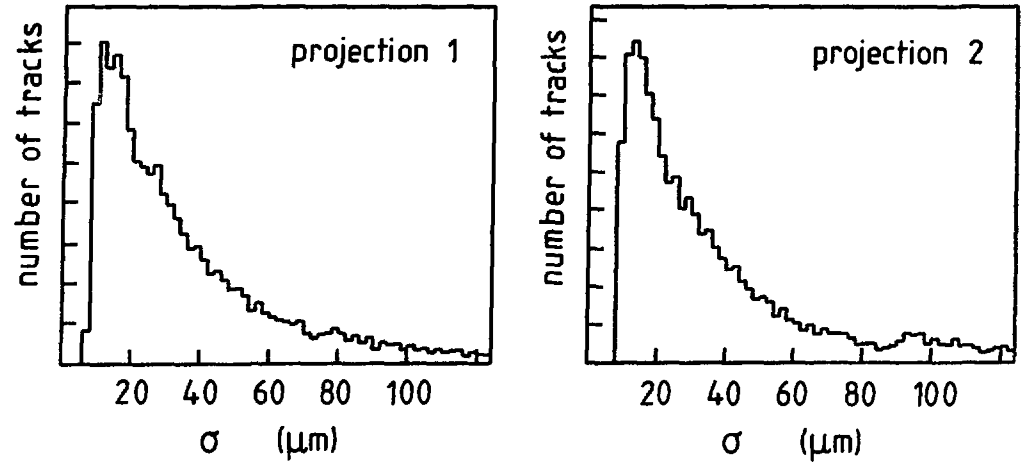

Fig. 5.13 The distribution of the resolutions of the VMSD tracks in both projections of the vertex telescope.

Figure 5.13 shows the track resolution calculated at the Z position of the interaction vertex in both projections of the telescope. For a sample of unselected interaction trigger events one can expect very few tracks to originate from decaying particles which decay before the vertex telescope. The reconstructed tracks should, within errors, point back to the primary vertex. A measure for this is the so-called χ^2 distance distribution. The χ^2 distance is the square of the distance of a track to the primary vertex divided by the square of the combined errors of the track and vertex. This distribution should behave as a χ^2 distribution of two degrees of freedom. In fig. 5.14 this distribution is shown for all tracks reconstructed in the vertex telescope which have a momentum larger than 2 GeV. An ideal χ^2 distribution should have an average value per degree of freedom: $\langle\chi^2\rangle/NDF = 1$. In fig. 5.14 this quantity is 1.6 which is a reasonable number in view of all approximations made. Figure 5.15 shows an example of a reconstructed event.

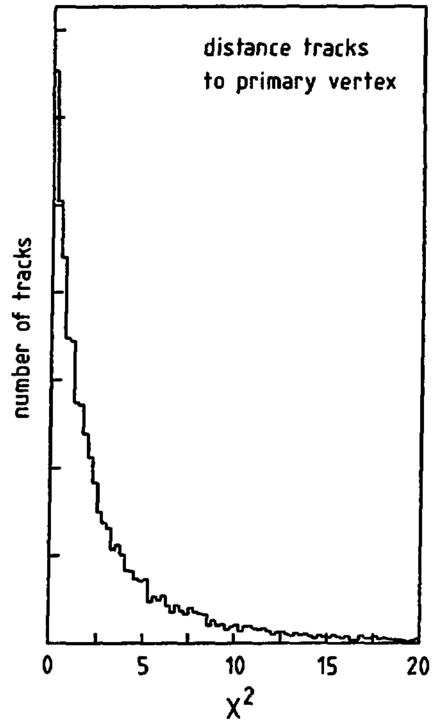

Fig. 5.14 The distribution of the χ^2 distances of all tracks found in the vertex telescope with a momentum larger than 2 GeV.

5.9 Secondary Vertex Reconstruction and Event Selection

The tracks reconstructed in the vertex telescope are used to reconstruct vertices originating from charmed particles decaying between the interaction vertex and the first VMSD. The channels in which we look for decay vertices are :

$$\begin{aligned} D^o &\rightarrow K^- + \pi^+ \\ D^+ &\rightarrow K^- + \pi^+ + \pi^+ \\ D^o &\rightarrow K^- + \pi^+ + \pi \\ D_s^+ &\rightarrow K^- + K^+ + \pi^- \\ D^+ &\rightarrow K^- + K^+ + \pi^- \quad \text{and c.c.} \end{aligned} \qquad (5.9).$$

In these channels charmed particles cannot be seen as a peak on the inclusive invariant mass spectrum of all track combinations without any secondary vertex requirements. This is due to two reasons: the presence of a large combinatorial background and a small number of detectable charm decays. The background is caused by the track combinations which might give an invariant mass in the charm mass region. The average charged track

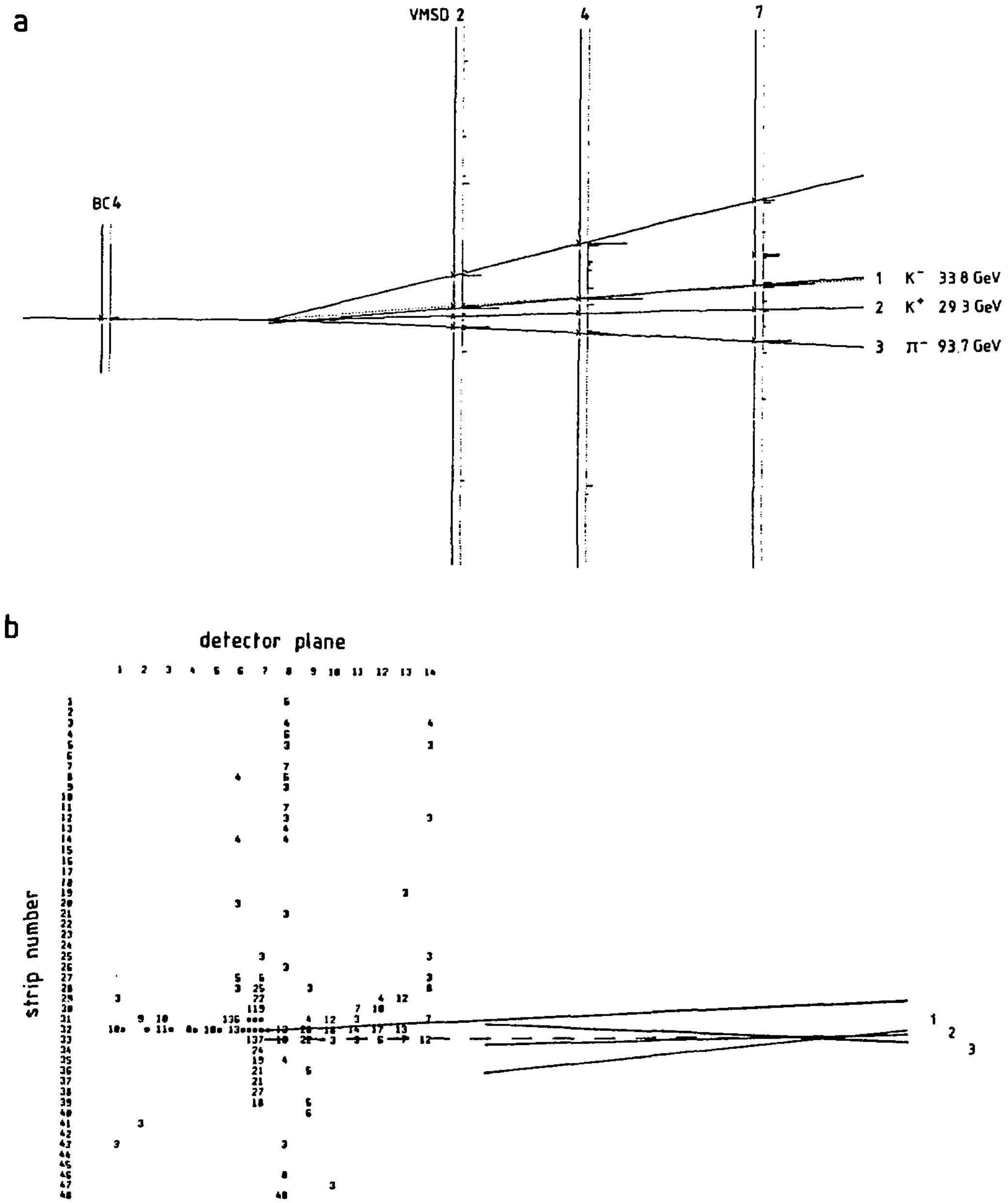

Fig. 5.15 Example of a reconstructed event. The event contains a decay $D_s^- \rightarrow K^+K^-\pi^-$ at ΔZ = 11.2 mm. The calculated mass is $M_{KK\pi}$ = 1.977 GeV. The lifetime is τ = $4.7 \cdot 10^{-13}$s. The two kaons are compatible with a ϕ meson as M_{KK} = 1.016 GeV.

a) Projection 2 of the vertex telescope. Indicated are the tracks, the pulseheights in the detectors and the attributed coordinates.

b) The active target. The broken line represents the calculated trajectory of the decaying D_s^- meson.

multiplicity in an event is eight, causing a large number of combinations. The charm particle cross section is very small (~ 1 °/oo of the total inelastic cross section). Combined with the branching ratio into one of the above decay channels (~ 10%) and the detection efficiency (~5%) this results in one detectable decay every $2 \cdot 10^5$ events, which is not visible above the existing background (see also ref. BAIL6). In fig. 5.16 an example is shown of the invariant mass distributions of all combinations from a subset of the total data sample. To reduce the large background, mass combinations with a detected secondary vertex are selected.

The secondary vertex reconstruction is restricted to those track combinations in the channels indicated above which are in a window around the charm mass region. For the decay channel $D^0 \rightarrow K\pi$ we have an additional requirement on the angle between the flight path of the D^0 and the K meson: $|\cos\Theta_K| < 0.8$. The mass intervals used are :

$$1.75 \leq M_{Kn\pi^-} \leq 2.00 \qquad n=1,3$$
$$1.75 \leq M_{KK\pi^-} \leq 2.15 \qquad (5.10).$$

After a combination in this interval has been found, a vertex fit is done with the tracks involved. The fit is a least squares fit, minimizing the weighted distances of the tracks to the vertex. The position of the vertex is subsequently used to recuperate as yet undiscovered tracks which might originate from this vertex. A guided track search is

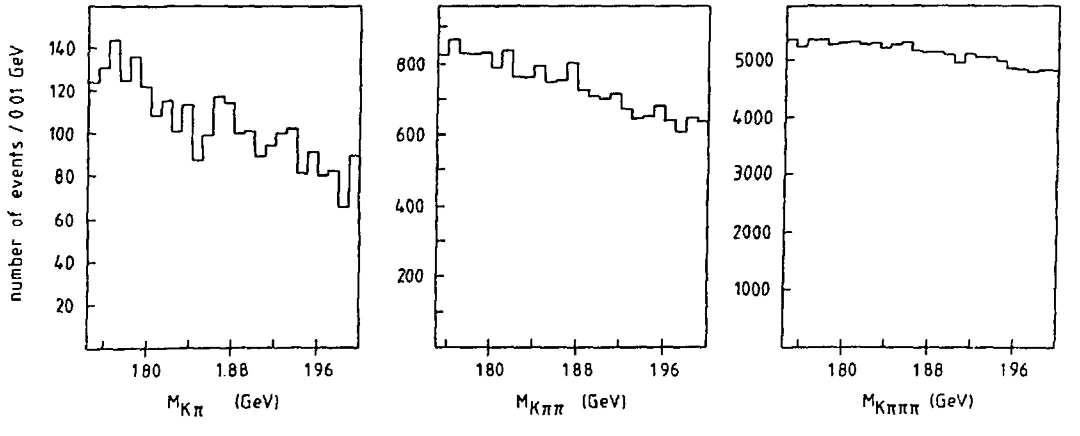

Fig. 5.16 Inclusive invariant mass distributions for all mass combinations without detection of a secondary vertex.

made in projection (+14° and -14°) only, using the vertex position and the unused coordinates in the vertex telescope. If a track is found in one or both projections the secondary vertex is considered to be incomplete, faking a decay vertex of one of the channels (5.9), and rejected.

5.9.1 The selection criteria for secondary vertices

5.9.1.1 Selection criteria on the tracks

The reconstructed secondary vertices are subjected to a set of selection criteria. These selections are meant to reject all mass combinations not originating from a charm decay vertex in that particular channel. In fact when all tracks are fitted with coordinates which exhibit pure Gaussian errors, and when those tracks are used for a vertex fit, two cuts should be enough to reject the combinations not originating from a secondary vertex. These cuts are: a cut on the χ^2 of the fitted secondary vertex and a cut on the relative distance, in terms of standard deviations, of the secondary vertex to the primary vertex. The former cut tests whether the tracks form a vertex, while the latter cut tests whether this vertex coincides with the primary vertex. In reality, however, the errors on the coordinates are not Gaussian, although they are represented and treated as such. Due to multiple scattering, elastic scattering of the tracks in the microstrip detectors and cluster encoding distortions, the error distributions of the coordinates have a Gaussian shape extended with a tail. These tails are not very large with respect to the Gaussian part, but they can introduce sizable effects in the vertex position and errors. To overcome these problems more cuts are introduced which would, in the case of pure Gaussian errors, be equivalent with the two basic cuts. Now however these cuts will filter out distorted tracks and clean up our sample. These cuts are: cuts on the resolutions of decay tracks, cuts on the χ^2 distance of the decay tracks to the primary vertex and a cut on the distance of secondary vertex to the primary vertex. A second class of cuts is still needed. Not all secondary vertices originate from charm decays in the channels mentioned in (5.9). These channels only represent ~15% of all decays. We will find additional secondary vertices originating from:

- charm decays from which a low momentum track misses the acceptance of the drift chambers,
- charm decays with unobserved neutral decay products,
- secondary interactions,
- vertices with wrongly assigned tracks.

To reject these combinations, cuts are applied to test whether the momentum sum vector of the decay points back to the primary vertex. In the case of secondary interactions other tracks may be attributed to the secondary vertex. A summary of the applied cuts is given below.

- A cut on the χ^2 of the secondary vertex. The χ^2 cut is set to correspond to a confidence level of 1%, 1% and 10% for respectively 2, 3 and 4 prong decays.
- A cut on the weighted distance of the secondary vertex to the primary vertex. The distance is required to be bigger than 4 σ.
- A cut on the distance of the secondary vertex to the primary vertex. The distance should be larger than 3 mm.
- Cuts on the $\chi^2_{distance}$ of the decay tracks to the primary vertex.
  For 2 prong decay: one track with $\chi^2_{distance} > 9$, the other with $\chi^2_{distance} > 4$.
  For 3 prong decay: two tracks with $\chi^2_{distance} > 9$, the other with $\chi^2_{distance} > 4$.
  For the $KK\pi$ decay channels, the last requirement was decreased to $\chi^2_{distance} > 1$, as the additional selected kaon provides the necessary background reduction.
  For 4 prong decay: two tracks with $\chi^2_{distance} > 9$, one other with $\chi^2_{distance} > 4$.
- A cut on the resolution of the decay tracks. The decay is required to have at least two track projections (in the vertex telescope) with a resolution better than 40 μm.
- A cut to test whether the momentum sum vector of the decay points back to the primary vertex. The $\chi^2_{distance}$ of the trajectory of the reconstructed charm decay candidate with respect to the primary vertex should be less than 12.
- Cuts on the attribution of leftover tracks to the various vertices. Two types of leftover tracks can be present, tracks found with drift chamber guidance and tracks only seen in the vertex telescope. A track can be attributed to a vertex when it has a weighted impact parameter of less than 3 σ and in both projections a resolution better than 30 μm.
  Of the tracks which cannot be attributed to the primary vertex only one is allowed to point to the secondary vertex.

Only one extra track reconstructed in a vertex telescope projection without drift chamber guidance is allowed to point to the secondary vertex while being incompatible with the primary vertex.

Tracks which point back to neither of the two vertices are used in a search for a third vertex.

Only one track is allowed to point back to none of the three vertices.

5.9.1.2 Selection criteria using tracks and active target

The aim of an active target consistency cut is to check whether tracks, which are considered as decay tracks, can be recognized as coming from the primary vertex from the pulse height in the active target. As a first step all tracks in the event which have a $\chi^2_{distance}$ of less than 9 are classified as pointing to the primary vertex. These "pointing" tracks are then displaced parallel to themselves towards the primary vertex. Subsequently the pulse heights in all planes of the active target downstream of the interaction vertex are calculated. For the calculated pulse heights it is assumed that a particle deposits a charge equivalent to 1 m.i.p. in each plane divided over the two nearest strips. The calculated pulse height for each strip is then summed for all "pointing" tracks. The calculated and measured pulse heights in the pairs of strips covered by the decay tracks which were classified as "pointing" are then compared with each other. The Landau distribution has, as function of the pulse height, a steep rise to a maximum followed by a slower descent into a long tail (see figs. 3.2 and 4.4). If a pulse height is measured which is bigger than the one calculated, no statement can be made as to whether these are compatible with each other, due to the tail from the Landau distribution. However, if the measured pulse height is smaller than the one calculated, and lower than the pulse height at the onset of the distribution, the measured pulse height can be considered to be incompatible with the calculated. In that case one may conclude that fewer particles have passed than presumed from the "pointing" classification. The compatibility is checked by taking the difference between the measured and the calculated pulse heights. For the planes in which the measured pulse height (ph) is smaller than the calculated, these differences are added in quadrature and divided by the number of planes behind the interaction plane (5.11). To consider a track not present, i.e. incompatible with the active target, this value should exceed 0.2, which corresponds to a level of 0.45 m.i.p.; we use :

$$\frac{\Sigma_{planes}(ph_{measured} - ph_{calculated})^2}{N_{planes}} > 0.2 \qquad (5.11).$$

For 3 and 4 prong decays it is allowed that at most 1 track is compatible with the primary vertex according to the target information. For 2 prongs this test is not made, as it does not change the signal over background ratio.

Using the reconstruction and selection as described in this chapter events are selected. These events, their mass spectra and the extracted lifetime results are presented in the next chapter.

6. MASS SPECTRA AND LIFETIMES OF CHARMED MESONS

6.1 Introduction

In this chapter we will present the selected events as obtained with the selection criteria described in chapter 5. The chapter is organized as follows: first we will discuss the method to extract the lifetime from a sample taken with a restricted efficiency as function of the lifetime, then we will discuss the treatment of the background. In the following sections we will present the selected data sample and the lifetimes obtained. Systematic biases will also be discussed.

6.2 Lifetime Determination Via Measurement of Decay Length

In this section we will give a description of the method employed to determine the mean lifetime of a particle via the measurement of the decay length.

The probability of a particle to decay per unit time is taken to be λ. In total we have N particles from which dN decay in a time interval dt :

$$dN = -N\lambda dt \quad , \quad \text{and hence} \quad N = N_o e^{-\lambda t} \qquad (6.1),$$

with: N_o the initial number of particles at $t = 0$.

We can now define $\tau = 1/\lambda$ which is the mean lifetime of the particle. The probability to observe a particle which decays with a lifetime between t_i and t_i+dt_i is then :

$$P(t_i) = \frac{k_i e^{-t_i/\tau} dt_i}{\int_o^\infty e^{-t_i/\tau} dt} = \frac{k_i}{\tau} e^{-t_i/\tau} dt_i \qquad (6.2),$$

with: k_i the probability to observe a decay independent of lifetime.

When the particle is only observable in a certain time interval $[t_{min}, t_{max}]$, then the normalization factor in the denominator of (6.2) becomes an integral between t_{min} and t_{max} :

$$P(t_i) = \frac{k_i}{\tau} \frac{e^{-t_i/\tau} dt_i}{e^{-t_i^{min}/\tau} - e^{-t_i^{max}/\tau}} \qquad (6.3),$$

In the case that $t_i^{max} \gg \tau$, i.e. the length of the decay volume is long with respect to the mean decay length, (6.3) becomes :

$$P(t_i) = \frac{k_i}{\tau} e^{-(t_i - t_i^{min})/\tau} \quad dt_i \qquad (6.4).$$

This is again an exponential decay distribution but now in the so-called "corrected" lifetime $t_i - t_i^{min}$.

When a sample of N particles is detected, then their mean lifetime τ can be extracted using the likelihood function L :

$$L(\tau) = \prod_{i=1}^{N} \frac{k_i}{\tau} \frac{e^{-t_i/\tau}}{e^{-t_i^{min}/\tau} - e^{-t_i^{max}/\tau}} \qquad (6.5).$$

The lifetime is obtained by maximizing the logarithm of L with respect to τ.

In reality the individual lifetimes of the particles are obtained from three quantities: the traversed distance l_i from production to decay vertex, the momentum p_i and the mass of the particle m_i :

$$t_i = \frac{m_i c^2}{p_i c} \bullet \frac{l_i}{c} \qquad (6.6).$$

In the following subsections we will elaborate on the method to extract the lifetime from the observed events. In particular the effect of the background on the lifetime and the detection efficiency as function of the decay distance will be discussed.

6.2.1 Detection efficiency

The detection efficiency for an event with certain kinematical properties can be approximated with a block shaped efficiency function. Below a time t_i^{min} the efficiency is zero, between t_i^{min} and t_i^{max} the efficiency has a constant value, above t_i^{max} the efficiency is again zero. Interpreting the time interval $[t_i^{min}, t_i^{max}]$ as a time interval in which the decay is visible, the values of t_i^{min} and t_i^{max} can formally be regarded to have no errors. The measurement errors will however vary for decays of each decay channel, as the environment depends on additional tracks which influences the attribution of errors to the coordinates in the vertex telescope. These differences occur due to e.g. Landau fluctuations, elastic scattering in the silicon detectors and the influence of the charge deposited due to the other tracks in the event. The efficiency function will thus have slanted front and rear edges. We will however neglect this effect and assume that the efficiency function has infinitely steep front and rear edges. This approximation is made, as the effect of the errors will be rather small with regard to the sensitive time interval. One can expect the effect to average out.

The edges of the efficiency curve are determined for each individual event. The low edge t_i^{min} is found by shifting the decay back, in small steps along the flight path of the decaying particle, towards the primary vertex (the so-called "swimming back procedure"). All other track parameters, like direction and errors, are kept constant. The event is then rerun through all selection criteria of the analysis program for each step. The first step at which the event is rejected, determines t_i^{min}. The maximum time t_i^{max} is determined by the length of the decay volume and hence the position of the first detector in the vertex telescope. The validity of the approximation made for the efficiency function can be tested by studying the dependence of the result for the mean lifetime as function of the applied cuts. This procedure is described in section 6.3.2.2.

6.2.2 Fit of mass spectra

The decaying particles which are selected by the analysis program are not all signal (= real D meson) events. In the invariant mass histogram one can see that a D signal is present above a background (see section 6.3). These background events are due to e.g. interactions of secondaries, misidentified decays of other particles or other decay modes, and reconstruction problems which fake a D decay in that particular decay channel. To extract the lifetime of the signal events one has to correct for the background events which are present under the signal. The probability to find an event with mass $m_i \pm \sigma_i$ is given by :

$$P(m_i) = \frac{1}{N} \left(a + bm_i + \frac{c}{\sqrt{(2\pi)}\sigma_i} e^{-(m_i - m_D)^2/2\sigma_i^2}\right) \qquad (6.7),$$

in which the background is taken to be linear in m. As the width of the D signal is negligible with respect to the error on the mass measurement, it is represented by a Gaussian distribution. Here, N is the total number of events in the mass interval $[m_1, m_2]$ which is considered for the lifetime measurement. The normalization requirement then becomes :

$$\int_{m_1}^{m_2} P(m)\, dm = 1 \qquad (6.8).$$

The parameters m_D, a, b and c can be extracted for a given set of events by maximizing the logarithm of the likelihood function L with respect to m_D, a, b and c :

$$\ln L = \sum_i \ln P(m_i) \qquad (6.9),$$

yielding a maximum value $\ln L_{opt}$ for the optimum positions of m_D, a, b and c. The quantity lnL forms, in the multidimensional space of all parameters, a surface with a maximum at the optimum values of all parameters. The errors on the parameters are determined by calculation of the value of these parameters at the positions (below and above the optimum parameter values) on the likelihood function, where $\ln L = \ln L_{opt} - 0.5$, varying one parameter at a time, and keeping the others fixed. Their variations are then taken as errors (EADY1).

The probability to observe a decay with lifetime t_i and mass m_i is then given by :

$$P(t_i, m_i) = \frac{P_D(m_i)}{\tau_D} e^{-t_i/\tau_D} + \frac{P_B(m_i)}{\tau_B} e^{-t_i/\tau_B} \qquad (6.10),$$

with:

$$P_D(m_i) = \frac{c}{N\sqrt{(2\pi)}\sigma_i} e^{-(m_i - m_D)^2/2\sigma_i^2} \qquad (6.11),$$

and:

$$P_B(m_i) = \frac{1}{N}(a + bm_i) \qquad (6.12).$$

Expressions 6.11 and 6.12 give the probability that a decay belongs to the signal or the background, respectively. We can now rewrite the likelihood function :

$$L = \prod_{i=1}^{N} \left(\frac{P_D(m_i)}{\tau_D} \frac{e^{-t_i/\tau_D}}{e^{-t_{i,min}/\tau_D} - e^{-t_{i,max}/\tau_D}} + \frac{P_B(m_i)}{\tau_B} \frac{e^{-t_i/\tau_B}}{e^{-t_{i,min}/\tau_B} - e^{-t_{i,max}/\tau_B}} \right) \qquad (6.13).$$

When the parameters obtained by maximizing (6.9) are used as input, the maximization of L in (6.13) with respect to τ_D and τ_B will yield their optimum values.

6.2.3 The influence of the measurement errors of the lifetime of individual events on the mean lifetime

The lifetime of each individual decay is measured with a finite measurement error. To check the effect of an error on the individual lifetime, we used a Monte Carlo program in which a lifetime distribution was generated. Subsequently the distribution was smeared, by shifting each individual value with an error value as drawn from a Gaussian error distribution. A fit to the smeared curve was performed to obtain again a lifetime. For various assumptions on the error distributions, the difference with the original generated lifetime was smaller than 2%. In the fit we can thus omit the error on the individual lifetime, as our statistical error exceeds this value.

6.3 Results

6.3.1 Mass spectra from the selected events

The invariant mass distributions for the selected events are presented in figures 6.1 and 6.2. In fig. 6.1 the mass distributions for the decay channels $D^o \to K\pi$, $D^+ \to K\pi\pi$ and $D^o \to K\pi\pi\pi$ are given for the two different beam types K^- and π^- as well as for the total data set. In all distributions the signals for the D mesons stand out clearly above the background. In fig. 6.2 the mass distributions are shown for the decay channels $D^+ \to KK\pi$ and $D_s^+ \to KK\pi$. The mass distribution for the K^- data shows an accumulation of events around the D_s^+ mass. From the 10 events seen in the D_s^+ mass region, 3 have a KK mass compatible with a ϕ meson. Only one event is due to a D_s^+, the rest originate from D_s^-. The signal due to $D^+ \to KK\pi$ is either very small or absent. In the distribution for the π^- beam no evidence is seen for either decay mode. This seems to indicate that D_s^- production is favoured with the K^- beam, in which case the strange valence quark of the D_s^- originates from the K^- (leading particle effect). However, no enhancement of D^+ production with a K^- beam is expected, which is confirmed by the absence of a $D^+ \to K^+K^-\pi^+$ signal as seen in the π^- beam.

For all channels the number of signal and background events, as fitted with an algorithm described in section 6.2.2, are presented in table 14.

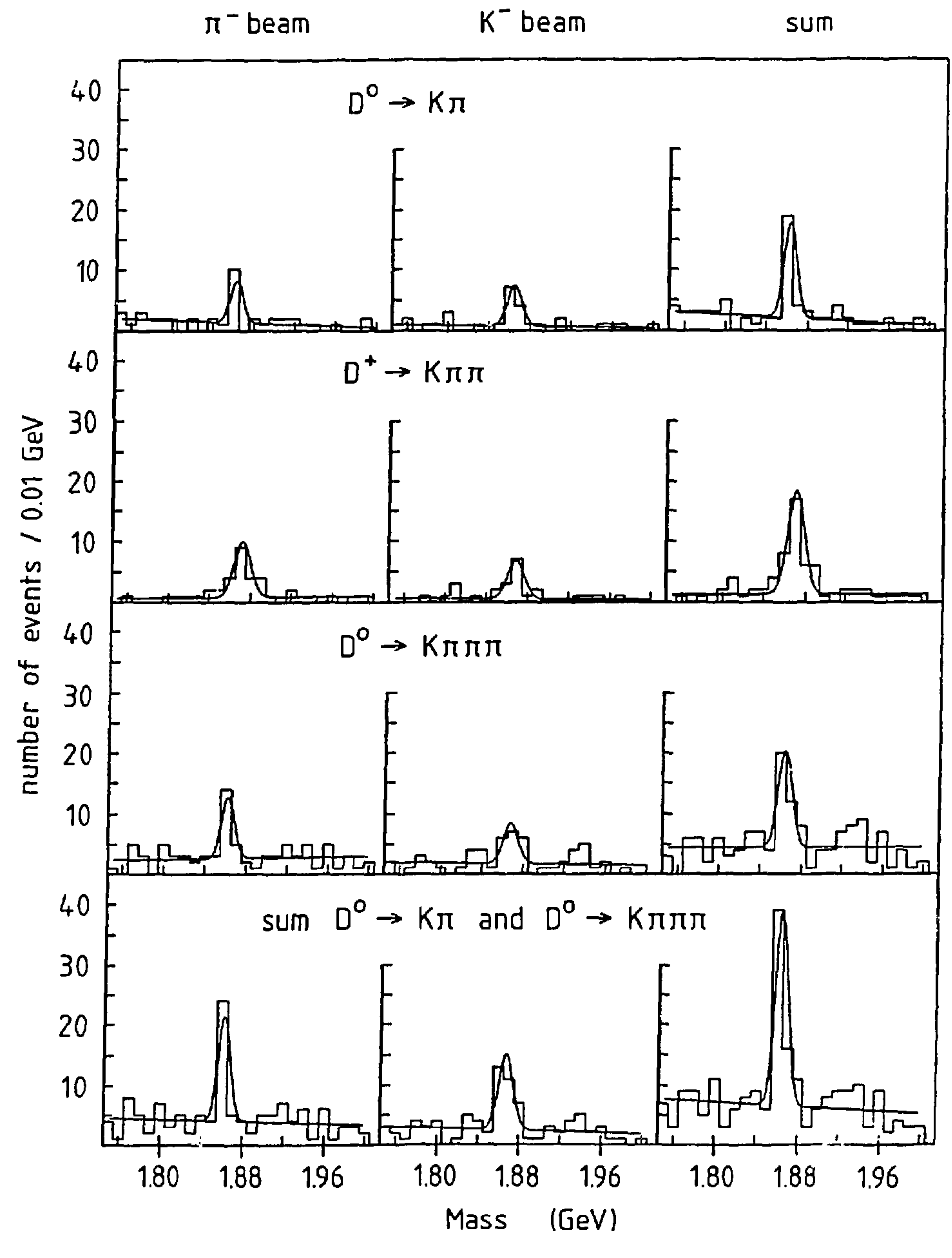

Fig. 6.1 The invariant mass distributions for the selected events in the channels $D^0 \to K\pi$, $D^+ \to K\pi\pi$ and $D^0 \to K\pi\pi\pi$, for incoming π^- and K^-, and for their sum. The lines are the results from the fits in the mass window 1.75 to 2.00 GeV.

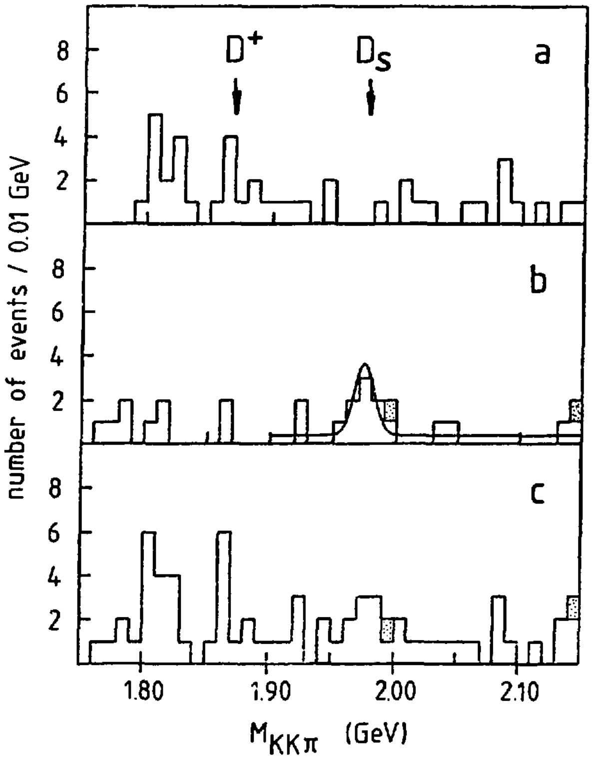

Fig. 6.2 The invariant mass distributions for the selected events in the channels $D_s^\pm \to KK\pi$ and $D^+ \to KK\pi$, the dotted events are ambiguous with the decay $D^+ \to K\pi\pi$, a) incoming π^- beam, b) incoming K^- beam and c) all data. The line in b) is the result from the fit in the mass window 1.9 to 2.15 GeV, above the D^+ mass.

Table 14: Number of fitted signal and background events

decay channel	mass (GeV)	number of signal events	number of background events
$D^o \to K\pi$	1.863±0.002	24±5	5
$D^+ \to K\pi\pi$	1.871±0.002	34±5	4
$D^o \to K\pi\pi\pi$	1.864±0.001	26±6	12
$D^o \to K\pi + D^o \to K\pi\pi\pi$	1.864±0.001	48±8	16
$D_s^+ \to KK\pi$ *	1.978±0.005	8	2

* not fitted, see section 6.3.3.

6.3.2 The lifetimes of the D^0 and D^+ mesons

6.3.2.1 Lifetime determination

For the events in the mass distributions displayed in fig. 6.1 we perform the lifetime fit as described in the previous section. The lifetimes for the D^+ meson from the $K\pi\pi$ channel, for the D^0 meson from the $K\pi$ and $K\pi\pi\pi$ channel as well as for the sum of the last two are given in table 15. The lifetime of the background is also given. The lifetime of the background is significantly smaller than the lifetime of the signal, indicating that the background may be due to reconstruction accidents resulting in short distance vertices and due to secondary interactions in the active target, which occupies the first few mm of the decay volume. In fig. 6.3 the corrected lifetime distributions are shown for the events in the signal regions. The curves represent the fitted lifetimes which also contain a component for the background.

Table 15: Results of the lifetime fits for D^0 and D^+.

decay channel	τ_{signal} $(10^{-13}s)$	$\tau_{background}$ $(10^{-13}s)$
$D^0 \to K\pi$	$4.4\pm^{1.1}_{0.9}$	$1.7\pm^{0.4}_{0.3}$
$D^+ \to K\pi\pi$	$9.5\pm^{2.1}_{1.6}$	$0.9\pm^{0.3}_{0.2}$
$D^0 \to K\pi\pi\pi$	$3.4\pm^{0.8}_{0.6}$	$1.8\pm^{0.2}_{0.2}$
$D^0 \to K\pi$ or $K\pi\pi\pi$	$3.8\pm^{0.7}_{0.5}$	$1.8\pm^{0.2}_{0.2}$

6.3.2.2 Systematic errors

When measuring the lifetime of a particle via the measurement of the flight path of individual events we take into account the detection efficiency as function of the length of the flight path by defining the minimum and maximum detectable lifetimes (see section 6.2.1). To check the validity of our procedure we vary several cuts which are sensitive to the decay distance (Δz, $\chi^2_{distance}$) and determine the lifetime again. When the assumption on the shape of the efficiency curve was correct and the swimming back procedure was correctly executed we should arrive at the same lifetime, within errors, for each set of cuts. Some caution is necessary in interpreting the results, as the events samples are not statistically independent.

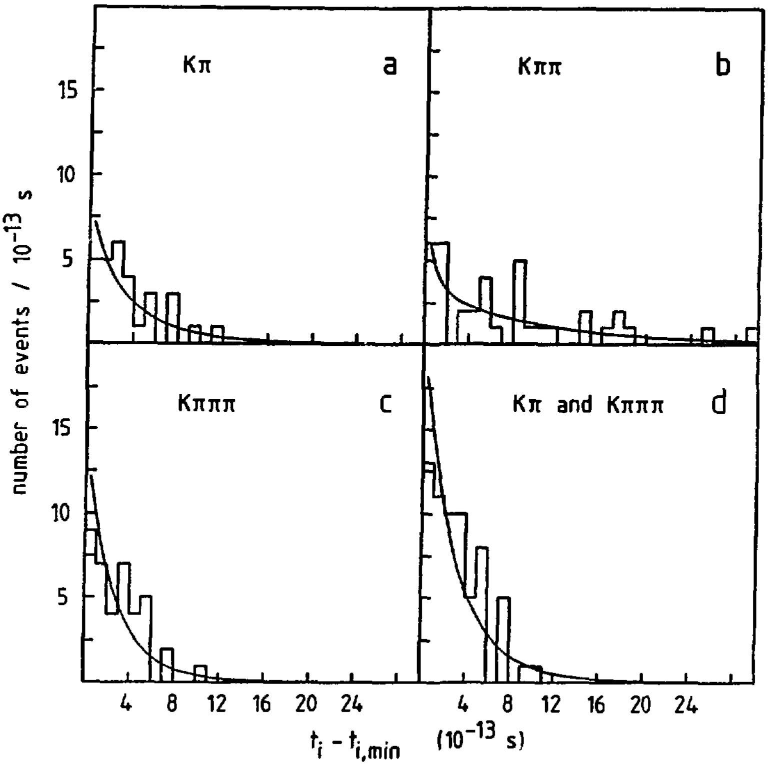

Fig. 6.3 Corrected lifetime distributions: The curve drawn is the background-corrected, fitted lifetime distribution. a) Kπ, b) Kππ, c) Kπππ and d) Kπ + Kπππ.

We have calculated the lifetime of the D^o and D^+ with several sets of cuts. The cuts used for the study of systematic errors are summarized in table 16. The calculated lifetimes obtained with the various sets of cuts are shown in fig. 6.4. From the measured lifetimes with the different cuts we conclude that the effects of systematic errors are smaller than $0.4 \cdot 10^{-13}$s. An independent check on systematic effects of selection criteria on the lifetime can be performed with the measurement of the decay $K_s^o \to \pi^+\pi^-$. Due to the relatively long lifetime of the K_s^o, the decay distance distribution of observed K_s^o should be flat (average decay length >> length of decay volume). In fig. 6.5 the decay distance distribution is presented for K_s^o selected with the same selection criteria as for $D^o \to K\pi$. Within statistics this distribution appears flat. A possible slight enhancement between Δz = 3 and 6 mm may be due to secondary interactions in the active target. We may conclude that no systematic bias is observed with this method.

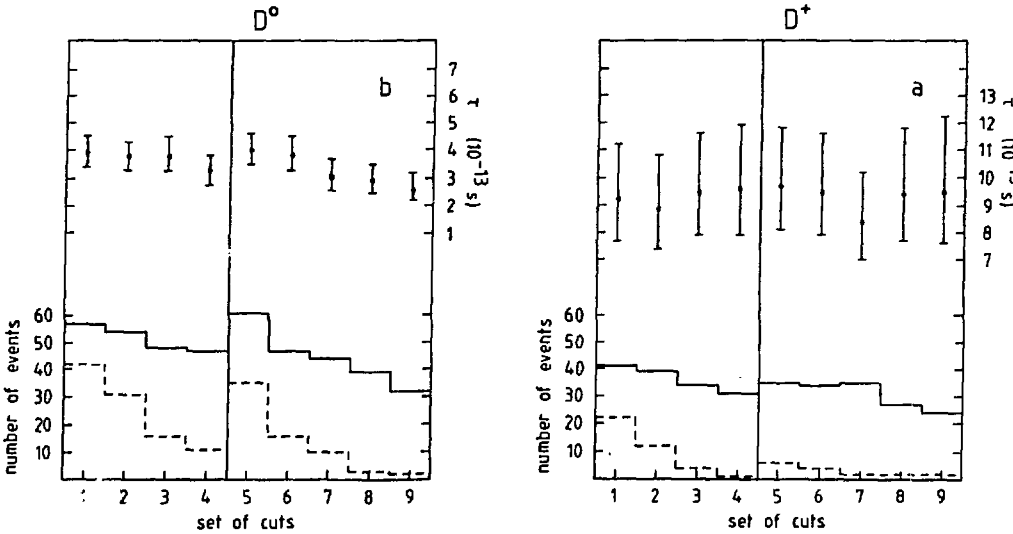

Fig. 6.4 The lifetimes as obtained with various sets of cuts. The cuts are listed in table 16. Sets 1 to 4 are for the first group in table 16, sets 5 to 9 for the second group. Set 3 and set 6 are identical. In each picture the top plots gives the lifetime results, the drawn histogram the signal and the broken line histogram the background below the signal. a) $K\pi$, b) $K\pi + K\pi\pi\pi$.

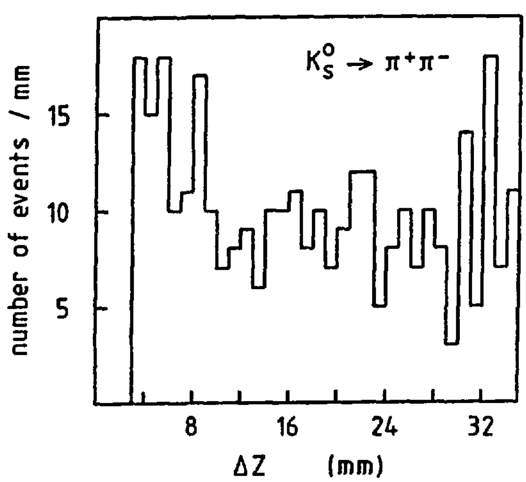

Fig. 6.5 Distribution of the decay distance of $K^0_S \to \pi^+\pi^-$.

Table 16: The cuts used for the systematics study.

The cuts which are not varied remained as described in section 5.9

cut set	Δz(mm)	σ	χ^2 distance for closest, 2nd closest and 3rd closest track to the primary vertex		
			$K\pi$	$K\pi\pi$	$K\pi\pi\pi$
1	3	4	0	0	0
			4	4	0
				9	4
2	3	4	0	0	0
			9	9	0
				9	9
3	3	4	4	4	0
			9	9	4
				9	9
4	3	4	9	9	0
			9	9	9
				9	9
5	2	4	4	4	0
			9	9	4
				9	9
6	3	4	4	4	0
			9	9	4
				9	9
7	4	4	4	4	0
			9	9	4
				9	9
8	5	4	4	4	0
			9	9	4
				9	9
9	6	4	4	4	0
			9	9	4
				9	9

6.3.3 The lifetime of the D_s^+ meson

For the determination of the D_s^+ lifetime we will use the data obtained with the K^- beam, as only in this subsample a clear signal is visible above the background. To avoid distortions due to decays which are ambiguous (in particle identification) with the decay $D^+ \rightarrow K\pi\pi$, we do not include events, if they have a $K\pi\pi$ mass in the range: $1.85 < M_{K\pi\pi} < 1.90$ GeV (see fig. 6.6a). As can be seen from fig. 6.2, the number of events available for the determination of the D_s^+ lifetime is very limited, due to which a fit of the lifetime will gain us little precision. Therefore we will only make an average of the individual lifetimes corrected for background. To study possible systematic effects of the background on the lifetime, we try to clean up the $KK\pi$ mass spectrum by scanning the events, because in a small sample background events can have a large impact. We will discuss three cases, one without any scanning criterion, and two cases with successively tighter scanning criteria.

1. For the event sample as shown in fig. 6.6a which is selected without scanning criteria, the lifetime of signal and background are presented in table 17, row 1. In fig. 6.7 the corrected lifetime distributions are shown for the events in the signal regions, the curve representing the average lifetime which contains a component for the background. The lifetime of the background is taken as the average from the events in the mass windows $1.90 < M < 1.95$ GeV, $2.00 < M < 2.15$ GeV

2. The event sample is cleaned up by a visual scan of individual events. The scan is performed on an Apollo work station with a visual display terminal. The purpose of the scan is to recognize either wrongly reconstructed primary vertices or secondary interactions in the target. Wrongly reconstructed primary vertices are recognized from the target information together with the tracks from the vertex telescope. They are mostly due to backscattered heavy fragments in the active target. Secondary interactions are found again by visually combining track and target information. If the target contains a large excess of charge in the neighbourhood of the secondary vertex and extra tracks seem to originate from the same region, one can classify the event as a secondary interaction. In fig. 6.6b the resulting mass spectrum is presented. The scan clearly rejects background events while the signal remains. In table 17, row 2, the lifetime results for this sample are given.

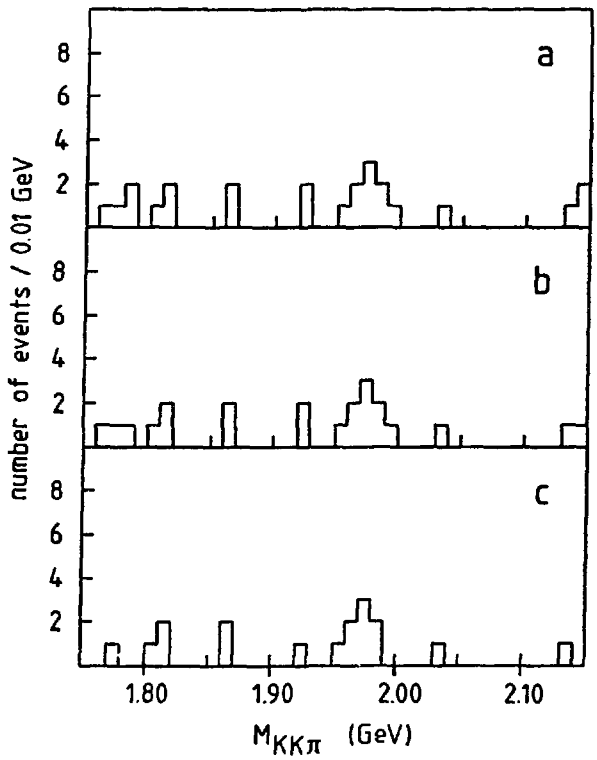

Fig. 6.6 The mass distributions for the K^-beam data in the $KK\pi$ channel, a) no scan, b) scan to reject secondary interactions and wrong primary vertices, c) scan as b) but to also reject wrong reconstruction.

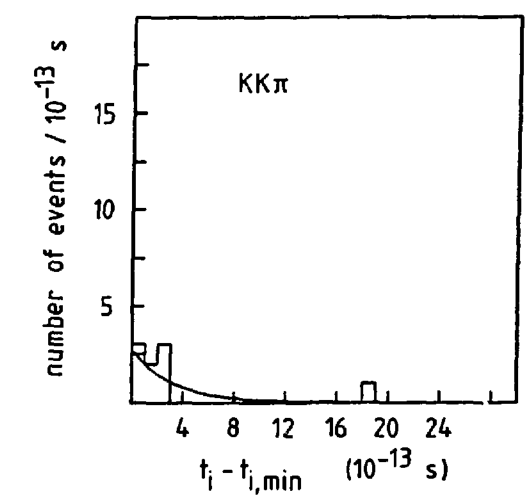

Fig. 6.7 Corrected lifetime distribution for $KK\pi$. The curve drawn is the background-corrected, average lifetime distribution for $KK\pi$ (case 1).

3. With the second set of scanning criteria we reject, in addition to the criteria in case 2, also reconstruction errors which are clearly contradicted by the active target information. Wrong reconstructions are vertices found with tracks originating from different vertices, but which are combined into a fictitious secondary vertex. Wrong reconstructions can be rejected if decay tracks are seen in the active target, but are evidently not originating from the reconstructed vertex. On the basis of this scan we arrive at the mass distribution as depicted in fig. 6.6c. The results for the lifetime are given in table 17, row 3.

From the study of the influence of the background on the lifetime, we conclude that no appreciable effect can be seen. We have checked that the result without scanning, and thus without bias, is stable within the errors.

Table 17: Lifetime results for the D_s^+ meson.

1) no scan, 2) scan to reject secondary interactions and wrong primary vertices, 3) scan as 2, but also reject wrong reconstruction.

case	mass (GeV)	number of signal events	number of background events	τ_{signal} (10^{-13}s)	$\tau_{background}$ (10^{-13}s)
1	1.974±0.005	8	1	$3.6\pm^{1.1}_{1.5}$	2.4±1.0
2	1.974±0.005	8	1	$3.6\pm^{1.1}_{1.5}$	2.2±1.0
3	1.971±0.004	7	1	$3.9\pm^{1.3}_{1.7}$	2.9±1.7

6.4 Comments on the Relative Production Rates of Charmed Particles

From the total number of events measured with incoming K^- beam and incoming π^- beam , we can extract the relative cross section for the production with the two beam types. These numbers can be stated under the assumption that the acceptance of the spectrometer is equal for both K^- and π^- production. The cross section ratios obtained are :

$$\frac{\sigma(K^-Si\rightarrow D^{o/+})}{\sigma(\pi^-Si\rightarrow D^{o/+})} = \frac{37\pm7}{47\pm8} \bullet \frac{N(\pi^-)}{N(K^-)} = 1.3 \pm 0.3$$

$$\frac{\sigma(K^-Si\rightarrow D^{o})}{\sigma(\pi^-Si\rightarrow D^{o})} = \frac{23\pm5}{25\pm6} \bullet \frac{N(\pi^-)}{N(K^-)} = 1.4 \pm 0.5$$

$$\frac{\sigma(K^-Si\rightarrow D^{+})}{\sigma(\pi^-Si\rightarrow D^{+})} = \frac{14\pm4}{20\pm5} \bullet \frac{N(\pi^-)}{N(K^-)} = 1.1 \pm 0.4$$

We may conclude that the production rates in the K^- beam are of the same order of magnitude as those in the π^- beam within the Feynman x_F range (about 0 to 0.9) covered by the spectrometer (see ref. NEUG1).

6.5 Conclusions

The results for the lifetimes of the D^+, D^o and D_s^+ mesons are :

$$\tau(D^+) = 9.5\pm^{2.1}_{1.6}\pm0.4\bullet10^{-13}s$$
$$\tau(D^o) = 3.8\pm^{0.7}_{0.5}\pm0.4\bullet10^{-13}s$$
$$\tau(D_s^+) = 3.6\pm^{1.1}_{1.5}\pm0.4\bullet10^{-13}s$$

The errors given are statistical and systematic, respectively. The results for the lifetimes of the three types of D mesons are all obtained with the same apparatus and practically equal selection. Hence, it can be expected that systematic biases cancel out in ratios of the lifetimes. The lifetime ratios obtained are :

$$\tau(D^+)/\tau(D^o) = 2.5\pm0.6$$

$$\tau(D^+)/\tau(D_s^+) = 2.6\pm1.1$$

$$\tau(D_s^+)/\tau(D^o) = 0.9\pm0.4$$

The errors for the ratios were obtained by averaging the asymmetric individual errors followed by a standard error propagation.
The production rates in the K^- beam are of the same order of magnitude as those in the π^- beam within in the x_F range covered.

7. REVIEW OF EXPERIMENTAL RESULTS

7.1 Measurements of D° and D^{+} Lifetimes

A brief review will be given on other results of D meson lifetime measurements. The discussion is split up into two parts, one for the D° and D^{+}, and one for the D_s^{+}. The following lifetime measurements for the D° and D^{+} have been published up to now (see also tables 18 and 19).

Table 18: Measurements of lifetimes of D° mesons.

The errors indicated are statistical and systematic respectively.

	experiment	production process	detection technique	coord. resol. µm	# events	lifetime 10^{-13}s
E531	(USHI1)	$\nu + N$	emulsion +spectr.	1	58	$4.3^{+0.7}_{-0.5}{}^{+0.1}_{-0.2}$
WA58	(ADAM1)	$\gamma + N$	emulsion +spectr.	1	44	$3.6^{+1.2}_{-0.8}\pm 0.7$
NA11	(BAIL3, BELA1)	$\pi^- + Be$	Siµstrip +spectr.	4.5	26	$3.7^{+1.0}_{-0.7}\pm 0.5$
NA16	(AGUI1)	$p + H_2$	bubble +spectr.	45	16	$4.1^{+1.3}_{-1.0}$
NA18	(BADE1)	$p + H_2$	bubble +spectr.	30	9	$4.1^{+2.6}_{-1.3}\pm 0.5$
NA27	(AGUI2)	$\pi + H_2$	bubble +spectr.	15-20	11	$3.5^{+1.4}_{-0.9}$
SHF	(ABE1)	$\gamma + H_2$	bubble +spectr.	40-55	50	$6.1\pm 0.9\pm 0.3$
MARKII	(GLAD1)	e^+e^-	driftch. +spectr.	100	74	$4.7^{+0.9}_{-0.8}\pm 0.5$
DELCO	(YAMA1)	e^+e^-	driftch. +spectr.		280	$4.6\pm 1.5^{+0.7}_{-0.6}$
NA32 this experiment		$\pi^- + Si$ $K^- + Si$	Siµstrip +act.target +spectr.	4.5	48	$3.8^{+0.7}_{-0.5}\pm 0.4$

Table 19: Measurements of lifetimes of D^+ mesons.

The errors indicated are statistical and systematic respectively.

	experiment	production process	detection technique	coord. resol. µm	# events	lifetime 10^{-13}s
E531	(USHI1)	$\nu + N$	emulsion +spectr.	1	28	$11.1^{+4.4}_{-2.9}$
WA58	(ADAM1)	$\gamma + N$	emulsion +spectr.	1	27	$5.0^{+1.5}_{-1.0} \pm 1.9$
NA1	(ALBI1)	$\gamma + N$	act.target +spectr.		98	$9.5^{+3.1}_{-1.9}$
NA11	(BAIL3, BELA1)	$\pi^- + Be$	Siµstrip +spectr.	4.5	28	$10.6^{+3.6}_{-2.4} \pm 1.6$
NA16	(AGUI1)	$p + H_2$	bubble +spectr.	45	15	$8.4^{+3.5}_{-2.2}$
NA18	(BADE1)	$p + H_2$	bubble +spectr.	30	7	$6.3^{+4.9}_{-2.3} \pm 1.5$
NA27	(AGUI2)	$\pi + H_2$	bubble +spectr.	15-20	23	$9.8^{+3.4}_{-2.2}$
SHF	(ABE1)	$\gamma + H_2$	bubble +spectr.	40-55	48	$8.6 \pm 1.3^{+0.7}_{-0.3}$
MARKII	(GLAD1)	e^+e^-	driftch. +spectr.	100	23	$8.9^{+3.9}_{-2.7} \pm 1.3$
NA32 this work		$\pi^- + Si$ $K^- + Si$	Siµstrip +act.target +spectr.	4.5	34	$9.5^{+2.1}_{-1.6} \pm 0.4$

1. E531 (USHI1): This experiment uses the wide band neutrino beam of Fermilab. The experimental apparatus consists of an emulsion stack followed by a magnetic spectrometer. The scanning of the emulsion is performed by tracing the spectrometer tracks back into the emulsion in order to find the tracks originating from primary and secondary vertices. This technique yields a higher efficiency for finding secondary vertices than the usual volume scan in which a search for tracks is made in a restricted volume. The reconstructed events are distributed over many different decay modes including decay modes with neutral secondaries which cannot be visually associated with the decay vertex.

2. WA58 (ADAM1): A stack of emulsion was placed in a photon beam in front of the Ω spectrometer at the CERN SPS. The photon energy range was 20-70 GeV. The scanning was performed using a volume scan procedure in a 6.9 mm thick emulsion. The events were found in many different decay modes including decay modes with neutral secondaries. The result on the D^+ lifetime from this experiment is two standard deviations lower than the world average.

3. NA16/NA27 (AGUI1,AGUI2): These experiments use different versions of the same basic apparatus, i.e. a high resolution H_2 bubble chamber (LEBC) in front of the EHS spectrometer. The EHS spectrometer is a magnetic spectrometer with detectors for particle identification. The beam is a 360 GeV π^- beam at the CERN SPS. Many different decay modes, some with neutral particles, contribute to the final event sample.

4. NA18 (BADE1): This experiment uses a high resolution bubble chamber (BIBC) filled with a heavy liquid (C_6F_6). For momentum analysis of the secondary tracks a streamer chamber is employed. No particle identification nor π^0 detection is available. The experiment uses a 340 GeV π^- beam at the CERN SPS. The D^0 signal is seen in two decay channels ($K\pi$ and $K3\pi$), the D^+ signal in one channel ($K\pi\pi$).

5. SHF (ABE1): The SLAC Hybrid Facility has produced lifetime measurements from two experiments using the same basic apparatus. The difference between the two experiments can be found in the improvements in the performance of the apparatus. The apparatus consists of the SLAC 1 m bubble chamber in front of a forward spectrometer. The beam is a photon beam of 20 GeV. The events are reconstructed in many different decay modes. To compensate for missing π^0's a special algorithm was used to obtain the momentum of the decaying charmed meson. The lifetime results of this experiment are remarkable, as their measured lifetime ratio of D^0 and D^+ is rather small, which is in particular due to one D^0 events with a lifetime of $55 \cdot 10^{-13}$s.

6. NA1 (ALBI1): This was the first experiment to employ Si detectors for a lifetime measurement of charmed particles. The beam is a 40-150 GeV photon beam at the CERN SPS. The experiment employs a magnetic spectrometer (FRAMM) and a search is made for coherent production of D mesons

on an active target. The active target consists of 40 Si detectors, 300 µm thick, which are read out layer by layer. Momentum analysis and particle identification are performed by the downstream spectrometer. The lifetime of the D^+ mesons, which are reconstructed with the spectrometer, is determined in the following way. At least the first two active target layers should have no signal, guaranteeing that the interaction takes place in the target. At the first occurrence of a step in signal height, indicating an interaction in a layer, this step should correspond at least to two minimum ionizing particles (m.i.p.) and persist over at least four layers. Subsequently, a second step, corresponding to 2, 4 or 6 m.i.p. extending over at least four layers, indicates the decay of a long lived particle. The distance corresponding to the number of layers in the first ionization step is a measure of the lifetime of the decaying particle. The decay channels selected are: $D^+ \rightarrow K + \pi + \pi + n\pi^o$. As no connection can be made between the tracks in the spectrometer and the charge in the active target, the decay distances used for the lifetime determination are contaminated with D^o decays, for which certain corrections are made.

7. NA11 (BAIL3,BELA1): The predecessor of the experiment reported on in this thesis. The apparatus consists of a Be target placed in a 200 GeV π^- beam in front of a magnetic spectrometer. The differences with the present experiment (NA32) can be found in the trigger, the target and the vertex telescope (see also chapter 1). The events were reconstructed in the decay modes $D^+ \rightarrow K\pi\pi$, $D^o \rightarrow K\pi$ and $D^o \rightarrow K\pi\pi\pi$.

8. MARKII (GLAD1): the MARKII spectrometer at the PEP ring at SLAC is a magnetic spectrometer with, as a special later addition, a high resolution cylindrical drift chamber around the beam pipe to measure the decay tracks from heavy flavour mesons. The D mesons for the lifetime measurement are produced in e^+e^- collisions at a centre of mass energy of 29 GeV. To reduce the background which hides the inclusive D signals, one uses the decay $D^* \rightarrow D + \pi$ to select the events which form a peak in the D^*-D mass spectrum. The signal for D^o, as well as the signal for D^+, are observed with this method. The D^o is seen in the channels $K+\pi$ and $K+\pi+\pi^o$; the D^+ is seen in the channel $K+\pi+\pi$. For these events the distance of the D decay vertex with respect to the centre of the beam spot is measured. The lifetime is obtained from the displacement from zero of the distribution of these decay distances.

9. DELCO (YAMA1): The DELCO spectrometer is also situated at the PEP ring at SLAC. Again the D^{o} lifetime is measured using the D^{*} decay chain to reduce the background. To determine the lifetime, the distance of the decay tracks of the D^{o} are measured with respect to the beam centre (impact parameter method). The lifetime is extracted from the displacement from zero of the peak of this distribution.

7.2 Measurements of the D_s^+ Lifetime

The existence and mass of the D_s^+ meson have only recently been firmly established. The results from the e^+e^- ring experiments (refs. ALBR1, ALTH1, CHEN1, DERR1) now put its mass around 1.97 GeV. The measurement of the lifetime has only been done by three experiments of which a summary may be found in table 20.

Table 20: Measurements of lifetimes of D_s^+ mesons

The errors indicated are statistical and systematic respectively.

	experiment	production process	detection technique	coord. resol. µm	# events	lifetime 10^{-13}s
E531	(USHI1)	$\nu + N$	emulsion +spectr.	1	6	$2.6\pm^{1.6}_{0.9}$
NA11	(BAIL5)	$\pi^- + Be$	Siµstrip +spectr.	4.5	12	$3.1\pm^{1.2}_{0.8}$
HRS	(JUNG1)	e^+e^-	driftch. +spectr.	100	17	$3.5\pm^{2.4}_{1.8}\pm0.9$
NA32 this work		$K^- + Si$	Siµstrip +act.target +spectr.	4.5	8	$3.6\pm^{1.1}_{1.5}\pm0.4$

1. E531 (USHI1): This experiment has published a lifetime result based on the observation of 6 D_s^+ events, decaying in three prongs, in an emulsion.

2. NA11 (BAIL5): The predecessor of NA32 has published a result based on 12 events in the decay mode $D_s^+ \rightarrow KK\pi$ with an average lifetime of $(3.1\pm^{1.2}_{0.8})\bullet10^{-13}$s.

3. HRS (JUNG1): The High Resolution Spectrometer collaboration has measured the lifetime of a sample of 17 D_s^+ events decaying in the channel $D_s^+ \rightarrow \phi\pi$. The lifetimes were extracted from the measured de length distribution. The average lifetime is $(3.5\pm^{2.4}_{1.8}\pm0.9)\bullet10^{-13}$s.

7.3 Conclusions

Despite the large variations in detection techniques, each with its own statis and systematic errors, the lifetime results from most experiments are in good agree with each other. Improvements on these results may be obtained by experiments w observe large (>100) numbers of fully reconstructed events in just a few decay chan Moreover, for the lifetime of the D_s^+ meson one will need a good particle identifica to reject events due to misidentified D^+ decays.

8. COMPARISON WITH SOME MODELS

8.1 Theoretical Models

8.1.1 Introduction

In this chapter we will explore to what extent the results of the lifetime measurements can be used to test two recent theoretical models. We will extract the main parameters of these models, using our lifetime data . These show still large errors due to the low statistics. Nevertheless some conclusions can already be drawn.

The decay of the three pseudoscalar charmed mesons (D^o, D^+ and D_s^+) can be described with various processes. The diagrams corresponding to these processes are shown in fig. 8.1. The first type of diagram is the so-called spectator diagram (fig. 8.1b, c and d) in which the c quark decays via emission of a virtual W^+. The other antiquark in the meson remains unaffected by the decay, hence the name spectator quark. The second type is the so-called W exchange diagram (fig. 8.1e) in which both charmed quark and light antiquark are involved and a W^+, originating from the decay of the c quark, is absorbed by the light antiquark. The third type is the W annihilation diagram in which the charmed quark and the light antiquark annihilate into a W^+ (see fig. 8.1f and g). The diagram in fig. 8f, representing the decay through W annihilation of the D^+ meson, is Cabibbo suppressed.

Naively one would expect that only the spectator diagrams have an appreciable strength. The weak annihilation to a final state of a fermion and an antifermion is proportional to the masses of these fermions, and hence is small due to low values of the masses of the light quarks. This is analogous to the suppression of π or $K \rightarrow e\nu_e$ versus π or $K \rightarrow \mu\bar{\nu}_\mu$, which is known as a helicity suppression. The lifetimes in this naive quark model would then be the same for all charmed mesons, and be related to the lifetime of the muon which is described as well by a spectator diagram (fig. 8.1a) :

$$\tau_c = (\tfrac{1}{5})\,(m_\mu^5/m_c^5)\,\tau_\mu \qquad (8.1),$$

with: m_μ the mass of the muon

m_c the mass of the charmed quark (1.5–1.8 GeV).

Due to the uncertainty in the value of the charm quark mass, we obtain $\tau_c \sim 3.1\text{–}7.6 \cdot 10^{-13}$s. Measured D lifetimes have indeed this order of magnitude. The spectator diagrams predict equal lifetimes for charmed particles, which is essentially determined by τ_c, the lifetime of the charmed quark, and hardly influenced by the light quarks, i.e. :

$$\tau(D^+) \simeq \tau(D^o) \simeq \tau(D_s^+) \simeq \tau_c \qquad (8.2).$$

Similarly, the semileptonic branching ratios, for each lepton, for all weakly decaying charmed states should be equal, again dominated by the semileptonic decay of the c-quark ($BR_{sl}(c)$) :

$$BR_{sl}(D^+) \simeq BR_{sl}(D^o) \simeq BR_{sl}(D_s^+) \simeq BR_{sl}(c) \qquad (8.3),$$

which in the parton model is about 20%, since one out of five charm decays leads to an electron (muon) in the final state, as illustrated in fig. 8.2.

Both theoretical predictions are contradicted by experiment. The lifetimes show the following ratios :

$$\tau(D^+)/\tau(D^o) = 2.5\pm0.6 \qquad \text{(this thesis)} \qquad (8.4a).$$

$$\tau(D^+)/\tau(D_s^+) = 2.6\pm1.1 \qquad \text{(this thesis)} \qquad (8.4b).$$

Measured values (BALT1) of semileptonic branching ratios are :

$$BR_{sl}(D^+) = (17.0\pm1.9\pm0.7)\% \qquad (8.5).$$

$$BR_{sl}(D^o) = (\ 7.5\pm1.1\pm0.4)\%$$

The discrepancy between the predictions and the measurements of the lifetimes and branching ratios can be attributed to either or both of the following two mechanisms.

- The influence of the strong interaction (called colour clustering) can create a destructive interference, thus suppressing the non-leptonic decays of the D^+ mesons. It is a manifestation of the Pauli principle, as two $\bar{d}$'s are present in the final state of Cabibbo allowed D^+ decays (see fig. 8.1c). This will make the lifetime of the D^+ meson longer.
- A non-negligible W-exchange diagram in the D^o decay and W annihilation diagram in the D_s^+ decay, implying a mechanism in the strong interaction in the meson to counter the helicity suppression. This would decrease the lifetime of D^o and D_s^+ mesons.

The dominance of spectator diagrams has been used successfully by Bauer and Stech (BAUE1) for the description of exclusive two body decays of D-mesons (see section 8.1.2).

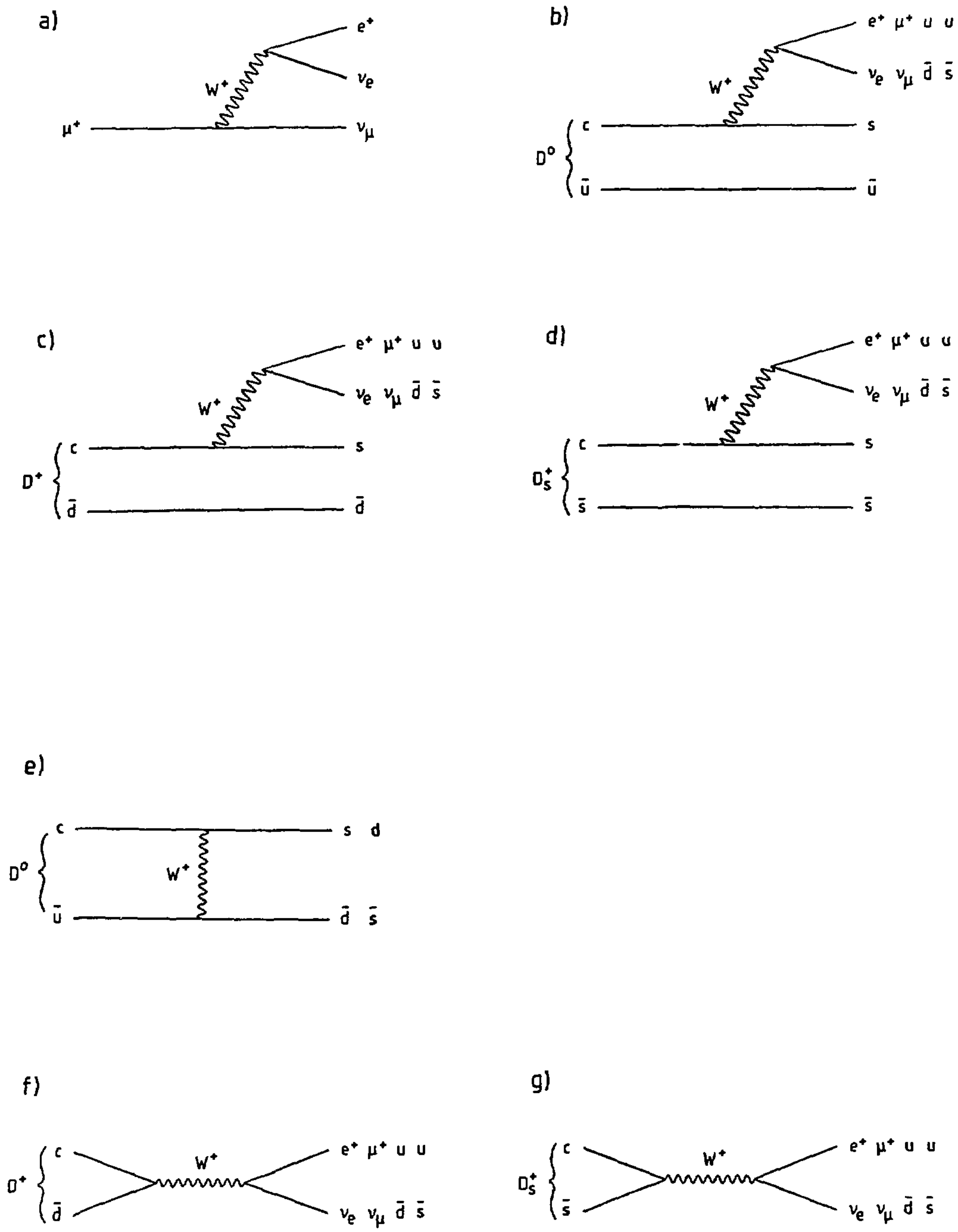

Fig. 8.1 The diagrams involved in charm decays, the individual diagrams are explained in the text.

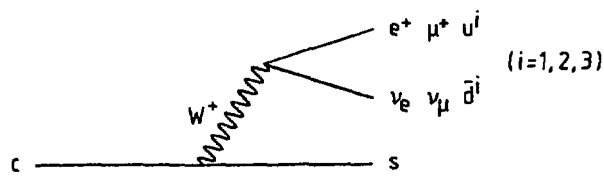

Fig. 8.2 The possible final states for the Cabibbo allowed decay of a charmed quark.

The two mechanisms responsible for the lifetime differences are discussed using a model by Rueckl (RUEC1), describing inclusive charm decays in section 8.1.3.
The measured branching ratios refered to in this chapter are summarized in table 22.

8.1.2 The decay widths of two body decays of D mesons

In order to separate the effect of the short distance strong interactions from that of the W-exchange and annihilation diagrams, Bauer and Stech (BAUE1) have proposed the following model.

It is very likely that two body decays of charmed mesons, in which the decay products have large momenta, are only due to spectator diagrams. They used the effective Hamiltonian (ELLI1) for two body decays, in which they replace the V-A quark currents by hadron currents. For the non-leptonic two body decays the Hamiltonian then becomes :

$$H_{eff} = (G/\sqrt{2})\cos^2\Theta \, :(a_1(\bar{u}d)_H(\bar{s}c)_H + a_2(\bar{s}d)_H(\bar{u}c)_H): \qquad (8.6),$$

with : G the weak coupling constant,
Θ the Cabibbo mixing angle
$(\bar{u}d)_H$, $(\bar{s}c)_H$, $(\bar{s}d)_H$ and $(\bar{u}c)_H$ the hadron currents.

The real coefficients a_1 and a_2 contain the colour exchange effects between the quark currents. They are related to the QCD short distance coefficients c_+ and c_- of the usual effective quark Hamiltonian by :

quark currents. They are related to the QCD short distance coefficients c_+ and c_- of the usual effective quark Hamiltonian by :

$$a_1 = c_1(\mu) + \xi c_2(\mu)$$
$$a_2 = c_2(\mu) + \xi c_1(\mu) \qquad (8.7),$$

with ξ the colour suppression factor, which is the contribution of diagram 8.3b relative to diagram 8.3a, and :

$$c_1(\mu) = \tfrac{1}{2}(c_+(\mu) + c_-(\mu))$$
$$c_2(\mu) = \tfrac{1}{2}(c_+(\mu) - c_-(\mu)) \qquad (8.8).$$

assuming that factorization is a good approximation at a specific energy scale μ. Furthermore, c_+ and c_- obey the relation $c_+^2 c_- = 1$ (ELLI1).

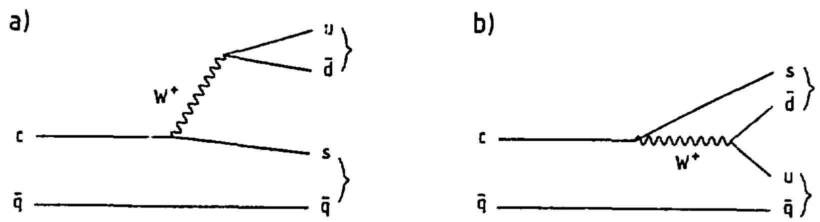

Fig. 8.3 Quark diagrams for two-body decays of D-mesons.

Using this Hamiltonian the partial decay widths can be calculated. The decay channels can be classified as those depending on a_1, a_2 and on a_1+xa_2, where x depends on the process (FAKI1). This can be deduced from the hadron currents in (8.6) and the quark content of initial and final states. In table 21 the results obtained for some decay widths are summarized (BAUE1). They found $|a_1| \simeq 0.89$, and $|a_2| \simeq 0.54$, and that their ratio a_2/a_1 should be negative, using the MARKIII data (BALT1). They discuss that these values are shifted by incorporating final state interactions. By fitting the decays $D^0 \to K^-\pi^+$ and $D^0 \to \bar{K}^0\pi^0$, taking $a_1 > 0$, $a_2 < 0$ and using the $K\pi$ phase shift analysis, they obtain $a_1 \simeq 1.06$ and $a_2 \simeq -0.62$.

Table 21: The model predictions of some partial decay widths by Bauer and Stech.

decay channel	$\Gamma_{part.}$ in $10^{10}\ s^{-1}$
$D^0 \to K^-\pi^+$	$17.1\ a_1^2$
$D_s^+ \to \phi\pi^+$	$9.4\ a_1^2$
$D^+ \to \phi\pi^+$	$2.0\ a_2^2$

For comparison with the short distance QCD coefficients, they argue that in the transition from quark currents to hadron currents, an additional factor of 0.9 should be used to account for the incomplete overlap of initial and final internal meson wave functions. In that case, they obtain $a_1 \approx 1.2$ and $a_2 \approx -0.72$ from the MARKIII data. Using our measurements on the lifetimes and the branching ratios of the MARKIII collaboration, we can anew calculate the coefficients a_1 and a_2 using the values for the partial widths of table 21 from :

$$a_1^{\,2} = (BR[D^0 \to K^-\pi^+]/17.1 \bullet 10^{10} \tau(D^0)) = 0.86 \pm 0.25 \qquad (8.9a)$$

$$a_2^{\,2} = (BR[D^+ \to \phi\pi^+]/2.0 \bullet 10^{10} \tau(D^+)) = 0.49 \pm 0.26 \qquad (8.9b),$$

yielding $a_1 = 0.93 \pm 0.14$, and $a_2 = -0.70 \pm 0.19$, using the sign convention of Bauer and Stech. Using expression 8.8 and the values of $c_+ = 0.74$ and $c_- = 1.8$ at $\mu = 1.5$ GeV obtained by Rueckl (RUEC1), one finds $c_1 = 1.27$ and $c_2 = -0.53$. The relations (8.7) between a_1, a_2, c_1 and c_2 provide two measurements of the colour suppression factor ξ. The average value is $\xi = 0.25 \pm 0.28$, which is compatible with the standard value $\xi = 1/3$, but does not exclude a smaller value or even $\xi = 0$. It should be remarked that the error in ξ does not contain contributions due to the theoretical uncertainties in c_1 and c_2 (or c_+ and c_-) and the uncertainties in the estimates of the coefficients of a_1^2 and a_2^2 of table 21. Moreover, a_1 and a_2 are obtained from two decay channels only, and not from a fit to many channels as in BAUE1.

We can now compare branching ratios of two body decays. Using our measurement of $\tau(D_s^+)$, we obtain :

$$BR(D_s^+ \to \phi\pi) = \Gamma(D_s^+ \to \phi\pi)\tau(D_s^+) = (2.9 \pm 1.3)\% \qquad (8.10),$$

in good agreement with the value measured by the CLEO group (CHEN1) and the HRS group (DERR1) of (3.3±1.1)% and 4.4%, respectively.

Alternatively, using the average of the measured values of $BR(D_s^+ \to \phi\pi)$, we can derive the ratio of the lifetimes of D_s^+ and D^0, i.e. :

$$\tau(D_s^+)/\tau(D^0) = (\Gamma[D^0 \to K^-\pi^+]/\Gamma[D_s^+ \to \phi\pi^+] \bullet (BR[D_s^+ \to \phi\pi^+]/BR[D^0 \to K^-\pi^+]) = 1.2 \pm 0.4 \qquad (8.11).$$

This ratio agrees well with our measured value of 0.9±0.4.

We may conclude that the analysis by Bauer and Stech gives rise to a consistent description of the two body decay channels of D mesons via spectator diagrams.

8.1.3 The contribution of interference effects and of W exchange diagrams

In this section we will discuss a model by Rueckl (RUEC1) to consider both two body and many body charm decays, and stresses the importance of the non-spectator processes for these decays.

Rueckl remarks that the short distance coefficients $c_+ = 0.74$ and $c_- = 1.8$ at $\mu = 1.5$ GeV modify the semileptonic branching ratio of the c-quark from 20% to (RUEC1):

$$BR_{sl}(c) = 1/(2+2c_+^2+c_-^2) \approx 16\% \qquad (8.12),$$

which is close to the measured value for the D^+ meson of 17.0% (BALT1). However, the value for BR_{sl} for D^o is not explained. Using the lifetimes and semileptonic branching ratio of the PDG (PDG1), we observe that the partial width for semileptonic decay of D^+ and D^o are nearly equal within errors at a value around $\Gamma_{sl} = 20 \cdot 10^{10} s^{-1}$. The deviations from the total width (or lifetime) for D^o and D_s^+ must be due to additional non-leptonic partial widths.

For the two mechanisms, which may resolve these discrepancies, mentioned in section 8.1.1, Rueckl (RUEC1) has remarked that interference effects may increase the lifetime of the D^+ meson slightly, but cannot explain e.g. the ratio $\tau(D^+)/\tau(D^o)$. However, the existence of a substantial contribution of W-exchange diagrams to the decay of the D^o meson is illustrated by the observation of a sizable branching ratio $BR(D^o \to \overline{K}^o \phi)$. This decay channel can only be described by a W-exchange diagram. E.g. the ARGUS collaboration has measured this branching ratio to be (0.99±0.32±0.17)%. The helicity suppression of the W exchange and W annihilation diagrams may be lifted by soft gluon effects. The contribution of W exchange and W annihilation are described by the parameters $P^{(1)}$ and $P^{(8)}$, which are assumed to be equal for all D-mesons. The quantities $P^{(1)}$ and $P^{(8)}$ represent the product of the probability for the annihilating constituent quarks to be in a spin 1 colour singlet and a spin 1 colour octet configuration, respectively, times the spatial overlap of the wave functions of the quarks. Rueckl (RUEC1) derives the ratio $P^{(8)}/P^{(1)}$ from the relation

$$P^{(8)}/P^{(1)} = r_8/r_1 \qquad (8.13),$$

and r_8 and r_1 can be computed from the following lifetime ratios :

$$\tau(D^+)/\tau(D^o) = [2+2c_+^2+c_-^2+(2c_+-c_-)^2(r_1/3)+(c_++c_-)^2(r_8/12)] \;/\; (2+2c_+^2+c_-^2) \quad (8.14a),$$

$$\tau(D^+)/\tau(D_s^+) = [2+2c_+^2+c_-^2+(2c_++c_-)^2(r_1/3)+(c_+-c_-)^2(r_8/12)+2r_1] \;/\; (2+2c_+^2+c_-^2) \quad (8.14b).$$

Here, r_1, is the ratio of the semi-leptonic widths due to annihilation and quark decay. The ratio r_8/r_1 quantifies the proportion in which spin-1 colour octet and colour singlet configurations of the constituent quark are involved. For $r_8 = 8r_1$, the chances would be equal.

Using the measured values of the lifetime ratios and the above values for c_+ and c_-, we obtain :

$$r_1 = 1.5\pm1.3$$

$$r_8 = 18\pm3$$

$$P^{(8)}/P^{(1)} = r_8/r_1 = 12\pm11 \quad (8.15).$$

The value $r_1 = 1.5\pm1.3$ is consistent with the value calculated by Rueckl, $r_1 \approx 2.3$. Our result for the ratio $r_8/r_1 = P^{(8)}/P^{(1)}$ is compatible with the value $r_8/r_1 \simeq 5.4$ of Rueckl, but also does not rule out $r_8/r_1 = 8$, i.e. equal contributions from the two configurations of the quarks in the D meson: spin 1 colour singlet and spin 1 colour octet. The present data on lifetimes thus indicate crude agreement with the description of Rueckl. The prediction obtained by a pertubative QCD calculation, that $P^{(8)} \gg P^{(1)} \sim 0$, as well as similar results obtained with a soft gluon multipole expansion, are ruled out by this result (see ref. RUEC1 section VI-1).

If the diagram depicted in fig. 8g, representing the decay through W annihilation of the D_s^+, has a reasonable strength, this implies that decays of the D_s^+ into a final states with pions only should occur. Observation of such decay modes are experimentally very difficult, and have up to now not been reported.

Table 22: Summary of experimental data used in this chapter.

	D^o	D^+	D_s^+
BR_{sl} (BALT1)	(7.5±1.1±0.4)%	(17.0±1.9±0.7)%	
$BR(D^o \to K^-\pi^+)$ (BALT1)	(5.6±0.4±0.3)%		
$BR(D^+ \to \phi^-\pi^+)$ (BALT1)		(0.93±0.26±0.17)%	
$BR(D_s^+ \to \phi^-\pi^+)$ (CHEN1)			(3.3±1.1)%
(DERR1)			(4.4)%
$BR(D^o \to \bar{K}^o\phi)$ (BALT1)	(0.99±0.32±0.17)%		

8.2 Conclusions

We have applied the model of Bauer and Stech, which describes two body decays of D mesons with a spectator mechanism, to our lifetime data. Using this model and the measured lifetimes, it is possible to derive $BR(D_s^+ \rightarrow \phi\pi)$ well in agreement with measured values for this branching ratio. Alternatively, the lifetime ratio $\tau(D_s^+)/\tau(D^o)$ predicted by the model and using the measured value of $BR(D_s^+ \rightarrow \phi\pi)$ agrees with our value. The colour suppression factor found is in agreement with the expected value $\xi = \frac{1}{3}$, but does not rule out $\xi = 0$ as suggested by Bauer and Stech.

We have made a crude determination of the ratios r_1, r_8, and $P^{(8)}/P^{(1)} = r_8/r_1$ used by Rueckl. The results are in agreement with the values for these ratios estimated by Rueckl, and thus indicate that spectator and exchange/annihilation processes are of roughly equal importance in inclusive charm decays.

SUMMARY

In this thesis an experiment is described to measure the lifetimes of pseudoscalar charmed mesons. The experiment is located in the CERN North area and uses a negatively charged unseparated hadron beam of 200 GeV. The experiment is carried out with a magnetic spectrometer preceded by a beam telescope, consisting of 4 Si microstrip detectors, an active target, consisting of 14 Si microstrip detectors, and a vertex telescope, consisting of 7 Si microstrip detectors in 3 different strip orientations for an accurate reconstruction of beam direction, primary and secondary vertices. The spectrometer consists of two spectrometer magnets, 48 planes of drift chambers and 3 Cerenkov hodoscopes for the determination and identification of charged secondaries. The lifetimes of the charmed mesons are determined by measuring the length of their flight path, their momentum and their mass. The results, which are described in the thesis, are based on the analysis of part of the collected data.

In chapter 2, a description is given of the spectrometer used for the measurements. In chapter 3, the most important features of Si microstrip detectors are discussed. A model is presented for the charge drift and diffusion in Si detectors; calculated and measured coordinate resolutions are compared. Chapter 4 contains a description of the trigger, the calibration procedures and the data sample collected. In particular, the calibration of the Si detectors is described. Chapter 5 treats the track reconstruction and event selection for this analysis. The event preselection is presented, and its acceptance and efficiency for short lived decays is assessed. The reconstruction of tracks in the microstrip detectors and the vertex selection with these tracks are described in detail.

In chapter 6, the mass spectra and lifetime results are presented. The lifetimes are $\tau(D^0) = (3.8 \pm^{0.7}_{0.5} \pm 0.4)\bullet 10^{-13}$s, $\tau(D^+) = (9.5 \pm^{2.1}_{1.6} \pm 0.4)\bullet 10^{-13}$s and $\tau(D_s^+) = (3.6 \pm^{1.1}_{1.5} \pm 0.4)\bullet 10^{-13}$s. The first error is the statistical error and the second error is the systematic errors (due to the selection criteria). The production rates in the K^- beam and in the π^- beam are found to be in the same order of magnitude within the x_F range covered. Previous experimental data on the lifetimes of charmed particles are reviewed in chapter 7.

In the last chapter, a theoretical interpretation is presented of the measured decay properties. The decay of each charmed meson can be described by two out of three possible Cabibbo-allowed decay processes. The results presented on the lifetimes of D^o, D^+ and D_s^+ show that the model of Bauer and Stech for the description of exclusive two body decays with spectator diagrams, modified by strong interaction effects, gives a consistent description of non-leptonic partial decay widths of these channels. The lifetime ratios $\tau(D^+)/\tau(D^o)$ and $\tau(D^+)/\tau(D_s^+)$ are in agreement with estimates of Rueckl on the relative contribution of the semi-leptonic decay widths to quark decay and W exchange/W-annihilation, indicating that W exchange/W annihilation is an equally important decay mechanism.

SAMENVATTING

In dit proefschrift wordt een experiment beschreven, waarin de levensduren van de pseudoskalaire mesonen worden gemeten, die het vierde quark, charm, beva en. De experimentele opstelling bevindt zich in de Noordhal van CERN. Met behulp van het CERN Super Proton Synchrotron (SPS) wordt een bundel negatief geladen hadronen met een impuls van 200 GeV naar het experiment gezonden. De experimentele opstelling is samengesteld uit een magnetische spektrometer, voorafgegaan, in volgorde door: de bundeldetektoren, de aktieve trefplaten en een vertex teleskoop. De bundel wordt waargenomen met vier Si mikrostrip detektoren met drie verschillende orientaties van de detektiestroken. De aktieve trefplaten, waarmee de bundeldeeltjes kunnen botsen, worden gevormd door 14 dicht opeen geplaatste Si mikrostrip detektoren. De ionisatie veroorzaakt door de reaktieprodukten kan met deze detektoren worden waargenomen. De in de botsing of door verval gevormde deeltjes worden gedetekteerd met de vertex teleskoop, met 7 Si mikrostrip detektoren, eveneens met drie verschillende orientaties van de detektiestroken. De impuls en identiteit van de gevormde deeltjes worden gemeten met dc spektrometer, welke de volgende elementen bevat: twee spektrometer magneten, 48 driftkamer vlakken en 3 veelcellige Cerenkov tellers. De levensduur van een charm meson wordt bepaald door de afstand tussen de produktievertex en de vervalsvertex, alsmede door de massa en de impuls. De in dit proefschrift gepresenteerde resultaten zijn gebaseerd op de analyse van een deel van het totale gegevensbestand.

In hoofdstuk 2 wordt een beschrijving gegeven van de experimentele opstelling.

Hoofdstuk 3 bevat enkele belangrijke eigenschappen van Si mikrostrip detektoren. De drift en diffusie van de in de Si detektoren door de deeltjes vrijgemaakte ladingen worden in een model beschreven. Het op deze wijze berekende oplossend vermogen wordt vergeleken met de gemeten waarden. Hoofdstuk 4 bevat een beschrijving van de direkte instrumentele selektie van gebeurtenissen, van de kalibratie van de detektoren en van het verzamelde gegevensbestand. In hoofdstuk 5 worden de rekonstruktie en de selektie van gebeurtenissen door het analyseprogramma behandeld. Aan het begin van de rekonstruktie worden de gebeurtenissen voorgeselekteerd. Een beschrijving van deze voorselektie wordt gegeven en de doeltreffendheid ervan voor gebeurtenissen met een kortlevend verval wordt geschat. De rekonstruktie van de sporen in de vertex teleskoop en de selektie van de gerekonstrueerde vertices worden in detail behandeld. De berekende levensduren van de charm mesonen worden in hoofdstuk 6 gepresenteerd. De levensduren zijn $\tau(D^o)=(3.8\pm^{0.7}_{0.5}\pm0.4)\bullet10^{-13}s$ $\tau(D^+)=(9.5\pm^{2.1}_{1.6}\pm0.4)\bullet10^{-13}s$ en $\tau(D_s^+)=(3.6\pm^{1.1}_{1.5}\pm0.4)\bullet10^{-13}s$. De aangegeven fouten zijn respektievelijk de statistische en de systematisch fout (ten gevolge van de selektie procedure). Uit de geobserveerde signalen wordt gekonkludeerd dat de charm mesonen in πSi en KSi wisselwerkingen, binnen de fout, en in het door de spektrometer bestreken x_F interval, in gelijke mate geproduceerd worden. Hoofdstuk 7 bevat een korte samenvatting van deze levensduren gemeten in andere experimenten. Het laatste hoofdstuk bespreekt twee theoretische beschrijvingen van de vervalseigenschappen van charm mesonen. Het verval van elk van de drie mesonen kan beschreven worden door twee van drie mogelijke vervals processen. De modelbeschrijving van Bauer en Stech voor de vevalskanalen van charm mesonen naar twee deeltjes vormt, als de levensduurresultaten gebruikt worden, een konsistent beeld van de vervalsbreedten van deze niet leptonische vervalskanalen. De schattingen van Rueckl ten aanzien van de bijdrage van de semi-leptonische vervalsbreedten tot het quark verval en de W annihilatie/W uitwisseling zijn in overeenstemming met de geobserveerde verhoudingen van de levensduren $\tau(D^+)/\tau(D^o)$ en $\tau(D^+)/\tau(D_s^+)$. Dit laatste toont aan dat W annihilatie en W uitwisseling processen zijn die in sterkte vergelijkbaar zijn met het toeschouwer proces.

ACKNOWLEDGEMENTS

At this place I have the pleasure to thank everybody who had a constructive contribution to this thesis.

I thank the members of the ACCMOR collaboration for the pleasant cooperation. It has been a very positive experience and a great pleasure to work at CERN in an international group. I acknowledge each individual contribution by the group members without going to the sheer impossible task of listing them.

I make an exception for Kees Daum to thank him for his constant support and enthusiasm. Most of the results in this thesis were product of our cooperation, a cooperation I experienced as very pleasant and instructive.

I thank Prof. Kluyver , my promotor, for carefully reading the manuscript.

Carol Ponting can type a thesis in 4 days, something I thought impossible until I actually saw it happen.

Finally I would like to thank Lucie for her support throughout all these years.

REFERENCES

ABE1 K. Abe et al., Phys. Rev. D 33 (1984) 1.

ADAM1 M. Adamovich et al., CERN-EP/86-77 June 1986, submitted to Phys. Lett. B.

AGUI1 M. Aguilar-Benitez et al., Phys. Lett. 122B (1983) 312.

AGUI2 M. Aguilar-Benitez et al., CERN-EP/85-130, submitted to Z. Phys. C.

ALBI1 E. Albini et al., Phys. Lett. 110B (1982) 339.

ALBR1 H. Albrecht et al., Phys. Lett. 153B (1985) 343.

ALBR2 H. Albrecht et al., Phys. Lett. 158B (1985) 525.

ALTH1 M. Althoff et al., Phys. Lett. 136B (1984) 130.

BADE1 A. Badertscher et al., Phys. Lett. 123B (1983) 471.

BAIL1 R. Bailey et al., Nucl. Instrum. and Meth. 226 (1984) 56-58.

BAIL2 R. Bailey et al., proposal NA32, CERN/SPSC/82-57, SPSC/P180.

BAIL3 R. Bailey et al., Z. Phys. C 28 (1985) 357-363.

BAIL4 R. Bailey et al., Z. Phys. C 30 (1986) 51-63.

BAIL5 R. Bailey et al., Phys. Lett. 139B (1984) 320, Contr. to Int. Europhysics Conf. on High Energy Physics, Bari 1985.

BAIL6 R. Bailey et al., Phys. Lett. 132B (1983) 230.

BALT1 R. Baltrusaitis et al., Phys. Rev. Lett. 54 (1985) 1976;
R. Baltrusaitis et al., Phys. Rev. Lett. 55 (1985) 150;
R. Baltrusaitis et al., Phys. Rev. Lett. 56 (1986) 2141.

BAUE1 M. Bauer & B. Stech, Phys. Lett. 152B (1985) 380;
Proc. Moriond Workshop on Flavour Mixing and C.P. Violation, La Plagne 1985, p. 151.

BEBE1 C. Bebek et al., Cleo-86-2 CLNS-86/715.

BELA1 E. Belau, Ph.D. thesis Ludwig-Maximilians Universität, München 1985;
MPI-PAE/Exp. El. 151, June 1985.

BELA2 E. Belau et al., Nucl. Instr. and Meth. 214 (1983) 253-260.

BELA3 E. Belau et al., Contr. to Int. Conf. on Hadron Spectr., Maryland, April 1985.

BIGI1 I. Bigi, PITHA 85/14, August 1985.

BLAN1 G. Blanar et al., proposal NA11, CERN/SPSC/78-14, SPSC/P95.

BLUN1 O. Blunck & S. Leisegang, Z. Phys. C 128 (1950) 500.

CASO1 C. Caso & M. Touboul, submitted to La Rivista del Nuovo Cimento, CERN-EP/85-176.

CHAR1 G. Charpak & F. Sauli, CRRN-EP/84-35.

CHEN1 A. Chen et al., Phys. Rev. Lett. 51 (1983) 634.

DAUM1 C. Daum et al., Nucl. Instr. and Meth. 176 (1980) 119-127.

DERR1 M. Derrick et al, Phys. Rev. Lett. 54 (1985) 2568.

DIJK1 H. Dijkstra, Ph.D. thesis, Universiteit van Amsterdam, 1985.

EADY1 W. Eady, D. Drijard, F. James, M. Roos and B. Sadoulet, Statistical methods in experimental physics, North Holland, 1971, section 9.3.

ELLI1 J. Ellis et al., Nucl. Phys. B100 (1975) 313

ENGL1 J. England et al., Nucl. Instr. and Meth. 185 (1981) 43-47.

FAKI1 D. Fakirov and B. Stech, Nucl. Phys. B133 (1978) 315-326.

FANO1 U. Fano, Ann. Rev. Nucl. Sci. 13 (1963) 1.

FLAM1 V. Flamino et al., CERN-HERA 79-01.

GLAD1 L. Gladney, Ph.D. thesis, Stanford 1985.

HALL1 G. Hall, IC/HENP/83-1.

HANC1 S. Hancock et al., CERN DD/83/14, EP/83-76.

HANC2 S. Hancock et al., CERN DD/83/20, EP/83-138.

HAUS1 J. Hauser, Ph.D. thesis, Cal. Inst. of Techn., 1985 (unpublished).

HEIJ1 E. Heijne, Ph.D. thesis, Universiteit van Amsterdam, 1983; CERN-EF/83-06.

HYAM1 B. Hyams et al., Nucl. Instr. and Meth. 205 (1983) 99-105.

JUNG1 C. Jung et al., Phys. Rev. Lett. 56 (1986) 1775.

KOLB1 K. Kolbig & B. Schorr, Asymptotic expansion for the Landau density and distribution functions, CERN.

LAND1 L. Landau, J. of Phys. (USSR) 8 (1944) 201.

NEUG1 E. Neugebauer, Ph.D. thesis Ludwig-Maximilians Universität, München 1984; MPI-PAE/Exp. El. 152, November 1984.

PDG1 Particle Data group, Rev. Mod. Phys., vol. 56, no. 2, part 2, April 1984.

PETE1 S. Peters, Ph.D. thesis, Universiteit van Amsterdam, 1980.

RANC1 P. Rancoita & A. Seidman, La Revista del Nuovo Cimento, No. 7 (1982).

REAY1 N. Reay, Proc. Int. Lepton/Photon Symp., Cornell Univ. 1983, p. 244.

REAY2 N. Reay, Int. Conf. on Phys. in Collision, Como 1983.

ROSS1 B. Rossi, High energy particles, 1952.

RUEC1 R. Rueckl, Habilitationsschrift, Univ. Munich 1983.

SHUL1 P. Shulek et al., Soviet J. Nucl. Phys. 4 (1967) 400.

SPIE1 W. Spierenburg, Ph.D. thesis, Universiteit van Amsterdam, 1983.

SZE1 Sze, Physics of Semiconductor Devices, 1981.

USHI1 N. Ushida et al., Phys. Rev. Lett. 56 (1986) 1767; Phys. Rev. Lett. 56 (1986) 1771.

VAVI1 P. Vavilov, Soviet Phys. JETP 5 (1957) 749.

YAMA1 H. Yamamoto et al., SLAC-PUB-3628 (1985), submitted to Phys. Rev. D.